Modeling, processing, and characterization of dielectric elastomer actuators and sensors

Kevin Kadooka

A dissertation

submitted in partial fulfillment of the

requirements for the degree of

Doctor of Philosophy

University of Washington

2017

Reading Committee:

Minoru Taya, Chair

Jaehyun Chung

Sawyer Fuller

Program Authorized to Offer Degree:

Mechanical Engineering

University of Washington

Abstract

Modeling, processing, and characterization of dielectric elastomer actuators and sensors

Kevin Kadooka

Chair of the Supervisory Committee:
Professor Minoru Taya
Mechanical Engineering

Over the past two decades, electroactive polymers (EAP) have been studied as a material for soft actuator and sensor systems. Dielectric elastomers (DE) are an EAP material which relies on the electrostatic force produced on compliant electrodes to produce deformation. In the converse sense, DE sensors can be used by measuring the electrical energy or impedance change produced under deformation. The two key limitations barring DE from commercial use are high driving voltage, and low output force. The scope of this work is as follows: to improve upon these two limitations by processing of actuators by a pneumatic dispenser, by adding tactile sensing and variable stiffness properties to the actuators, and developing a mechanical model to predict the actuator behavior. This work focuses specifically on the unimorph dielectric elastomer actuator (DEA), which consists of a DE laminate which contracts in the thickness direction and expands in-plane under applied voltage, and is constrained on one face by a passive material, resulting in bending of the structure.

The first part of the work is devoted to fabrication, modeling, and characterization of multilayer unimorph DEA. Fabrication is done using two schemes – the first is a conventional one, using

commercially available DE films, and the second is a novel method using a robotic dispenser system. The latter technique has two objectives. The first is to reduce the thickness of the DE layers to reduce driving voltage, since the DE deformation is proportional to the square of the applied electric field which itself is inversely proportional to electrode separation. The second is to deposit higher-performance DE materials, in this case, PVDF terpolymer, which exhibits large actuation stresses because of its high dielectric constant and relatively high Young's modulus. Using the dispenser, DE layers with 10 μm thick layers are repeatably produced, requiring actuation voltages one order of magnitude less than conventional thick DE films. Standard deviation of displacement and blocking force do not exceed 10% and 15% of the mean after 2 minutes of deformation, respectively. Elastic and viscoelastic models are developed for multilayer unimorph DEA consisting of flat and curved geometries. Both models were validated in comparison with experimental data with the latter shown to agree with the experimental data to within one standard deviation of the mean for majority of the deformation.

The second section demonstrates the novel use of electrolaminates to create variable stiffness DEA (VSDEA). Variable stiffness structures are of particular interest for soft actuators, because they allow switching between a low stiffness, high displacement mode and a high stiffness mode with large holding force. One device is demonstrated by simply utilizing the passive layer of a DEA as part of an electrolaminate, allowing for four-fold increase in bending rigidity. Another device is demonstrated consisting of a bundle of parallel DEA with electrostatic chucking features to modulate shear strength of the interfaces. This device exhibits a 39-fold increase in stiffness, and a claw actuator using these actuators is capable of lifting an object 17 times its own weight.

The final part of this work investigates two novel tactile sensors based on dielectric elastomers (DES). The first uses a dome-shaped protrusion to redistribute tactile forces onto an array of four capacitive sensors. The change in capacitance of the four sensors is used to measure and discriminate the force components of the impinging force. An array of these dome DES are fabricated using the dispenser system, and the ability to differentiate between normal and shear forces was demonstrated, as well as its proximity sensing ability. The tactile sensor array is also shown integrated as the passive layer of a DEA, providing tactile and proximity sensing capability to the actuator. The second tactile sensor features high resolution and scalability, and

is built in to a medical assistive device coined the “artery mapper” and is used to determine the location of a target artery for arterial line placement. It is demonstrated locating an artery on a test subject, possible due to its force resolution on the order of 2.8 kPa.

Table of Contents

List of Figures

List of Tables

1. Introduction

1.1 Motivation

One outstanding aspect of nature, compared to conventional man-made robotics, is its flexibility – not just in its ability to evolve and adapt, but also the inherent compliance of its actuation and sensing apparatus. The cucumber tendril, for instance, is an example of a natural sensor-actuator system which undergoes a complex shape change using a simple mechanism. Gerbode [1] hypothesized that the transformation from the straight plant tendril, to the helically coiled shape used for structural support, is caused by asymmetric stiffening of an internal fiber, combined with contraction of the tendril. In addition, the surface of the cucumber tendril is covered in an array of soft hemispherical sensors to provide tactile feedback, a model which has inspired sensor arrays in soft-robotics based man-made robots [2] [3]. The example of the cucumber tendril is fascinating, but nature as a source of inspiration for soft robotics is broad and diverse, highlighted in a recent review of bioinspired actuators and sensors by Taya et.al [4]. This is reflected by the influx of research on electroactive polymers (EAP) over the past two decades. Such soft transducer materials are capable of complex motion, are lightweight, independent of scale, silent, feature no moving parts, and are compliant. Conventional electromagnetic actuators on the other hand, tend to be stiff and bulky, an obvious detriment to biomimetic design of robots on ever more complex and compact scales, highlighting the need to investigate soft artificial muscle and sensors.

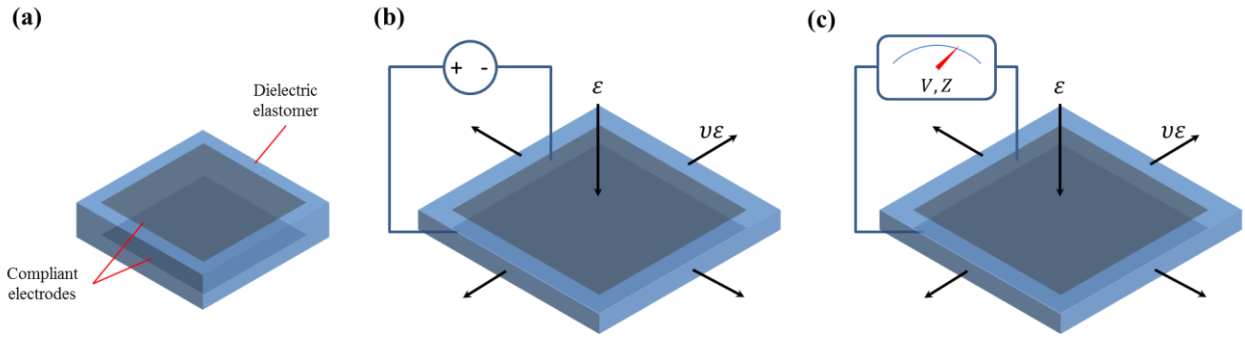

Figure 1. Operating principle of DE actuators and sensors showing (a) basic layout of DE transducer, (b) actuator mode, and (c) sensor mode.

Dielectric elastomers (DE) are a subgroup of electroactive polymers typified by their low stiffness and constant dielectric permittivity over a range of strains, and have been shown to

exhibit large actuation strains and stresses. In its simplest form, a DE transducer consists of a DE membrane sandwiched between two compliant electrodes, essentially forming a compliant capacitor (Figure 1). DE actuators (DEA) operate on the principle of electrostatic attraction of opposite charges on the electrodes, which deforms the membrane. DE sensors (DES) have a variety of sensor mechanisms, involving energy generation and impedance change under applied loading. Recent research seeks to apply DE transducers as end-effectors for robotic hands and surgical robots, as microfluidic pumps, adaptive optics, energy harvesters, fluidic flow sensors, and flexible robotic skin, to name a few applications. Despite their apparent benefits compared to conventional transducers, EAP, including DE, have yet to displace them in any commercial application. Among their key limitations are low blocking force and relatively high driving voltage. Innovative new types of structures and fabrication methods are needed to enhance their performance, and tools to guide their design and predict their behavior are equally important.

1.2 Overview

The objective of this work is to improve upon the limitations of DEA and DES barring them from widespread commercial applications, focusing on two main topics: (i) development of novel processing methods and structures, and in the case of DEA, (ii) development of an analytical closed-form model to predict their behavior.

Chapter 2 provides an overview of the existing literature on recent DEA and DES research, with specific focus on three areas of development: material, processing, and geometry. The references have been chosen to focus on reduction of actuation voltage, and increase of blocking force of DEA. Based on the literature, a ferroelectric relaxor polymer, P(VDF-TrFE-CFE) is chosen as a dielectric material to produce high stresses and moderate strains. Pneumatic dispensing is chosen as an effective processing tool to produce complex and varying DEA structures with thin layers to lower actuation voltage. The unimorph structure is chosen as the geometry needed to produce large out-of-plane displacements without additional complications such as material pre-stretch. Limitations of current EAP sensor devices are highlighted.

Chapter 3 focuses on fabrication and modeling of DEA. Two processing methods of DEA are presented. The first is more conventional, based on fabrication of DEA from commercially available films. Actuators based on this construction were used in verification of a mechanical model of DEA actuation presented in Chapter 4. The second method relies on a robotic dispenser

to produce multilayered unimorph DEA from PVDF terpolymer, highlighting the deposition parameters and procedure to produce homogeneous films of DE and electrode materials. Elastic and viscoelastic models are developed to predict the behavior of multilayer unimorph DEA, the former based on classical beam theory, and the modeling done by Smits and Choi [5] and other researchers on piezoelectric benders, and the latter applies the viscoelastic correspondence principle to the elastic solution to predict the time-dependent behavior of the DEA. Both models are verified against experimental data.

Chapter 4 introduces the concept of electrostatic chucking as a mechanism for variable stiffness DEA, allowing for rapid and low-power transition from flexible to rigid states. Two variable stiffness DEA are demonstrated, the first where the passive layer of a unimorph DEA is retrofitted with an electrolaminate, and the second consists of a bundle of parallel DEA units where their interfacial shear strength is modulated by electrostatic chucking. Equations are presented to predict their stiffness change and also load-carrying capacity of a claw actuator.

Chapter 5 details the fabrication and characterization of two novel types of DES. The first is a tactile sensor which can extract the components of an impinging force. It is envisioned as a flexible sensor for robotic end effectors, where manipulation of objects requires feedback of the magnitude and direction of normal and shear forces acting on a surface. The second is a tactile sensor array used as the sensing element in an assistive medical device used to map the position of a target artery for tasks such as arterial line placement in hospital settings.

Finally, Chapter 6 summarizes the key achievements of the work, and makes recommendations for future research.

2. Literature review

2.1 Dielectric elastomer actuators

Although electrostatic forces have been known through the works of physicists such as Coulomb and Maxwell for centuries, the use of electrostatic attraction to achieve actuation of dielectric elastomers was not well known until the 1990's through the pioneering works of SRI researchers Pelrine et al. [6] and Kornbluh et al. [7]. These works described actuation of polymer dielectrics using only the Maxwell stress p, developed by the electrostatic attraction between two compliant electrodes, where ε_o is vacuum permittivity, ε_r is the elastomer's dielectric constant, and E^2 denotes the electric field (Equation (1)). This was significant, because previous work on electrostrictive polymers (polymers which change shape under applied electric field) generally considered the Maxwell stress to be overshadowed by field-induced intramolecular forces. For this reason, and since the electrostriction is a result of external electrostatic forces, rather than internal intramolecular forces, any sufficiently soft dielectric material may in theory exhibit actuation under an applied electric field. Later work by Pelrine et al. demonstrates actuation strains and pressures similar to that of mammalian muscle tissue, on the order of 32% for silicone and 1.9MPa for polyurethane, respectively [8]. Morover, Pelrine noted that such dielectric elastomer actuators exhibit none of the deficiencies of some other artificial muscle technologies, such as limited strain in piezoelectrics, slow response of shape memory alloy, and high voltage required for conventional air-gap electrostatic devices.

$$p = \varepsilon_o \varepsilon_r E^2 \tag{1}$$

Despite the apparent benefits of dielectric elastomer actuators over conventional devices and approximately two decades of research, they have not seen widespread commercial application. In his early work, Pelrine [9] notes that dielectric elastomers typically use 1-6kV for actuation, pointing out that although good performance can be demonstrated down to a few hundred volts, very thin dielectric elastomer films are required and production yield falls significantly due to the increased risk of dielectric breakdown, especially for larger devices. A review of dielectric elastomer materials by Shankar [10] reiterates the issue of high driving voltage, as well as low blocking force due to the intrinsically soft nature of DE materials. In general, research on DE aims to improve the performance through three means:

(i) **Material**: Develop DE materials with high dielectric constant to increase actuator response, tune material stiffness for higher actuation strain or blocking force.

(ii) **Processing**: Produce thin, homogeneous layers of DE to increase electric field for a given voltage, and increase dielectric breakdown strength.

(iii) **Geometry**: Use novel geometry or smart structures to improve performance or add new functionality.

In terms of increasing the performance of DE materials, two methods are generally used. The first is investigating or synthesizing new DE materials. An example is the discovery of acrylic elastomer as a dielectric elastomer material. Pelrine discovered that acrylic elastomer (manufactured by 3M Corporation as VHB (Very High Bond) adhesive) can be used as a dielectric elastomer capable of attaining strains in excess of 100%, much higher than the previous frontrunner for actuation strain, silicone. However, the discovery and synthesis of new DE materials is not trivial. Another method is to improve the behavior of existing materials, typically by increasing its dielectric constant. One such example is molecular grafting of organic dipoles in PDMS (polydimethylsiloxane) by Kussmaul [11], which increased the dielectric constant a maximum of twofold (3.0 to 5.9) and decreased the elastic modulus fourfold (1900 to 550 kPa), resulting in actuation strain six times that of the original material.

Another such example of material enhancement is the production of highly electrostrictive terpolymers from PVDF (polyvinylidenefluoride), a well-known ferroelectric polymer. Bauer [12] describes the synthesis of a P(VDF-TrFE-CFE) (poly(vinyldeneflouride-thrifluoroethylene-chlorofluoroethylene)) terpolymer exhibiting the highest known dielectric constant for polymers (50), resulting in higher electrostrictive strain (>7%) despite the relatively high elastic modulus (>0.3 GPa). Further modification by Le [13] by doping the terpolymer with a plasticizer, DEHP (bis (2-ethylhexyl) phthalate) realizes an extreme increase of dielectric constant of 16-fold (820) at low frequency, and its elastic modulus is approximately halved. An approximately 28-fold increase in strain was observed, however, at the cost of decreased dielectric breakdown strength, and a tendency for the electric field to saturate at levels much lower than “neat” PVDF terpolymer (6.7 V/μm vs. 50 V/ μm).

Acrylic elastomers such as VHB have been proven to exhibit huge strains and moderate stresses, and electrostrictive polymers like PVDF terpolymer are capable of the highest blocking stress

among polymers (10 to >100 MPa [10]) and moderate strains. These two materials arguably represent the highest-performance DE materials available. There may be some debate as to whether PVDF terpolymer can be considered a DE material, as they are often classified as "relaxor ferroelectric polymers," due to the fact that the primary mechanism of actuation in neat PVDF is due to internal intramolecular forces, not Maxwell stress. Indeed, Pelrine [8] notes the blurry boundary between electrostrictive and electrostatically actuated transducers, since the strain of both types is typically a function of the square of the induced electric field. Le [13] deduced that the Maxwell strain is the dominating mechanism in PVDF terpolymer, since its strain has been shown to match the theoretical values described by the Maxwell effect in (1), at least up to the saturation of the electric field.

Various methods have been investigated to produce multilayer DEA consisting of stacked layers of thin DE with homogeneous thickness, including additive and subtractive processes. Only the former will be investigated here, as the subtractive processes, generally involving microfabrication, are limited to micrometer-scale transducers [14]. Among the additive processes are spray deposition, spin coating, doctor blade coating, and pneumatic deposition. Araromi [15] reported a multilayer unimorph DEA fabricated using an airbrush for spray deposition. Although spray deposition produces a Gaussian thickness distribution, multiple depositions were shown to result in more uniform thickness profiles. Despite the uniformity of the DE layers, their thickness was limited to approximately 80-100 μm, necessitating driving voltages on the order of 1-2 kV. Lotz [16] detailed a process using spin coating for DE deposition and spray deposition for electrode deposition, resulting in DE layers well under 100 μm, as thin as 5 μm. Duduta [17] used a similar process for DE deposition by spin coating, but instead substituted the electrode spray deposition for a stamping method. Choi [18] used a variation of the doctor blade technique, where elastomer layers are coated on a glass plate by doctor blade and debonded from the substrate by water diffusion, and laminated into a multilayered structure through hot rolling. Homogeneously thick layers are produced, with an average thickness of 1.49 μm. Risner [19] offers a preliminary study into using inkjet printing and pneumatic dispensing for DEA fabrication. Thin (~2 μm) and high resolution (< 1mm) structures were made with inkjet printing, although useful free-standing structures could not be made due to the inability to remove them from their stiff glass substrate. Pneumatic dispensing was shown to be feasible to produce elastomeric structures, however demonstration of their actuation is never realized.

Each of the additive processes for DEA fabrication have their own advantages and disadvantages. Spray deposition generally produces relatively thick DE layers, on the order of 100 μm. Spin coating can produce thinner DE layers, however it is not possible to create non-circular geometries such as electrodes and electrical traces with this technique. Similarly, doctor blade coating cannot easily form shapes with controlled geometries. All of the aforementioned techniques are not discriminatory in the area or shape of the layer being deposited, and thus require masking, or multiple deposition processes to produce the controlled geometries needed for more complex DEA. Moreover, since the shape is not easily controlled in these processes, the excess material is wasted. Techniques such as inkjet printing and pneumatic deposition potentially allow for greater control over the shape of the DEA, without depositing excess material. However, fabrication of DE transducers from start-to-finish using either of these devices is not well documented.

There are various geometries of DEA being investigated, including planar [8], "spring roll" [20], and bending actuators [21], to name a few. Of particular interest is the bending actuator, which consists of a laminate of one or more DE layers, each sandwiched between two compliant electrodes, bonded to one or more rigid passive layers. Planar expansion of the DE laminate under applied voltage is constrained on one face by the elastic layer, resulting in bending of the entire structure in the direction of the passive layer. A bending actuator with a single DE laminate and single passive layer is classified as a unimorph actuator. Utilizing two or more DE laminates and passive layers to obtain bidirectional motion is classified as a bimorph, or multimorph actuator. Such structures are of particular interest because of their inherent softness and large out-of-plane displacement. The latter property is especially advantageous in the field of DEA, since most DEA require a constant prestretch to be applied for large actuation, necessitating a stiff and potentially bulky frame.

Some of the disadvantages of DEA as soft actuators are their lack of a catch state, requiring constant voltage to be applied to hold a constant deformation, and their inherent softness, which means that they are easily deformed by external loads. One way of mitigating those issues is by combining DEA with variable-stiffness materials. Shintake [22] reported on a variable stiffness DEA (VSDEA) consisting of a unimorph actuator, where the passive layer is a PDMS channel filled with Wood's metal, a low-melting point alloy (LMPA). When the LMPA is heated above

its melting point (47°C) by Joule heating, the VSDEA becomes about 90 times softer than its solid state. The increase in stiffness when cooled can be used as a catch state where the DEA can firmly grasp an object after its initial deformation. However, some limitations include the toxicity of the LMPA (containing lead, bismuth, tin, and cadmium), potential fragility and leakage of the LMPA-containing layer, and the slow rate of heating and cooling (~30s). Pelrine [23] described a variable stiffness DE device based on electrostatic devices, later coined an "electrolaminate." Such electrolaminate structures consist of stacked "leaves" each consisting of one dielectric elastomer layer and one compliant electrode. When no voltage is applied, the electrolaminate is in a low-stiffness state as the leaves are not firmly bonded to one another, so they can easily slip and buckle. When opposite charges are applied to adjacent leaves, they are compressed by electrostatic forces, making the structure stiffer. The stiffness change, although not as great as the phase change of the LMPA, can occur quickly (<1s) and is not binary, so that the stiffness can be more easily tuned. Electrostatic attraction has also been used in DEA to lift objects much greater than their generative force would allow, as demonstrated by Shintake [24].

2.2 Modeling of dielectric elastomer actuators

The key equation for DEA modeling is the Maxwell strain (1), which dictates the deformation of the DE material as a function of the square of the applied voltage. However, the intrinsic softness of DE materials introduces a couple of challenges for DEA modeling, namely their strongly nonlinear stress-strain behavior, and highly viscoelastic behavior. As a result, the literature contains many references to modeling of DEA through numerical simulations. Zhang's analysis [25] is typical of most numerical modeling approaches, describing a planar DE membrane under various modes of mechanical loading, modeled using hyper-visco-elastic material (using the Neo-Hookean model and the standard viscoelastic model respectively) and the Euler-Lagrange equation to solve the nonlinear dynamics problem. However, this and other analyses typically describe the actuation of planar actuators, whereas the behavior of unimorph actuators is expected to be quite different.

Araromi's modeling of multilayer unimorph DEA [21] points out that although fundamental analytical models of bending DEA exist, they do not account for unconventional actuator configurations, especially those consisting of large numbers of layers and inhomogeneous layer geometries. However, Araromi's numerical analysis, based on a finite element model in

ABAQUS relies on piezoelectric elements negating all viscous effects. As such, time-dependent behavior of the DEA is not predicted. Lai [26] developed a numerical model of multilayer unimorph DEA, incorporating hyperelasticity based on the Ogden model, though still not incorporating time-dependent effects. Lai also proposes a closed-form equation for the displacement of DEA based on Timoshenko beam theory, noting though that deviation at higher driving voltages occurs because of material non-linearity. In general, linear elasticity appears to be a good assumption for unimorph actuators due to the small strains exerted, especially for stiffer materials than VHB such as silicone [21].

Considering that numerical schemes are the common denominator for the above modeling schemes, it is not a far stretch of the imagination to incorporate viscoelasticity into a framework such as ANSYS of ABAQUS. However, from Araromi and Lai's analyses, it is clear that that the current limitations of existing closed-form analytical solutions are an inability to account for the viscoelasticity of the DEA materials, and geometry more complex than two planar layers. Although numerical analyses are very accessible and computation time is generally not an issue, having closed-form analytical models is beneficial, as they do not obfuscate the behavior of the system, and remeshing of a finite element model is not necessary when new geometry needs to be investigated.

2.3 Dielectric elastomer sensors

Pelrine's pioneering work on DE actuators [8] briefly ruminates on the idea of self-sensing DEA, using the change in capacitance measured across the electrodes as a means of sensing its own deformation. Indeed, research on DE sensing expanded in the following two decades to include self-sensing actuators and DE tactile, proximity, and slip sensors based on various modes of transduction, including generative, capacitive, and resistive modes.

Pelrine's own later work describes the mechanism, modeling, and construction of DE generators (DEG) [9]. DEG are dielectric elastomer transducers which convert the mechanical work done by deforming the film, into electrical energy, by increasing the voltage of the charge stored on the electrodes. To harvest energy from the DEG, a bias voltage is applied in the generator's stretched state, inducing charge on the electrodes. When the generator is contracts to its original state, the opposite charges on the opposing electrodes are moved further apart, and the like charges are compressed, increasing the electrical energy. Generally, it is assumed that the charge

on the electrodes remains constant, and in this case the voltage of the DEG can be expressed as a function of the charge and area of the electrodes (2). Large voltage swings on the order of hundreds of volts can be produced at high bias voltages (over 1kV) and large strains (in excess of 50%). Commercial availability for transistors capable of operation at high voltage is somewhat limited and contributes to increased complexity and bulk of the system. McKay [27] demonstrated a self-priming DEG with piezoresistive electrodes as integrated circuitry, to mitigate the issue of bulky electronics.

$$V = \frac{Q(volume)}{\varepsilon_o \varepsilon_r A^2} \tag{2}$$

Although the proposed use for such DEG is for energy harvesting, it is feasible that a similar mechanism could be used for a strain-sensing DES, especially where large voltage swings are desired. However, DEG seem better suited for situations with large strains and high bias voltage. These facts combined with apparent limitations in DEG driving electronics remain limitations for potential sensors of this type.

Measuring the voltage swing of an initially charged DE transducer represents only one means of DE sensing. Examples of DE sensing by measuring the change in the impedance of the DE are abundant. Resistance changes in a DE transducer may occur in the compliant electrode during expansion, where percolation effects can cause the resistivity of the electrode to increase. Capacitance between the electrodes occurs as a result of area increase or gap separation during deformation. Inductance changes can also be observed, if certain fillers are introduced to a DE matrix. The following paragraphs will focus on DE sensors based on impedance change.

One interesting alternative to simply adding sensors to actuators is the concept of self-sensing dielectric elastomer actuators. In such actuators, no additional devices are needed to sense its position or deformation. One obvious advantage of such self-sensing devices is its ability to process closed-loop control without the bulk and complexity of additional sensors. This property could prove very useful in robotic systems with many degrees of freedom which would be otherwise burdened by heavy sensor such as encoders or transducers. Moreover, in some situations (such as MEMS), the use of traditional feedback systems is impossible.

To date, to types of self-sensing DEA have been investigated: a resistive type and a capacitive type. The first type, investigated by O'Brien [28] operates by measuring the change in resistance under expansion and contraction of the DEA's external electrodes. Under an applied voltage, the combination of Maxwell strain and Poisson's effect causes the compliant electrodes to undergo positive area strain. Due to percolation effects of the carbon powder electrodes used, the resistance decreases. Then, using a voltage divider circuit, the resistance change of the electrodes is translated into an output sensing voltage which can then be used to determine position of the DEA. The current flowing out of the ground plane of the actuator was measured and used to differentiate between the sensor voltage and driving voltage. This type of self-sensing DEA has several notable advantages, including tolerance of high voltages, the ability to isolate the sensing voltage from the driving voltage, and simplicity. However, it suffers from fairly poor accuracy - up to 20% error due to a 5-10 second lag during step function driving, and about 5% after the lag period. In addition, creep of the electrodes caused decreased accuracy over time.

A second type of self-sensing DEA developed by Jung [29] relies on changes in electrical characteristics of the elastomer, instead of the electrodes. By modeling the DEA as a simple capacitor, it can be noted that a capacitance change occurs under an applied voltage, due to an increase in electrode area and decrease in gap thickness. This capacitance change can be measured by using the DEA as a capacitive element in a high-pass filter circuit, where the input to the circuit is a low frequency, high amplitude actuation signal superimposed with a high frequency, low amplitude sensing signal. Since the sensing signal is small (100-300V) compared to the driving signal (1-2kV), it has little effect on the actuation. Moreover, the driving signal is not transmitted through the high pass filter if a sufficiently low frequency is used. The self-sensing property of this system is realized because the DEA's capacitance increase under applied voltage reduces the cutoff frequency of the high-pass filter, increasing the output voltage amplitude of the sensing signal screened by the filter. Experimental results showed a high degree of accuracy, compared to the resistive self-sensing DEA.

The self-sensing actuators discussed in the previous section are used only for simple measurements, for instance the overall displacement or strain of the actuator. Although this is a useful capability, it does not provide spatial resolution (e.g. Which part of the actuator is making contact with the object?) or tactile feedback (e.g. How much force is applied to the object, and is

it firmly grasped or slipping?), which are all attributes expected of artificial skin, and necessary input data for robotic manipulation of objects. For this reason, “standalone” DES – dedicated DE sensors which perform only sensing and no actuation – are needed.

Kim [30] reported on a “flexible fingertip tactile sensor” which provides high spatial resolution (2 mm) pressure sensing over a curved surface. The sensor array is a simple capacitive DE sensor which uses the compression of the DE under normal force to induce a capacitance change, which is measured by a capacitance-to-digital converter (CDC). The standout feature of this sensor lies in its construction. A series of discrete electrodes are deposited on a fingertip-shaped object, and then the DE layer is deposited by dip coating, followed by a conductive silicone common ground electrode deposited by dip coating. The result is a tactile sensor that conforms to a complex surface, with a high degree of spatial resolution.

Numerous sensors have been developed to measure shear forces, in contrast to the sensor developed by Kim, which measures only tactile forces normal to the sensor surface. A sensor developed by Hwang [31] utilizes a fingerprint-like structure with “micro-bumpers” perpendicular to the sensor’s surface. The surface of these micro-bumpers is coated with graphene to form an electrode. When a shear force acts on the surface, the bumpers shear and touch, forming a shorter conductive path, which decreases the surface resistivity. A sensor developed by Kim [32] uses a DE sensor with a segmented cathode and common anode, where the overlap of the cathode and anode electrodes varies with the shear loading. By the change in capacitance due to the change in overlapping area of the electrodes, the magnitude and direction of the shear force can be determined. A sensor developed by Tiwana [33] uses a conductive fiber encapsulated in silicone and a cylindrical electrode concentric to the fiber to measure the magnitude of applied shear force.

Although there is a clear abundance of DE sensors to detect tactile forces, including normal force and shear force, very few are able to measure the normal and shear force components of a tactile force independently. Moreover, most shear force sensors measure only the magnitude and not the direction of the force. To observe soft polymeric sensors with these desired capabilities, one must look outside the realm of dielectric elastomers. Several solutions discriminate between normal and shear tactile forces by using a protruding feature such as a hemisphere to distribute the tactile force over an array of sensing elements. The capacitive senor developed by Cheng

[34] uses various processes including soft lithography, spin coating, and E-beam deposition to form a PDMS structure with a 2x2 array of floating copper and gold electrodes. The array is attached to a PDMS dome, which distributes tactile forces over the array. By measuring the capacitance of each of the four electrodes, the sensor can determine the magnitude of the shear and normal force components. Another device, based on Flemion ionic polymer metal composite (IPMC) developed by Wang [2] places a flexible sensing array directly on the surface of a PDMS dome. When the IPMC membrane is deformed, redistribution of ions in the Flemion membrane causes a voltage increase. The IPMC membrane is segmented into four segments so that forces on each face register independently of each other.

It has been shown in this section that there is no shortage of DE sensor designs, based on various mechanisms and geometries. The concept of self-sensing shows promise for simple integration with DEA, however the inability to sense tactile forces and lack of spatial resolution are major drawbacks. Integration of DEA and tactile sensing DES with the necessary degree of resolution, and ability to discriminate between tactile normal and shear forces requires the development of a sensor array that can be easily and seamlessly integrated with the actuator part. Although the ability to discriminate between tactile normal and shear forces has been demonstrated in other polymeric sensors, it has not yet been reported for dielectric elastomer materials. The dome shaped sensors developed by Wang and Cheng could be implemented with dielectric elastomer as the sensing element, with few of the limitations imposed by their schemes, including the leakage of electrolyte and electrode degradation over time (in Wang's case) and extensive use of microfabrication techniques (in Cheng's case).

3. Dielectric elastomer actuators

3.1 Fabrication of unimorph DEA

Two methods were investigated for fabricating unimorph DEA: (i) construction from commercial DEA films and (ii) film deposition by robotic dispenser. Three types of unimorph DEA are fabricated in this chapter (Figure 2). These types are the flat unimorph DEA and curved unimorph DEA (producing out-of plane bending), and corrugated DEA (linear extension or contraction, depending on placement of elastic layer).

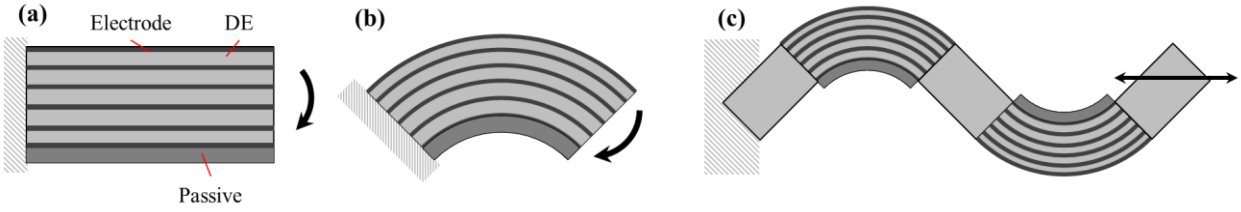

Figure 2. Schematic model of (a) flat, (b) curved, and (c) corrugated DEA.

3.1.1 Manual construction

Fabrication of DEA from commercially available films is a popular process among DEA researchers, since pre-processed DEA films are readily available. Acrylic elastomers, including 3M VHB, have seen widespread use as DEA material due to its compliance (Y = 220-450 kPa) and moderate dielectric constant (ε_r = 4.7) which allow for strains in excess of 100%. Its self-adhesive nature allows for lamination into multilayer actuators, and for carbon powder electrodes to be easily on its surface by brushing, stamping, or spray deposition [35]. A carbon powder (Ketjenblack EC-600) was used as the electrode material. The passive material was cellophane tape (3M 810 Magic Tape), since it is self-adhesive, relatively thin (50 µm) and stiff (2 GPa) compared to the DE material.

Several variations of unimorph DEA, for the purpose of verifying model results, were fabricated from 3M VHB F9469PC, a VHB film with nominal thickness of 127 µm. Although a thinner VHB film, F9460PC (50 µm) was available and could have been used in the interest of decreasing the driving voltage, it was found that the thinner film easily wrinkled and tore when the backing paper was removed, resulting in dielectric breakdown. The general scheme for fabricating the DEA is described below and illustrated in Figure 3.

1. A 25 x 50 mm piece of VHB with paper backing is fixed to a piece of PTFE film with Scotch tape.
2. A PTFE mask is applied, with a rectangular hole corresponding to the size of the electrode. For the flat DEA, the electrode size was 35 x 10 mm. For the curved and corrugated DEA, the electrode size was 8 x 10 mm.
3. Carbon powder is brushed onto the VHB surface. Excess carbon powder is removed by compressed air, and the PTFE mask is removed, forming a rectangular electrode.
4. Electrical connection is established to the electrode by a piece of self-adhesive copper tape.
5. If more than one layer is desired, another layer of VHB is laminated to the surface of the DEA. Otherwise, or when the required number of DEA has been reached, skip to step 7.
6. Steps 2-5 are repeated for the desired number of DE laminations, with the copper electrical connections placed in alternating positions, so that every other electrode is connected.
7. The passive material is applied to the top surface of the DEA.
8. The PTFE substrate and VHB backing paper is removed, and the final electrode is applied, repeating steps 2-4.
9. The excess material is trimmed, so that a 500 μm margin is left around the electrode to prevent arcing.
10. The actuator is molded to the desired shape. In the case of the flat unimorph DEA, the DEA is annealed at 100°C for 30 minutes to remove unwanted curvature from residual stresses formed during fabrication. In the case of the curved unimorph DEA, the DEA is molded around an aluminum cylinder of the desired radius (5 mm), at the same temperature and duration.

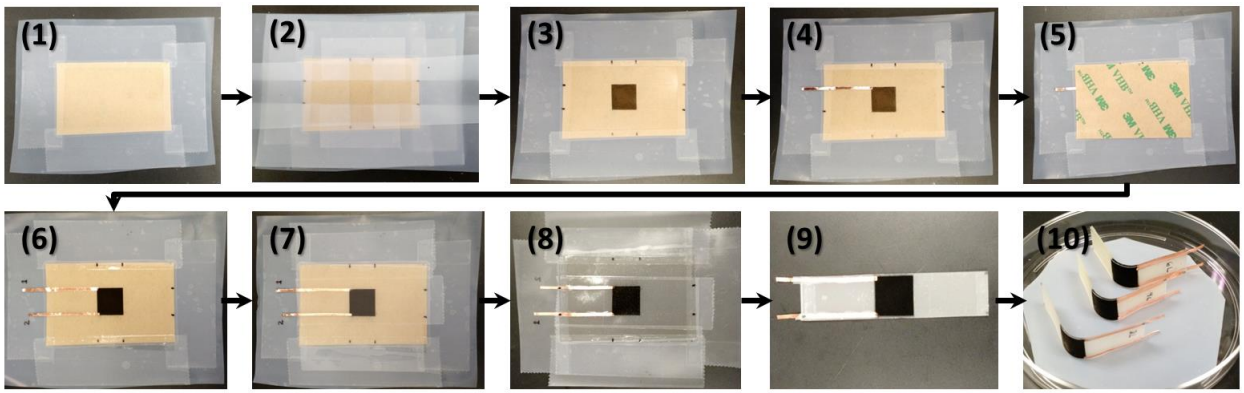

Figure 3. Fabrication scheme of flat DEA unimorph actuators from VHB film.

The corrugated DEA (Figure 4) follows a similar processing scheme with a few differences. First, the electrodes are segmented, so that the electroded area coincides with the curved segments of the DEA after molding. The segments are connected by strips of copper tape. Second, the side of the DEA covered by the passive material alternates so that it lies on the concave surface of the curved segments after molding. The placement of the passive layer causes the corrugated DEA to contract linearly upon actuation. Third, the flat DEA laminate is molded into the corrugated shape by an aluminum mold. Examples of the flat, curved, and corrugated DEA are shown in Figure 5.

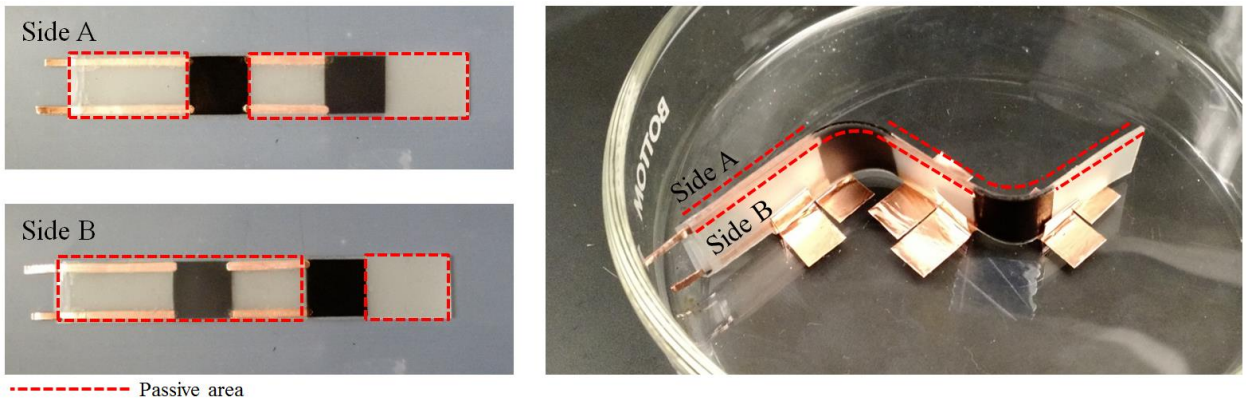

Figure 4. Corrugated DEA in flat, unmolded state showing alternating positions of the passive layer (left) and in the molded corrugated state (right).

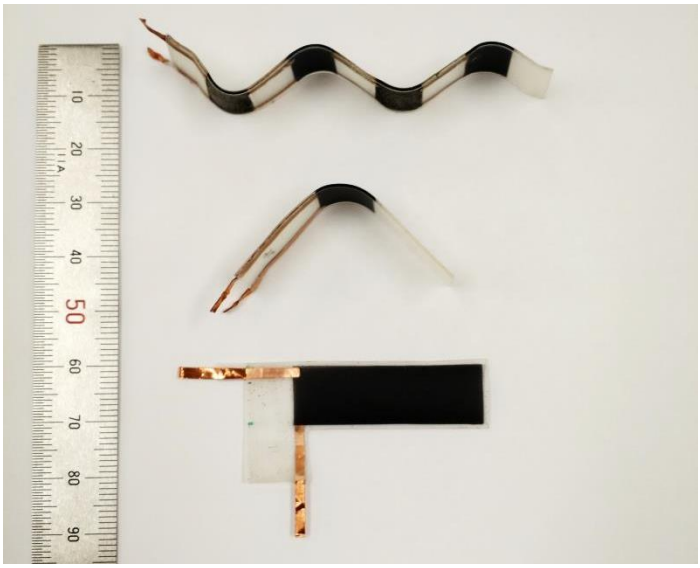

Figure 5. Examples of DEA constructed from commercial VHB film.

3.1.2 Robotic dispensing

This section details the use of a pneumatic dispenser system to deposit dielectric elastomer and electrode films. The system consists of a 3-axis robot (Musashi Engineering SHOTminiΩ_x) and a dispenser (Musashi Engineering ML-808GX). The overall setup of the dispenser system is shown in Figure 6. To dispense solutions, a syringe and needle filled with the liquid solution is mounted on the head of the 3-axis robot. The syringe is connected by an air line to the dispenser, which produces air pressure (5-200 kPa) to force the liquid solution through the needle and onto the substrate.

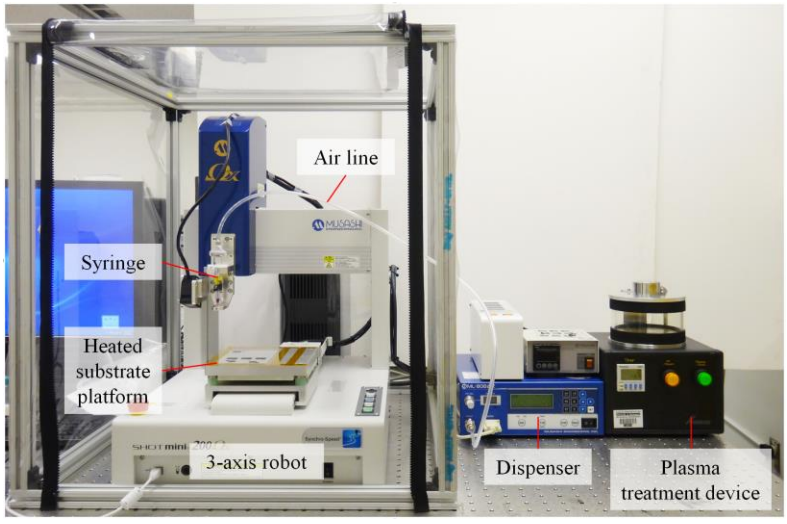

Figure 6. Robotic dispenser system and plasma treatment device.

The thickness and quality of the films produced depend heavily on the deposition parameters used. For a given film of desired material, thickness, and shape, the parameters below must be determined, often by a process of trial-and-error.

(a) **Needle diameter** (0.34 ~ 0.13 mm)**:** The needle diameter depends on the viscosity of the solution and the feature size desired. To produce smaller features such as electrical traces, or when a low viscosity solution is to be dispensed, a smaller needle is desired. On the other hand, clogging of the needle by particulates and high dispensing pressure for highly viscous solutions can be mitigated by larger needles.

(b) **Deposition pressure** (5 ~ 200 kPa)**:** Deposition pressure and needle diameter are interdependent, as the discharge rate depends on both pressure and area.

(c) **Needle-to-substrate distance** (typically 50 – 100 μm)**:** Holding the needle too close to the surface of the substrate prevents the solution from flowing freely, and too far may produce droplets instead of a contiguous film.

(d) **Scanning speed** (0.1 ~ 800 mm/s)**:** The amount of solution deposited depends on the scanning speed (speed at which the needle traverses the substrate) and discharge rate. Another issue associated with scanning speed is acceleration; if the discharge rate is held constant, more solution is deposited in areas in which the needle is accelerating and decelerating.

(e) **Scanning pitch** (>0.01 mm): The scanning pitch refers to the distance between each line in the needle's path. Smaller pitch generally results in smaller variation in film thickness, but takes more time and deposits more solution in a given area.

(f) **Substrate temperature** (<100°C): The temperature of the substrate affects the rate at which the solvent evaporates, producing a solid film. If the temperature is low, it may be necessary to wait for the film to solidify between successive operations. If the temperature is too high, the film may solidify during dispensing, clogging the needle.

In this work, PVDF terpolymer (P(VDF-TrFE-CFE), Piezotech) was used as the dielectric elastomer. As stated in the literature review, PVDF terpolymer generates high stresses and moderate strains, because of its high dielectric constant (50) and moderate elastic modulus (~0.3 GPa). The liquid solution used to deposit the DE layers was P(VDF-TrFE-CFE) 10 wt% dissolved in methyl ethyl ketone (MEK). The electrode material is also of vital importance to the

DEA performance. The electrode's stiffness must be low enough to prevent adding appreciably to the bending stiffness of the DEA, which would make the actuator inflexible. At the same time, it must be conductive; low conductivity generally reduces the response time of the DEA. Unlike the VHB DEA, the PVDF DE is not self-adhesive, so carbon powder simply deposited onto the surface would diffuse into any subsequently deposited liquid solution, resulting in dielectric breakdown. Therefore, the conductive filler must be mixed into a flexible matrix. To this end, a 2:1 (by weight) mixture of aqueous multi-walled carbon nanotube (MWCNT) and silicone emulsion polymer (KM2002L-1, Shin Etsu Corp.) was used. The MWCNT solution consisted of 4 wt% MWCNT (Nanocyl SA.) dispersed in water. Although other flexible matrixes were investigated, including styrene butadiene rubber (SBR) and metallocene butadiene rubber (MBR), silicone yielded the lowest stiffness and best chemical resistance against MEK (the DE solvent). Again, 3M 810 Magic Tape was used as the passive material. A summary of material properties of the DEA is tabulated in Table 1.

Table 1. Material properties of DEA materials.

	Young's Modulus [MPa]	Dielectric Constant	Sheet Resistance [kΩ/sq.]
P(VDF-TrFE-CFE)	390	50	-
Nanocyl [1.3 wt%] + H_2O [32 wt%] + KM-2002L-1 [66.7 wt%]	4.9	-	0.37
3M 810 Magic Tape	1660	-	-

Wettability of the deposition surface is important for depositing thin, homogeneous layers. When liquids are dispensed on a strongly hydrophobic surface, the contact angle between solution and substrate is large, and a contiguous film may not be formed. Materials such as PVDF terpolymer tend to be hydrophobic, so a method of increasing surface wettability is desirable. To this end, plasma treatment can be used to microscopically roughen the deposition surface by bombardment of high-energy molecules. A Sakigake YHS-R desktop plasma treatment device was used to treat the deposition surface between each round of dispensing. On trials with PVDF terpolymer, 20 µL droplets of electrode solution and deionized water were deposited by a micropipette. Plasma treatment of 120-180 seconds yielded the greatest increase in wettability, as shown in Figure 7, which shows the contact angle θ as a function of the duration of plasma treatment, where θ is defined as the interior angle between the periphery of the droplet and the substrate.

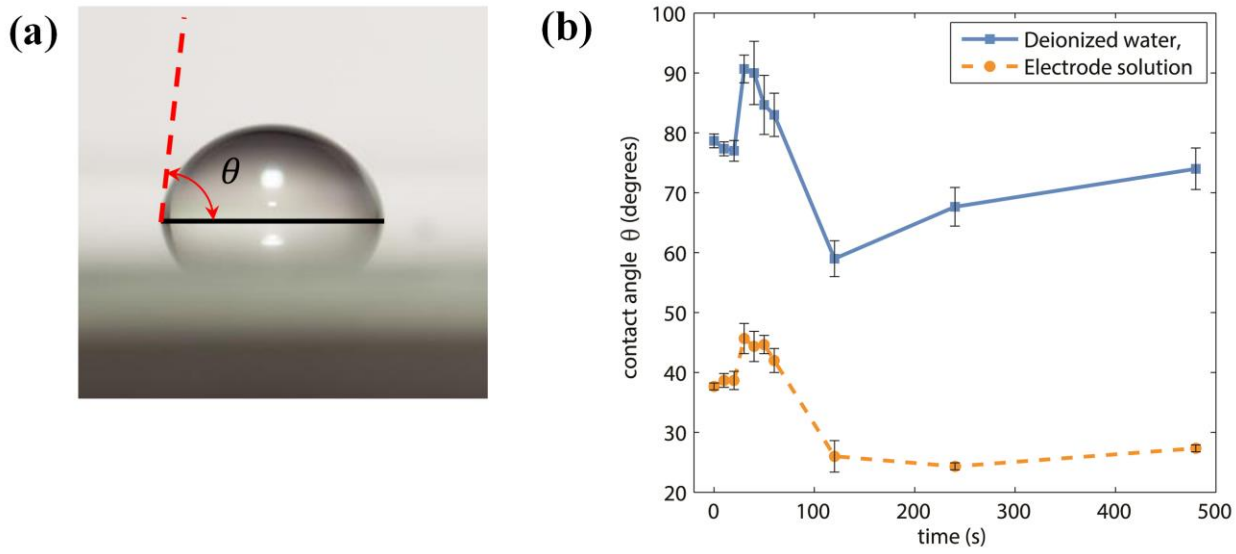

Figure 7. (a) Definition of contact angle θ, (b) Contact angle of electrode solution and deionized water (DIW) on P(VDF-TrFE-CFE) + 15wt% DEHP.

The dispensing scheme, needle path, and dispensing parameters are shown in Figure 8. A schematic model of the completed DEA is shown in Figure 9. The deposition substrate was a glass slide heated to 25°C by the heated platform of the 3-axis robot. Elevated temperature was not required because the MEK in the PVDF solution evaporates rapidly even at room temperature. The first layer is a thin DE layer, which acts as a release layer, since the silicone-based electrode material adheres strongly to glass. Note that two deposition pressures are used, a lower pressure for when the needle is moving slowly while changing direction, and a higher pressure for when the needle is moving at constant speed. Following plasma treatment, the first electrode is deposited. There are two electrode patterns, so that the every other electrode is connected in an interdigitated arrangement. A DE "fill layer" is added around the perimeter of the electrode, to provide a level surface for the subsequent DE layer to be deposited. The second electrode, with the opposite pattern as the first, is deposited, along with another DE fill layer and DE layer. This process can be repeated any number of times to produce multilayered DEA laminates. Actuators consisting of 2, 4, 6, 8, and 10 layers were constructed.

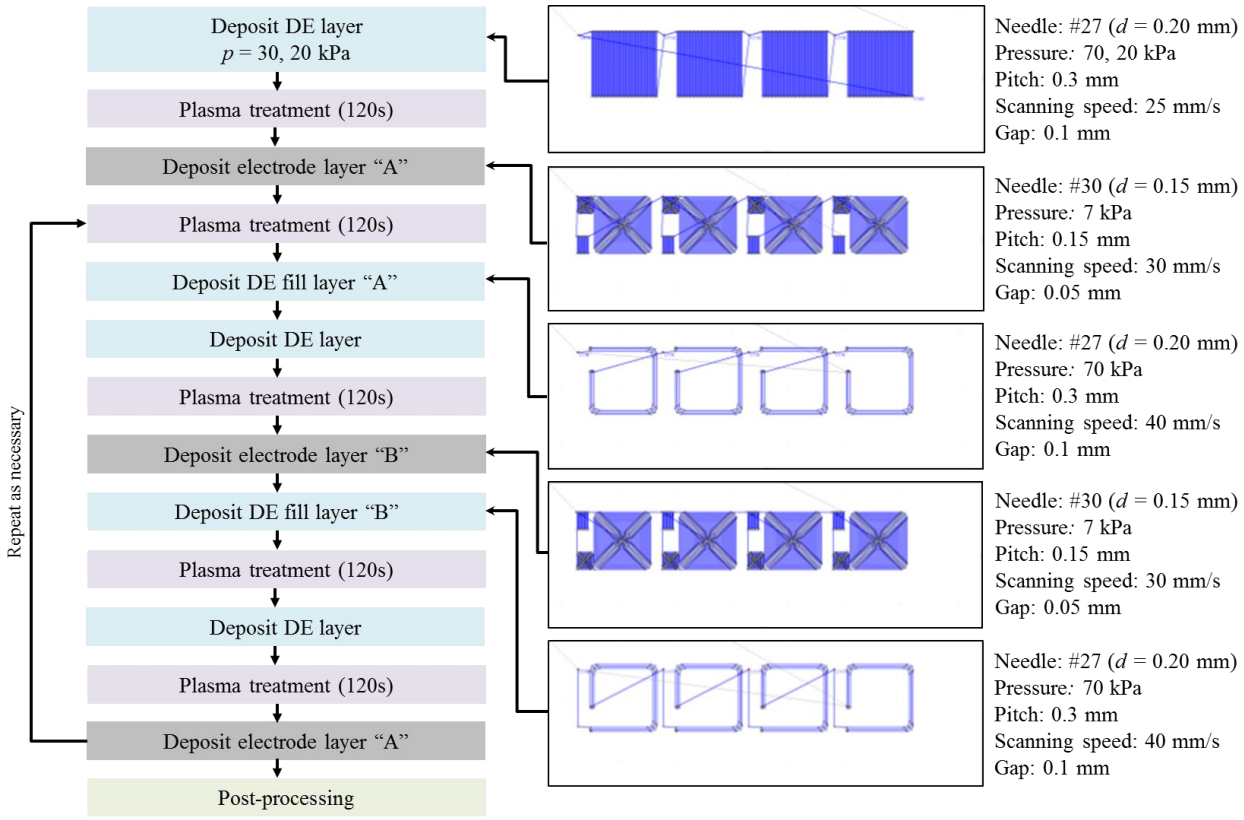

Figure 8. Dispensing scheme of dispenser-fabricated DEA.

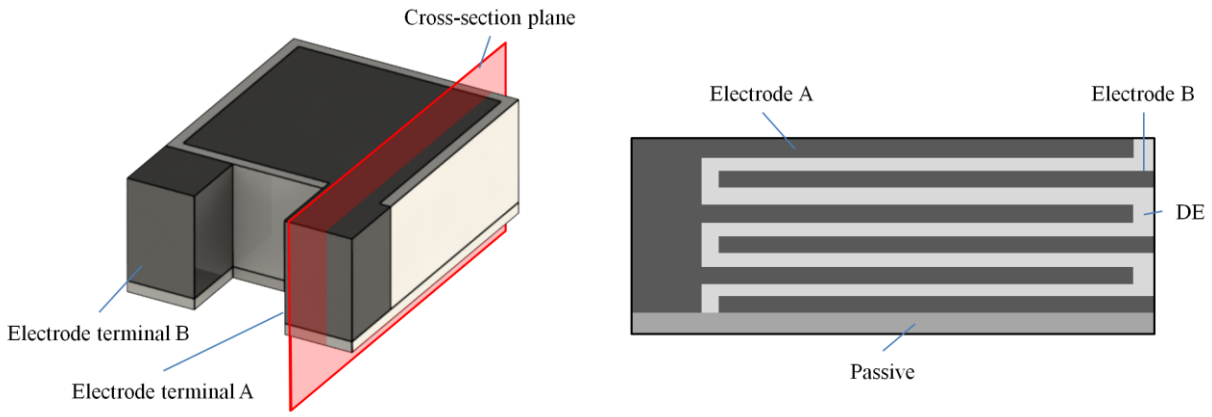

Figure 9. Schematic model and cross-sectional view of a 6-DE layer unimorph DEA (not to scale).

Following the dispensing steps, a number of post-processing steps are needed, shown in Figure 10. The DEA laminate can be easily removed from the glass substrate because of the DE release layer. The laminate is dried for 10 hours at 40°C, then annealed at 90°C for 1 hour to remove residual stresses. The passive layer (3M 810 Magic Tape) is adhered to one side of the DE

laminate, and then excess material is trimmed. Finally, the electrodes are connected electrically by self-adhesive copper tape, and the end of the actuator is potted in epoxy and mounted on a glass slide for ease of handling.

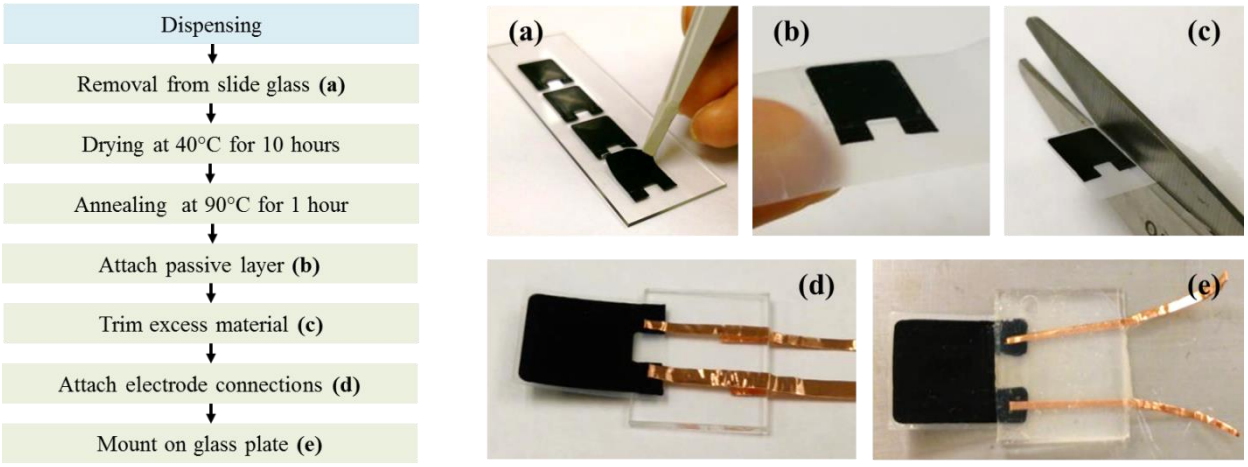

Figure 10. Post-processing scheme of dispenser-fabricated DEA.

Using this processing scheme, DEA with as many as 10 DE layers were fabricated, with typical DE layer thickness of 10 µm and electrode thickness of 15-25 µm. The average thickness of the DE and electrode layers is tabulated in Table 2. The processing time to produce 4 DEA each consisting of 10 DE layers each on a single glass substrate is approximately 3 hours (except for post-processing operations such as drying and annealing time).

Table 2. Average thickness of DEA layers.

	# of DE layers				
	2L	**4L**	**6L**	**8L**	**10L**
Electrode thickness [µm]	9	9	10.5	11.5	12
DE thickness [µm]	20	28	18	18	15

3.2 Elastic modeling of unimorph DEA

3.2.1 Elastic modeling of flat unimorph DEA

This model is based on the pioneering work on modeling of a unimorph piezoelectric bender by Smits [5] who used a thermodynamic method to evaluate the load-displacement behavior. Weinberg [36] and Dunsch [37] later extended the model to multilayer actuators and considered a unified approach to for various actuator geometries, loading, and boundary conditions respectively. This model can be adapted to model a dielectric elastomer unimorph actuator, by

replacing the piezoelectric eigenstrain in the original formulation with the Maxwell strain exhibited by dielectric materials. This study considers a multilayer actuator consisting of n laminae in the cantilever configuration shown in Figure 11. The actuator is fixed at $x = 0$, with a concentrated load P acting at its free end at $x = L$. Other configurations can be considered using the unified model discussed by Dunsch [37]. Curved beam sections can also be considered.

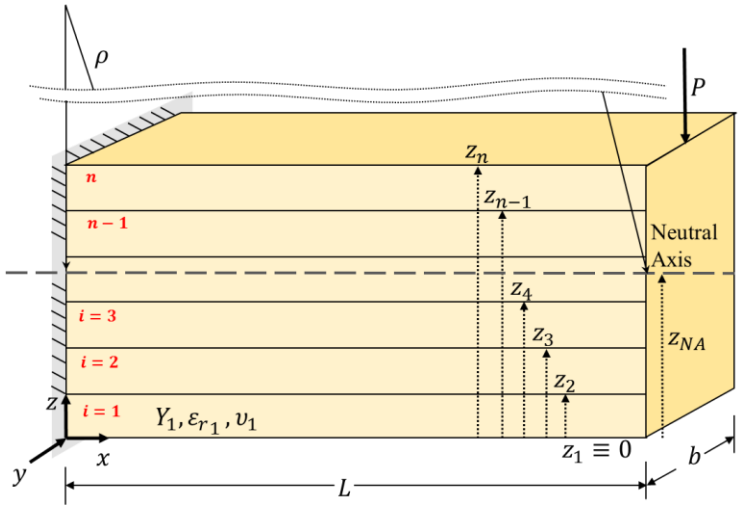

Figure 11. Model of multilayer unimorph actuator.

The assumptions in this model are the same as those used by Smits [5]: (i) static force equilibrium, (ii) Euler-Bernoulli beam theory holds, (iii) no slip occurs at the bonding surface.

The general expression for strain along the x-direction in the i-th lamina (3) is the sum of the elastic strain, and Maxwell strain induced by an electric field (4), where υ is Poisson's ratio, Y is Young's modulus, ε_o is vacuum permittivity, ε_r is relative dielectric constant, and E is the applied electric field. The electric field can be approximated by two parallel plates, i.e. $E = V/(z_{i+1} - z_i)$.

$$\varepsilon_i = \varepsilon_{i_{elastic}} + \varepsilon_{i_{Maxwell}} \tag{3}$$

$$\varepsilon_{i_{Maxwell}} = \upsilon_i \frac{\varepsilon_0 \varepsilon_{r_i}}{Y_i} E^2 = \upsilon_i \frac{\varepsilon_0 \varepsilon_{r_i}}{Y_i (z_{i+1} - z_i)^2} V^2 \tag{4}$$

Assuming linearly elastic materials (or sufficiently small strain), the elastic strain is simply denoted $\varepsilon_{i_{elastic}} = \sigma_i / Y_i$ and the total strain in each lamina is expressed as (5). From assumption

(ii), the strain distribution in the z-direction is linear (6), which automatically satisfies assumption (iii). In (6) ε^0 is the neutral axis strain, z' is the distance from the neutral axis, and ρ is the radius of curvature.

$$\varepsilon_i = \frac{\sigma_i}{Y_i} + \upsilon_i \frac{\varepsilon_0 \varepsilon_{r_i}}{Y_i (z_{i+1} - z_i)^2} V^2 \tag{5}$$

$$\varepsilon_i = \varepsilon^0 - \frac{z'}{\rho} \tag{6}$$

Assuming no axial load is applied, $\varepsilon^0 = 0$. Using the bottom of the unimorph as $z = 0$ and z_{NA} as the location of the neutral axis, (6) becomes (7). By substituting (7) into (5) and solving for σ_i, a general expression for stress in each lamina is obtained (8). For a non-electroactive layer such as an electrode or elastic layer, $\varepsilon_{r_i} = 0$.

$$\varepsilon_i = \frac{z_{NA} - z}{\rho} \tag{7}$$

$$\sigma_i = Y_i \left(\frac{z_{NA} - z}{\rho} - \frac{\upsilon_i \varepsilon_o \varepsilon_{r_i}}{Y_i (z_{i+1} - z_i)} V^2 \right) \tag{8}$$

Given assumption (i) and constant width b, the summation of forces (9) and moments (10) in each layer are equated to zero. In the moment expression, the moment due to voltage induced-stress and an external moment M_b are superimposed. For a concentrated load at $x = L$, $M_b = P(L - x)$.

$$\sum F = \sum_{i=1}^{n} b \int_{z_i}^{z_{i+1}} \sigma_i dz = \sum_{i=1}^{n} b \int_{z_i}^{z_{i+1}} Y_i \left(\frac{z_{NA} - z}{\rho} - \frac{\upsilon_i \varepsilon_o \varepsilon_{r_i}}{Y_i (z_{i+1} - z_i)} V^2 \right) dz = 0 \tag{9}$$

$$\sum M = \sum_{i=1}^{n} b \int_{z_i}^{z_{i+1}} \sigma_i z dz + M_b = \sum_{i=1}^{n} b \int_{z_i}^{z_{i+1}} Y_i \left(\frac{z_{NA} - z}{\rho} - \frac{\upsilon_i \varepsilon_o \varepsilon_{r_i}}{Y_i (z_{i+1} - z_i)} V^2 \right) z dz + P(L - x) = 0 \tag{10}$$

The equilibrium equations represent a system of two equations in two unknowns, z_{NA} and ρ. From the assumption of Euler-Bernoulli beam theory (ii), the displacement of the actuator $w(x)$ is related to ρ by the relation $\partial w(x) / \partial x = 1 / \rho(x)$. The appropriate boundary conditions for the

fixed-free configuration are $\partial w(0)/\partial x = 0$ and $w(0) = 0$. By solving (9) and (10) for ρ, and integrating $1/\rho$ twice with respect to x using the appropriate boundary conditions, the tip displacement δ can be expressed as a function of applied voltage V and tip load P (11)-(14).

$$\delta = \alpha P + \beta V^2 \tag{11}$$

$$\alpha = -\frac{\sum_{i=1}^{n} L^3 Y_i (z_{i+1} - z_i)}{3bK} \tag{12}$$

$$\beta = \frac{L^2\left(\sum_{i=1}^{n} Y_i (z_{i+1} - z_i) \sum_{i=1}^{n} \frac{\upsilon_i (z_{i+1} + z_i) \varepsilon_{r_i} \varepsilon_o}{2(z_{i+1} - z_i)} - \sum_{i=1}^{n} \frac{1}{2} Y_i \left(z_{i+1}^2 - z_i^2\right) \sum_{i=1}^{n} \frac{\upsilon_i \varepsilon_{r_i} \varepsilon_o}{z_{i+1} - z_i} \right)}{2K} \tag{13}$$

$$K = \left(\sum_{i=1}^{n} \left(\frac{1}{2} Y_i z_{i+1}^2 - \frac{1}{2} Y_i z_i^2 \right) \right)^2 - \left(\sum_{i=1}^{n} Y_i (z_{i+1} - z_i) \right) \sum_{i=1}^{n} \left(\frac{1}{3} Y_i z_{i+1}^3 - \frac{1}{3} Y_i z_i^3 \right) \tag{14}$$

The blocking force (reaction force generated when the actuator's tip is held at zero displacement) is determined by setting $\delta = 0$ and solving for P (15).

$$P_{bl} = -\frac{\beta}{\alpha} V^2 \tag{15}$$

For a bending actuator with $L > b$, the preferred axis of bending is about the *y* axis, and bending about the *x* axis and strain along the *x* axis may be neglected. Thus, a plane strain condition may be considered by replacing Y_i and υ by their equivalent plane strain values (16), (17). A MATLAB script to evaluate the elastic model is found in Appendix D.

$$Y_{i_{plane\_strain}} = \frac{Y_i}{1 - \upsilon^2} \tag{16}$$

$$\upsilon_{plane\_strain} = \frac{\upsilon}{1 - \upsilon} \tag{17}$$

3.2.2 Elastic modeling of curved and corrugated unimorph DEA

Consider a curved multilayer actuator consisting of n laminae with subtended angle ϕ and radius of curvature ρ, shown in Figure 12. The beam is fixed on one end and the free end is subjected to moment M. Deformation of the beam is characterized by the change in subtended angle θ. The elastic model of the unimorph DEA can be expanded to model curved sections by

replacing the linear strain distribution by the strain distribution expected in a curved beam, which is hyperbolic as a function of position in the beam, r (18). Continuing along the same procedure as the straight unimorph actuator, the stress in each lamina (19) is found by substituting the hyperbolic strain distribution into (5). Equilibrium equations for force (20) and moment (21) are found by integrating along the radial direction of the curved beam. The equilibrium equations represent a system of two equations in two unknowns, ρ and θ. Solving for the change in subtended angle θ results in a constitutive relation expressing θ in terms of the square of the applied voltage, V^2 and tip moment M (22)-(25).

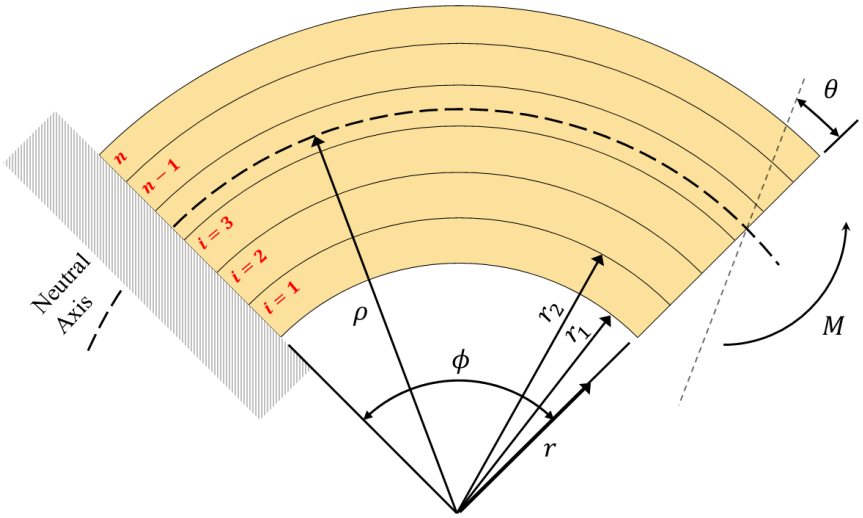

Figure 12. Model of curved multilayer unimorph actuator

$$\varepsilon_i = \frac{\theta}{\phi}\left(1-\frac{\rho}{r}\right) \tag{18}$$

$$\sigma_i = Y_i\left(\frac{\theta}{\phi}\left(1-\frac{\rho}{r}\right)-\frac{\upsilon_i\varepsilon_0\varepsilon_{r_i}}{Y_i(r_{i+1}-r_i)^2}V^2\right) \tag{19}$$

$$\sum F = \sum_{i=1}^{n} b\int_{r_i}^{r_{i+1}} Y_i\left(\frac{\theta}{\phi}\left(1-\frac{\rho}{r}\right)-\frac{\upsilon_i\varepsilon_0\varepsilon_{r_i}}{Y_i(r_{i+1}-r_i)^2}V^2\right)dr = 0 \tag{20}$$

$$\sum M = \sum_{i=1}^{n} b\int_{r_i}^{r_{i+1}} Y_i\left(\frac{\theta}{\phi}\left(1-\frac{\rho}{r}\right)-\frac{\upsilon_i\varepsilon_0\varepsilon_{r_i}}{Y_i(r_{i+1}-r_i)^2}V^2\right)rdr + M = 0 \tag{21}$$

$$\theta = \alpha M + \beta V^2 \tag{22}$$

$$\alpha = \frac{\phi \sum_{i=1}^{n} Y_i \left(\log(r_{i+1}) - \log(r_i) \right)}{bK} \tag{23}$$

$$\beta = \frac{\phi \left(\sum_{i=1}^{n} (r_i - r_{i+1}) Y_i \left(\sum_{i=1}^{n} \frac{\upsilon_i \varepsilon_i \varepsilon_0}{r_i - r_{i+1}} \right) + \sum_{i=1}^{n} Y_i \left(\log(r_{i+1}) - \log(r_i) \right) \left(\sum_{i=1}^{n} \frac{\upsilon_i (r_i + r_{i+1}) \varepsilon_i \varepsilon_0}{2(r_i - r_{i+1})} \right) \right)}{K} \tag{24}$$

$$K = \left(\sum_{i=1}^{n} (r_i - r_{i+1}) Y_i \right)^2 - \frac{1}{2} \sum_{i=1}^{n} \left(r_{i+1}^2 - r_i^2 \right) Y_i \sum_{i=1}^{n} Y_i \left(\log(r_{i+1}) - \log(r_i) \right) \tag{25}$$

With a constitutive relation between voltage, angular displacement, and moment for the curved unimorph actuator known, a relationship between voltage and length change can be determined for a corrugated actuator. Consider a corrugated actuator with A curved segments, and B straight segments with initial and deformed states shown in . The change in length of the actuator can (26) be expressed as the sum of the differences in the projected length of curved segments a and straight segments b, where the subscripts d and i denote the deformed and initial shapes, respectively.

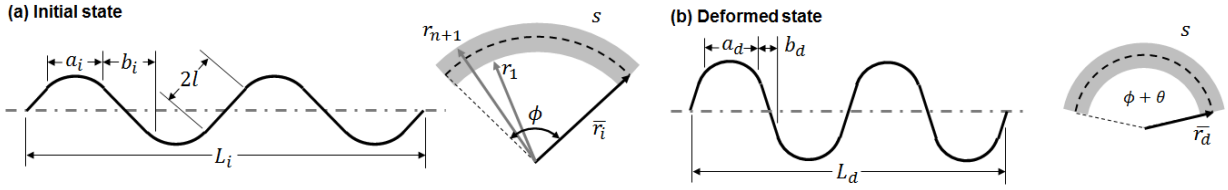

Figure 13. Corrugated actuator in ($A = 2, B = 2$) (a) initial state and (b) deformed under applied voltage

The change in projected length of the straight segment (27) depends on its half-length l and the subtended angle of the curved segment in its initial and deformed state. The change in projected length of the curved segment (28) is equal to the change in its chord length. The initial centerline radius $\bar{r}_i$ is taken as the average of the inner radius r_i and outer radius r_{n+1}. Assuming that the centerline arc length s remains constant during deformation (30) the deformed centerline radius $\bar{r}_d$ can be found. Finally, the change in length of the actuator (32) can be expressed in terms of the change in subtended angle θ, which itself is a function of voltage applied to the actuator.

$$\Delta L = A(a_d - a_i) + B(b_d - b_i) \tag{26}$$

$$b_d - b_i = 2l\left(\cos\left(\frac{\phi+\theta}{2}\right) - \cos\left(\frac{\phi}{2}\right)\right) \tag{27}$$

$$a_d - a_i = 2\left(\bar{r}_d \sin\left(\frac{\phi+\theta}{2}\right) - \bar{r}_i \sin\left(\frac{\phi}{2}\right)\right) \tag{28}$$

$$\bar{r}_i = \frac{r_i + r_{n+1}}{2} \tag{29}$$

$$s = \bar{r}_i\phi = \bar{r}_d(\phi+\theta) \tag{30}$$

$$\bar{r}_d = \frac{\bar{r}_i\phi}{\phi+\theta} = \frac{(r_i + r_{n+1})\phi}{2(\phi+\theta)} \tag{31}$$

$$\Delta L = 2A\left(\frac{(r_i + r_{n+1})\phi}{2(\phi+\theta)} \sin\left(\frac{\phi+\theta}{2}\right) - \frac{r_i + r_{n+1}}{2} \sin\left(\frac{\phi}{2}\right)\right) + 2Bl\left(\cos\left(\frac{\phi+\theta}{2}\right) - \cos\left(\frac{\phi}{2}\right)\right) \tag{32}$$

3.2.3 Comparison with experimental results

The models developed for the displacement of flat unimorph DEA (11), curved unimorph DEA (22), and corrugated DEA (32) were validated by comparison with the behavior of DEA fabricated from VHB F9469PC, discussed in Chapter 3.1. Input parameters for the flat, curved, and corrugated DEA are shown in Table 3, Table 4, and Table 5, respectively. Plots comparing the predicted and measured displacements are shown in Figure 14, Figure 15, and Figure 16. All experimental measurements of displacement were taken soon after a step voltage was applied to the actuator reached equilibrium, after 5 seconds. Note that the electrode layers were ignored in the model prediction, as the carbon black powder has negligible stiffness and thickness.

In general, good agreement with between the predicted and measured data is observed. In the case of the flat unimorph DEA, the model tends to overestimate the displacement at lower voltages. It was observed that at lower voltages (< 1kV), there are competing modes of deformation; bending along the width of the DEA, and bending along its length. At higher voltages, however, bending along the length of the DEA dominates, and the experimental data more closely matches the model predictions. Stiffening fibers could be added along the width of the DEA to prevent undesired two-plane bending.

Table 3. Input parameters for modeling of flat unimorph DEA.

	VHB F9469PC (DE)	3M Magic Tape (Passive)		Geometric Parameters
Thickness (µm)	127	50	**Length (mm)**	35
Young's modulus (MPa)	0.22	2000		
Poisson's ratio	0.5	0.35	**Width (mm)**	10
Dielectric constant	4.7	--		

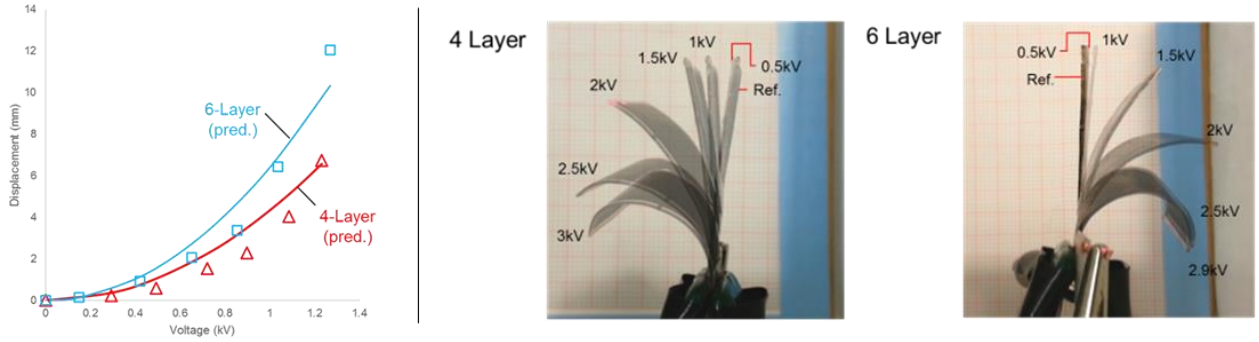

Figure 14. Model predictions and experimental results for tip displacement for 4 and 6 layer DEA.

Considering the curved and corrugated DEA, it is also noted that the model predictions corroborate well with the experimental data. The competing two-plane bending effect observed in the flat DEA was not observed here, potentially due to the initial curvature of the DEA instilling a preferred direction of bending. It is worth noting here one of the key benefits of the corrugated DEA – large contractile strains of approximately 25%, without any prestretch. This is over three times higher than the Maxwell strain developed by the DE itself (7.3%), due to amplification of that strain by the DEA's novel structure.

Table 4. Input parameters for modeling of curved unimorph DEA.

	VHB F9469PC (DE)	3M Magic Tape (Passive)		Geometric Parameters		
				2 layer	4 layer	6 layer
Thickness (µm)	127	50	**Radius of curvature (mm)**	5	5	5
Young's modulus (MPa)	0.22	2000	**Subtended angle (degrees)**	87	67	90
Poisson's ratio	0.5	0.35	**Width (mm)**	10	10	10
Dielectric constant	4.7	--				

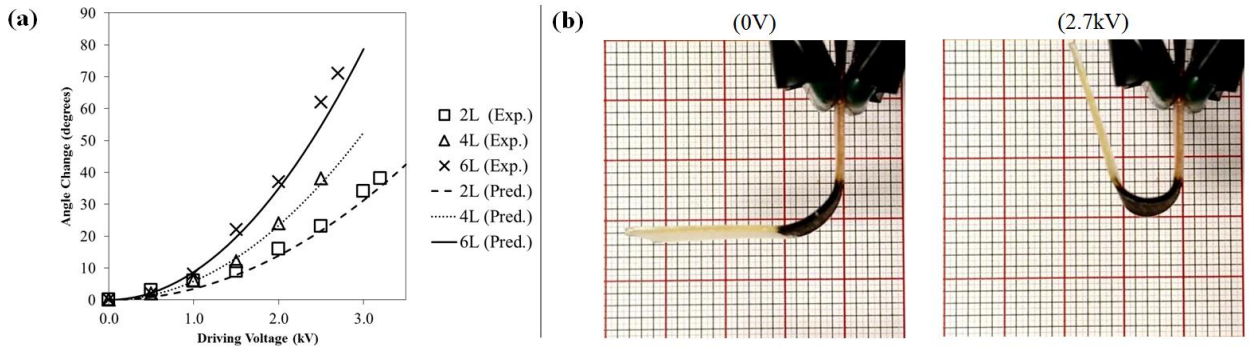

Figure 15. (a) Measured and predicted displacement of curved unimorph DEA and (b) initial (0V) and deformed (2.7kV) shape of 6-layer curved unimorph DEA.

Table 5. Input geometric parameters for modeling of corrugated DEA.

Geometric Parameters			
Number of VHB laminations	4	**Radius of curvature (mm)**	5
Number of curved segments	2	**Subtended angle of curved segments (degrees)**	90
Number of straight segments	2	**Half-length of straight segments (mm)**	7.5
		Width (mm)	10

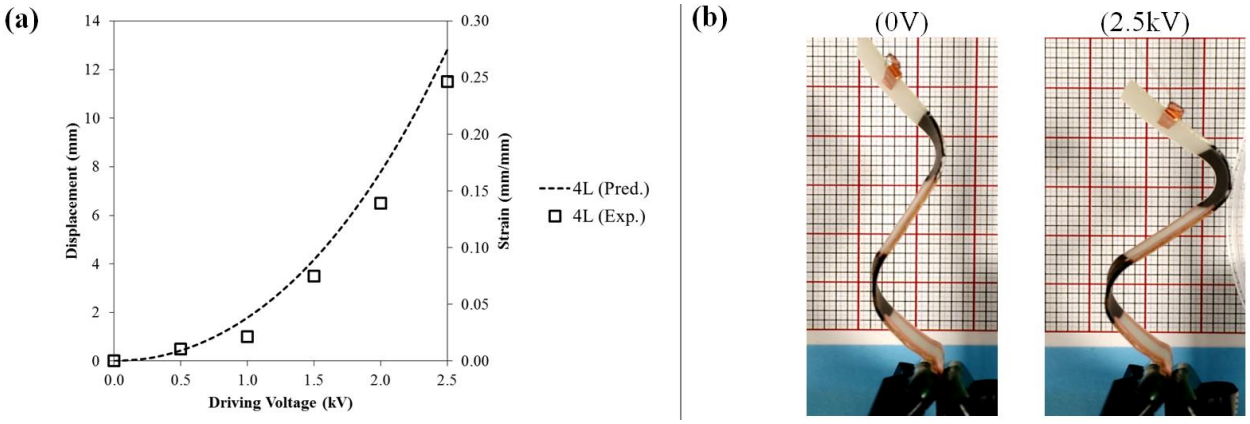

Figure 16. (a) Measured and predicted linear displacement of corrugated DEA and (b) initial (0V) and deformed (2.5kV) shape of corrugated DEA.

3.3 Viscoelastic modeling of unimorph DEA

3.3.1 Viscoelastic model development

A viscoelastic formulation for the load-displacement behavior of unimorph DEA can be obtained by applying the elastic-viscoelastic correspondence principle to the elastic formulation (11). Of particular interest are two subsets of the elastic solution, the free displacement ($P = 0$) and blocking force ($\delta = 0$).

In this formulation, linear viscoelasticity is assumed such that materials with relaxation functions $G(t)$ and creep functions $J(t)$ so that $J(t)*dG(t)=h(t)$ in the solution space, equivalent to $\overline{J}(s)\overline{G}(s)=1/s^2$ in Laplace space.

The steps to apply the elastic-viscoelastic correspondence principle are as follows:

1. Apply $\mathcal{L}$ to the elastic solution δ_e	$\mathcal{L}\{\delta_e(Y,V(t))\}=\overline{\delta_e}(Y,\overline{V}(s))$
2. Replace Y with $s\overline{G}(s)$	$\overline{\delta}_{vis}(\overline{G}(s),\overline{V}(s))$
3. Apply $s^2\overline{G}\,\overline{J}=1$	$\overline{\delta}_{vis}(\overline{J}(s),\overline{V}(s))$
4. Apply $\mathcal{L}^1$ to $\overline{\delta}_{vis}$	$\mathcal{L}^1\{\overline{\delta}_{vis}(\overline{J}(s),\overline{V}(s))\}=\delta_{vis}(J(t),V(t))$

Consider applying the correspondence principle to the free displacement equation (33). On applying the Laplace transform, it is observed that the voltage input is a function of time $V(t)$ whereas the parameter β consists of parameters invariant in time. As a result, the elastic solution in the Laplace domain is shown in (34). Although for the time being β acts as a constant, it should be noted that it contains the Young's modulus Y_i which will be acted on by correspondence principle.

$$\delta_e=\beta V^2(t) \tag{33}$$

$$\overline{\delta}_e=\mathcal{L}\{\delta_e\}=\beta\overline{V^2}(s) \tag{34}$$

The viscoelastic formulation in Laplace space $\overline{\delta}_{vis}$ is obtained by replacing the Young's modulus Y_i with the Laplace transformed creep function multiplied by the Laplace variable, $s\overline{G}(s)$ (35). The expression for β is rational, with the denominator a quadratic function of Y_i and the numerator a linear function of Y_i, thus $\beta=f(Y_i)/g(Y_i^2)$. Substituting $Y_i=s\overline{G}_i(s)$ yields another rational function of similar construction, with s in the denominator.

$$\overline{\delta}_{vis}=\beta\big|_{Y_i=s\overline{G_i}(s)}\overline{V^2}(s)=\frac{f(\overline{G_i}(s))}{s\cdot g(\overline{G_i}^2(s))}\overline{V^2}(s)=\frac{1}{s}\cdot\beta\big|_{Y_i=\overline{G_i}(s)}\overline{V^2}(s) \tag{35}$$

To convert to a form for use with creep functions instead of relaxation functions, the relation $s^2\overline{G}(s)\overline{J}(s)=1$ (realized from the Laplace transform of $J(t)*dG(t)=h(t)$) is used, instead substituting $Y_i=1/s\overline{J}_i(s)$ (36).

$$\overline{\delta}_{vis}=\beta\big|_{Y_i=1/s\overline{J}_i(s)}\overline{V^2}(s)=s\cdot\frac{f(1/\overline{J}_i(s))}{g(1/\overline{J}_i^{\,2}(s))}\overline{V^2}(s)=s\cdot\beta\big|_{Y_i=1/\overline{J}_i(s)}\overline{V^2}(s) \tag{36}$$

The viscoelastic solution in the Laplace domain is the product of two functions of the Laplace variable s, $\beta\big|_{Y_i=1/s\overline{J}_i(s)}$ and $\overline{V^2}(s)$. The inverse Laplace transform of such a product is the convolution integral of the inverse Laplace transforms of each function. As such, the viscoelastic solution for free displacement of the unimorph DEA can be expressed as the convolution integral of the inverse Laplace transform of $\beta\big|_{Y_i=1/\overline{J}_i(s)}$ and the time derivative of the input voltage (37).

$$\delta_{vis}=\mathcal{L}^{1}\left\{\overline{\delta}_{vis}\right\}=\mathcal{L}^{1}\left\{\beta\big|_{Y_i=1/\overline{J}_i(s)}\right\}*dV^2(t) \tag{37}$$

A similar procedure is used to determine the viscoelastic form of the elastic blocking force equation (38). Applying the Laplace transform to the elastic solution again acts only on the voltage input $V(t)$ whereas the coefficient parameters β/α are time invariant (39). The coefficient β/α, unlike the previous case, is a rational function where both the numerator and denominator are linear functions of Y_i. As a result, on substituting the Young's modulus Y_i by either the Laplace transformed relaxation function $s\overline{G}_i(s)$ or the reciprocal of the creep function $1/s\overline{J}_i(s)$, coefficient terms of s or $1/s$ do not occur (40) (41). Thus, on applying the inverse Laplace transform, no time derivative is applied to the input voltage in the convolution integral (42). A MATLAB script for evaluating the viscoelastic model is shown in Appendix D.

$$P_e=-\frac{\beta}{\alpha}V^2(t) \tag{38}$$

$$\overline{P}_e=\mathcal{L}\{P_e\}=-\frac{\beta}{\alpha}\overline{V^2}(s) \tag{39}$$

$$\overline{P}_{vis} = -\left.\frac{\beta}{\alpha}\right|_{Y_i = s\overline{G_i}(s)} \overline{V^2}(s) = \frac{p(\overline{G_i}(s))}{q(\overline{G_i}(s))}\overline{V^2}(s) = -\left.\frac{\beta}{\alpha}\right|_{Y_i = \overline{G_i}(s)} \overline{V^2}(s) \tag{40}$$

$$\overline{P}_{vis} = -\left.\frac{\beta}{\alpha}\right|_{Y_i = 1/s\overline{J_i}(s)} \overline{V^2}(s) = \frac{p(1/\overline{J_i}(s))}{q(1/\overline{J_i}(s))}\overline{V^2}(s) = -\left.\frac{\beta}{\alpha}\right|_{Y_i = 1/s\overline{J_i}(s)} \overline{V^2}(s) \tag{41}$$

$$P_{vis} = \mathcal{L}^1\left\{\overline{P}_{vis}\right\} = \mathcal{L}^1\left\{-\left.\frac{\beta}{\alpha}\right|_{Y_i = \overline{G_i}(s)}\right\} * V^2(t) \tag{42}$$

3.3.2 Viscoelastic material constitutive models

Two models were used for representing the creep and relaxation behavior of the DEA materials, the standard viscoelastic model (43) (44), and four parameter Prony series (45) (46). The Prony series lacks a closed-form representation for the creep function, however Loy [38] showed that interconversion between the relaxation function and creep function for the Prony series representation can be conveniently done via the relation $\overline{J}(s)\overline{G}(s) = 1/s^2$.

$$G(t) = E_1 + E_2 e^{-\frac{E_2}{\eta}t} \tag{43}$$

$$J(t) = \frac{1}{E_1}\left(1 - \frac{E_2}{E_1 + E_2} e^{-\frac{E_1 E_2}{\eta(E_1+E_2)}t}\right) \tag{44}$$

$$G(t) = G_0 - \sum_{i=1}^{n} G_i(1 - e^{-t/\tau_i}) \tag{45}$$

$$J(t) = \mathcal{L}^1\left\{\frac{1}{s^2\overline{G}(s)}\right\} \tag{46}$$

Relaxation data was acquired for all materials, held at 0.2% strain for 120 seconds, with the initial strain applied with a strain rate of 0.5%/s. Geometry of all specimens were similar, with 50 mm gauge length, 10 mm width, and thickness between 50 and 150 μm. For the standard viscoelastic model, stiffness parameter E_1 is fixed by the relaxation data at the end of test ($t = 120s$). The remaining stiffness parameter E_2 is fixed by relaxation data at $t = 0s$ since $G(0) = E_1 + E_2$. Damping term η was determined by linear least-square fitting using MATLAB's `cftool` function. The Prony series parameters $G_0 \cdots G_4$ and $\tau_1 \cdots \tau_4$ were determined using nonlinear least-squares fitting. Parameters for the standard viscoelastic model and Prony series

are tabulated in Table 6 and Table 7, respectively. A comparison of the relaxation data, and relaxation functions represented by the standard viscoelastic model, and Prony series, are shown in Figure 17. It follows from Figure 17 that the viscoelastic model based on the Prony series agrees with the experimental data, better than that based on the standard model.

Table 6. Standard viscoelastic model parameters for DEA materials

	E_1 [MPa]	E_2 [MPa]	η [MPa·s]
P(VDF-TrFE-CFE)	162.1	203.5	4080
MWCNT+Silicone [1:2]	1.39	3.55	92.5
Scotch tape	1366	496	8300

Table 7. Prony series parameters for DEA materials

	G_0	G_1	G_2	G_3	G_4	τ_1	τ_2	τ_3	τ_4
	[MPa]					[s]			
P(VDF-TrFE-CFE)	395.6	123.0	87.35	36.43	0	1.590	53.42	3.441	1
MWCNT+Silicone [1:2]	4.885	1.746	0.7235	0.6757	0.6159	67.05	0.1245	1.715	12.55
Scotch tape	1663.2	350.4	241.6	153.1	51.26	1170	0.5503	25.98	1.672

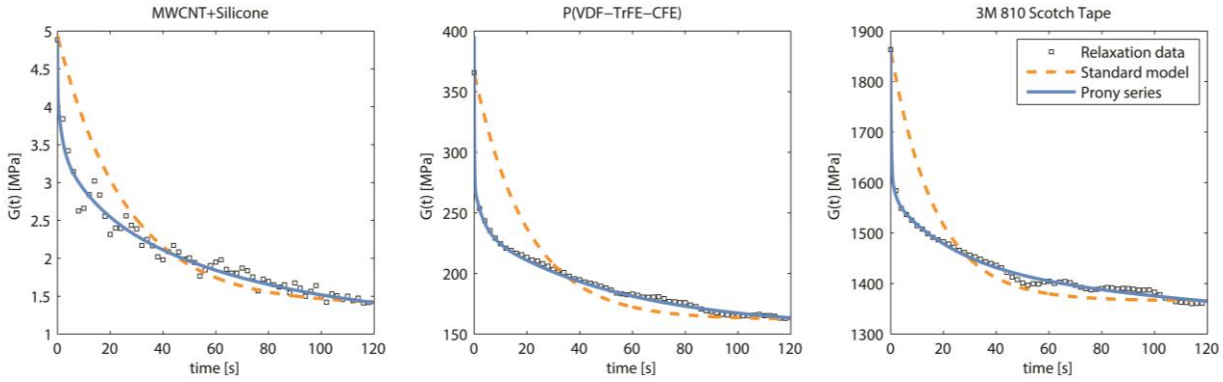

Figure 17. Relaxation data and viscoelastic material models for DEA materials.

3.3.3 Comparison with experimental results

The model predictions of tip displacement (37) and blocking force (42) were validated by comparison with experimental results from actuation of the P(VDF-TrFE-CFE) unimorph DEA fabricated in Chapter 3.2. The Prony series and the associated parameters in Table 7 were used to model the viscoelastic behavior of the DEA materials. The average thickness of the electrode and

DE layers in each DEA was measured under an optical microscope, tabulated in Table 2. Images of the DEA cross sections are shown in Appendix A. In all figures and tables, 2L, 4L … 10L denote the number of DE layers. Additional geometric and material parameters used for the viscoelastic model are shown in Table 8. It should be noted that in contrast with the elastic model of the VHB DEA, here the electrodes cannot be ignored, as they have non-negligible thickness.

Table 8. Additional model parameters for viscoelastic model.

Parameter	Value
Length	10 mm
Width	10 mm
Elastic layer thickness	50 μm
Elastic layer Poisson's ratio	0.35
DE/Electrode Poisson's ratio	0.50
DE relative permittivity	50

Figure 18 shows the experimental setup for the measurement of tip displacement and blocking force of the DEA. Tip displacement was measured by a laser displacement sensor (Keyence LK-081) and the blocking force at the tip of the actuator was measured by a 10 g capacity load cell (Transducer Techniques). The displacement and force of the DEA was measured as a step voltage of 500V was applied to the DEA. Data was recorded for 120 seconds.

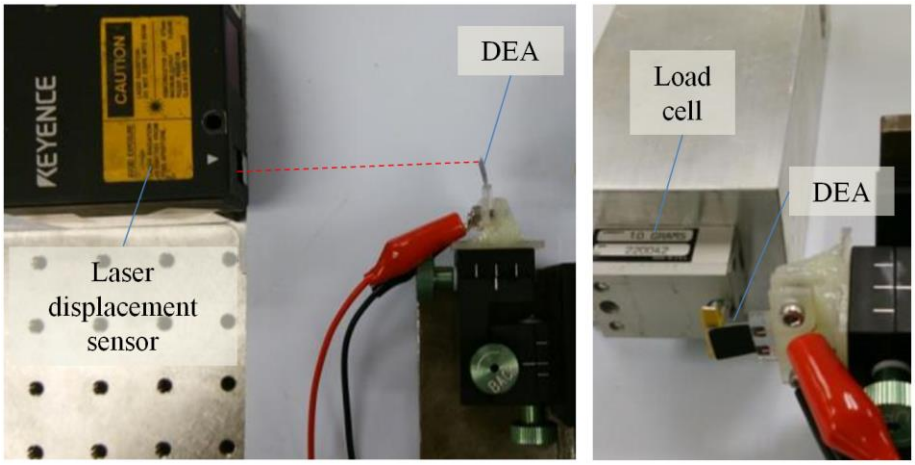

Figure 18. Experimental setup for measurement of tip displacement and blocking force.

Plots of the measured and predicted tip displacement and blocking force are shown in Figure 19 and Figure 20, respectively. In these plots it can be qualitatively observed that the evolution of displacement and force with time is reasonably well predicted by the viscoelastic model,

particularly for the DEA with four or more DE layers. Figure 21 illustrates the evolution of the tip displacement and blocking force with respect to the number of DE layers, and time. Figure 22 illustrates the error between the model prediction and the experimental results. The viscoelastic model predicts the tip displacement and blocking force to within 15% of the measured value at 120 seconds. However, the error between the predicted and measured results is greatest when the actuator is first energized. Additionally, there is a significant amount of error for the 2-DE-Layer DEA.

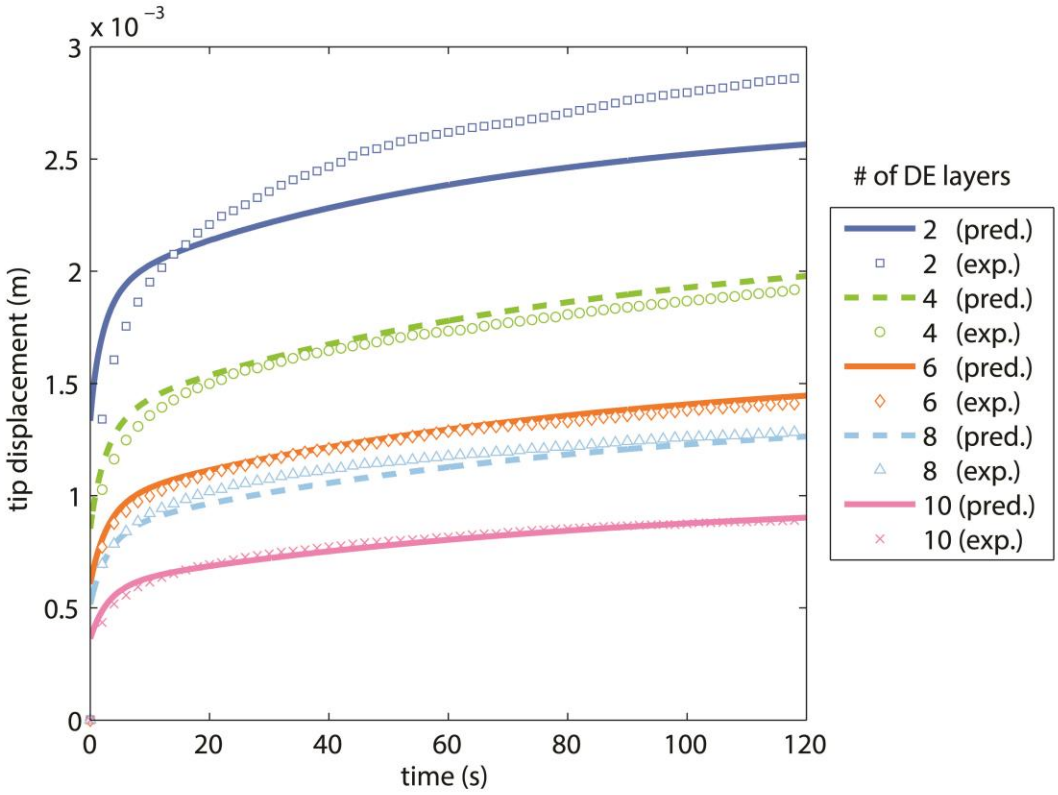

Figure 19. Predicted and measured tip displacement of DEA.

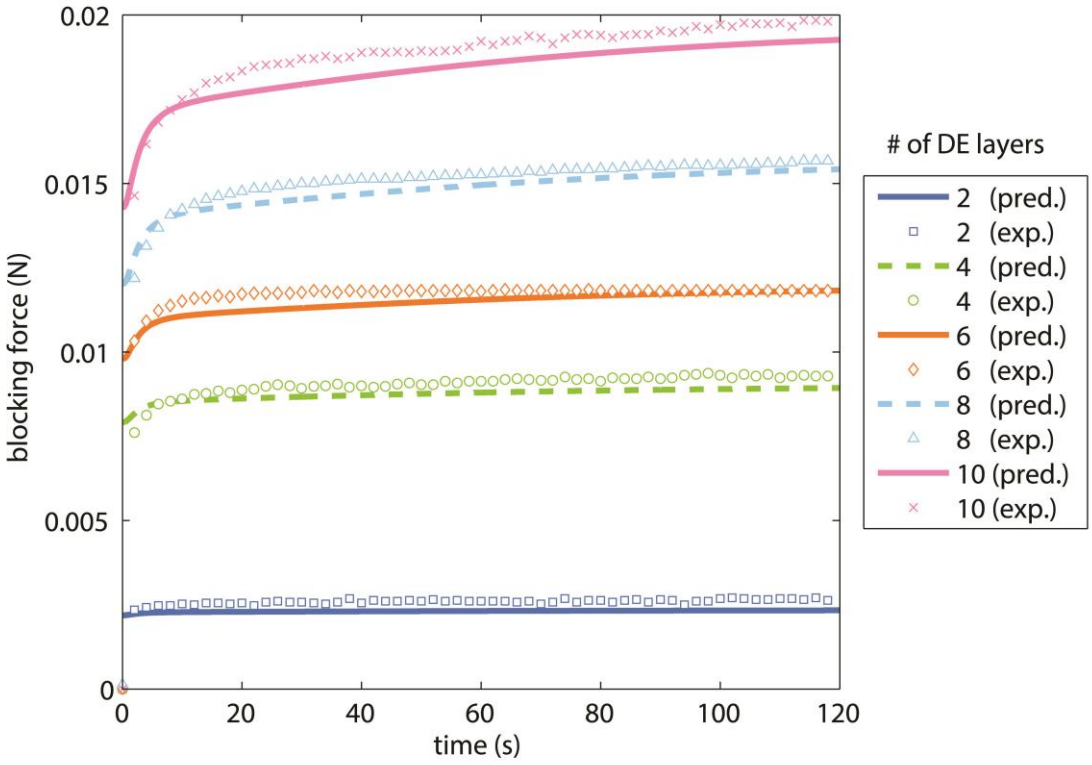

Figure 20. Predicted and measured blocking force of DEA.

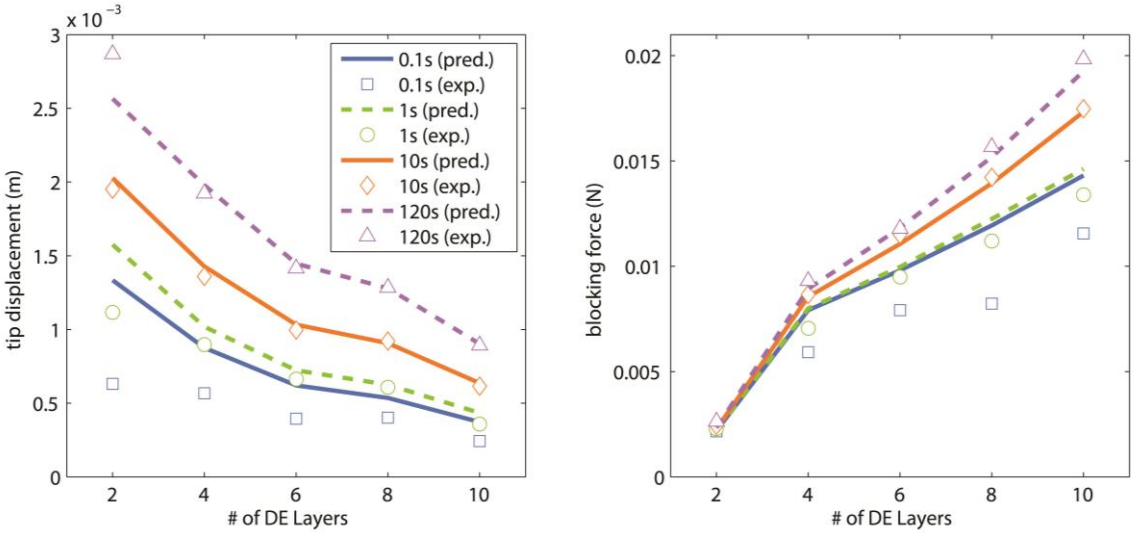

Figure 21. Evolution of tip displacement (left) and blocking force (right) with respect to time and number of DE layers.

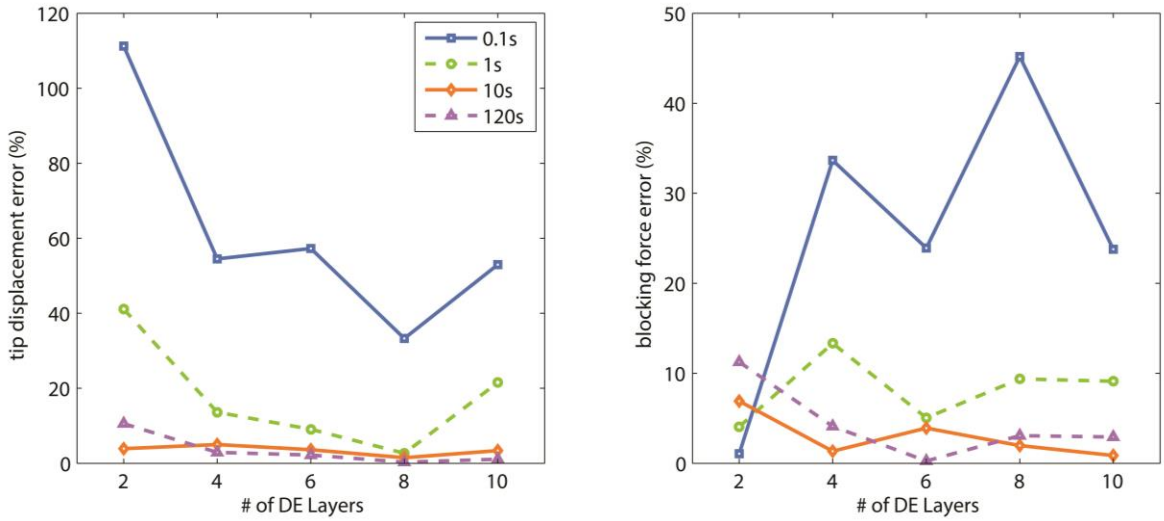

Figure 22. Error in model prediction for tip displacement (left) and blocking force (right) with respect to time and number of DE layers.

3.3.4 Comparison with experimental results from DEA population

It was shown in Chapter 3.3.3 that the viscoelastic model's predictions matched reasonably well with experimental data from single samples of multilayer unimorph DEA. However, some variance can be expected in the behavior of DEA, owing to slight variations in the fabrication and testing process. To this end, additional performance data from DEA fabricated using the present method is required to establish the expected variance between DEA samples fabricated in a batch. Moreover, the population data can be used to determine whether or not the viscoelastic model predictions fall within the bounds of the measured variance.

DEA consisting of 2, 4, 6, 8, and 10 DE layers were fabricated, using the process described in Chapter 3.1.2. The parameters for each batch of DEA are shown in Table 9. It is noted that although the deposition parameters for the DEA within each batch remain constant, they vary between batches to account for changes in temperature and solution viscosity at the time of fabrication. Tip displacement and blocking force for all DEA was measured with the same setup as described in Chapter 3.3.3.

Table 9. DEA batch deposition parameters.

	# of DE Layers				
	2L	**4L**	**6L**	**8L**	**10L**
P_1 (electrode) [kPa]	5.5	5.5	5.5	5.5	5.5
P_2 (DE pass 1) [kPa]	30, 50~58	30, 50~52	30, 50~56	30, 50~60	30, 50~62
P_3 (DE pass 2) [kPa]	40, 60	40, 60~62	40, 60~66	40, 60~66	40, 60~68
Success rate	8/12 (66.7%)	8/8 (100%)	5/8 (62.5%)	5/8 (62.5%)	3/8 (37.5%)
Samples tested	8	5	5	5	3

Figure 23 and Figure 24 show the tip displacement and blocking force of the DEA fabricated in each batch. Also shown on each plot are the corresponding model predictions using the DEA layer thicknesses shown in Table 10, additional parameters in Table 8 and Prony series parameters of Table 7. Table 11 and

Table 12 tabulate the mean and standard deviation of the DEA performance at various stages of deposition.

Table 10. Average thickness of DEA batches.

	# of DE layers				
	2L	**4L**	**6L**	**8L**	**10L**
Electrode thickness [µm]	7	10	10.5	10.5	11
DE thickness [µm]	18	18	18	18	18

Table 11. Tip displacement mean and standard deviation.

# of DE Layers	**Tip Displacement (mm) +/- 1 S.D. [% of mean]**			
	t = 0.1 s	**t = 1 s**	**t = 10 s**	**t = 120 s**
2	1.45 ± 0.25 (17.2%)	1.90 ± 0.26 (13.9%)	2.62 ± 0.27 (10.4%)	3.21 ± 0.26 (8.1%)
4	0.56 ± 0.07 (12.4%)	0.87 ± 0.10 (11.0%)	1.38 ± 0.15 (11.0%)	2.03 ± 0.16 (8.0%)
6	0.35 ± 0.08 (23.4%)	0.65 ± 0.06 (9.5%)	1.01 ± 0.07 (7.1%)	1.39 ± 0.10 (7.2%)
8	0.39 ± 0.07 (17.7%)	0.60 ± 0.06 (10.2%)	0.92 ± 0.09 (9.5%)	1.26 ± 0.12 (9.7%)
10	0.25 ± 0.03 (11.6%)	0.38 ± 0.03 (8.6%)	0.64 ± 0.07 (10.3%)	0.90 ± 0.06 (6.2%)

Table 12. Blocking force mean and standard deviation.

# of DE Layers	Blocking Force (mm) +/- 1 S.D. [% of mean]			
	t = 0.1 s	**t = 1 s**	**t = 10 s**	**t = 120 s**
2	1.97 ± 0.59 (30.2%)	2.45 ± 0.41 (16.6%)	2.58 ± 0.42 (16.4%)	2.67 ± 0.38 (14.1%)
4	3.37 ± 0.62 (18.4%)	4.29 ± 0.40 (9.3%)	5.26 ± 0.52 (9.9%)	5.60 ± 0.69 (12.4%)
6	6.78 ± 1.78 (26.3%)	9.22 ± 1.19 (12.9%)	11.28 ± 1.22 (10.9%)	11.62 ± 1.47 (12.7%)
8	9.01 ± 2.41 (26.8%)	11.00 ± 1.22 (11.1%)	13.86 ± 1.27 (9.2%)	15.29 ± 1.22 (8.0%)
10	11.03 ± 2.38 (21.6%)	13.23 ± 0.95 (7.1%)	17.60 ± 1.48 (8.4%)	20.03 ± 1.38 (6.9%)

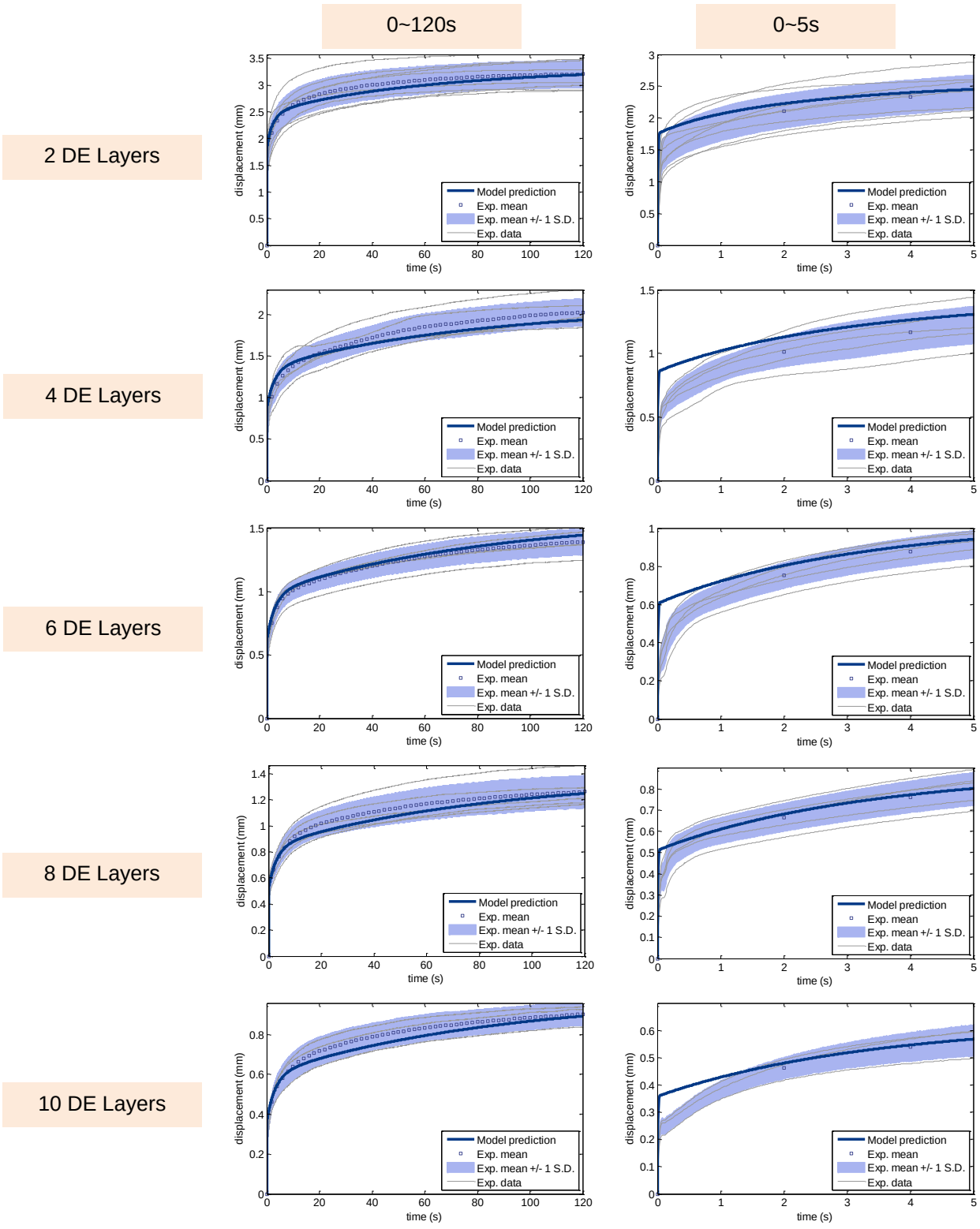

Figure 23. Tip displacement from experimental data of DEA population, with model prediction.

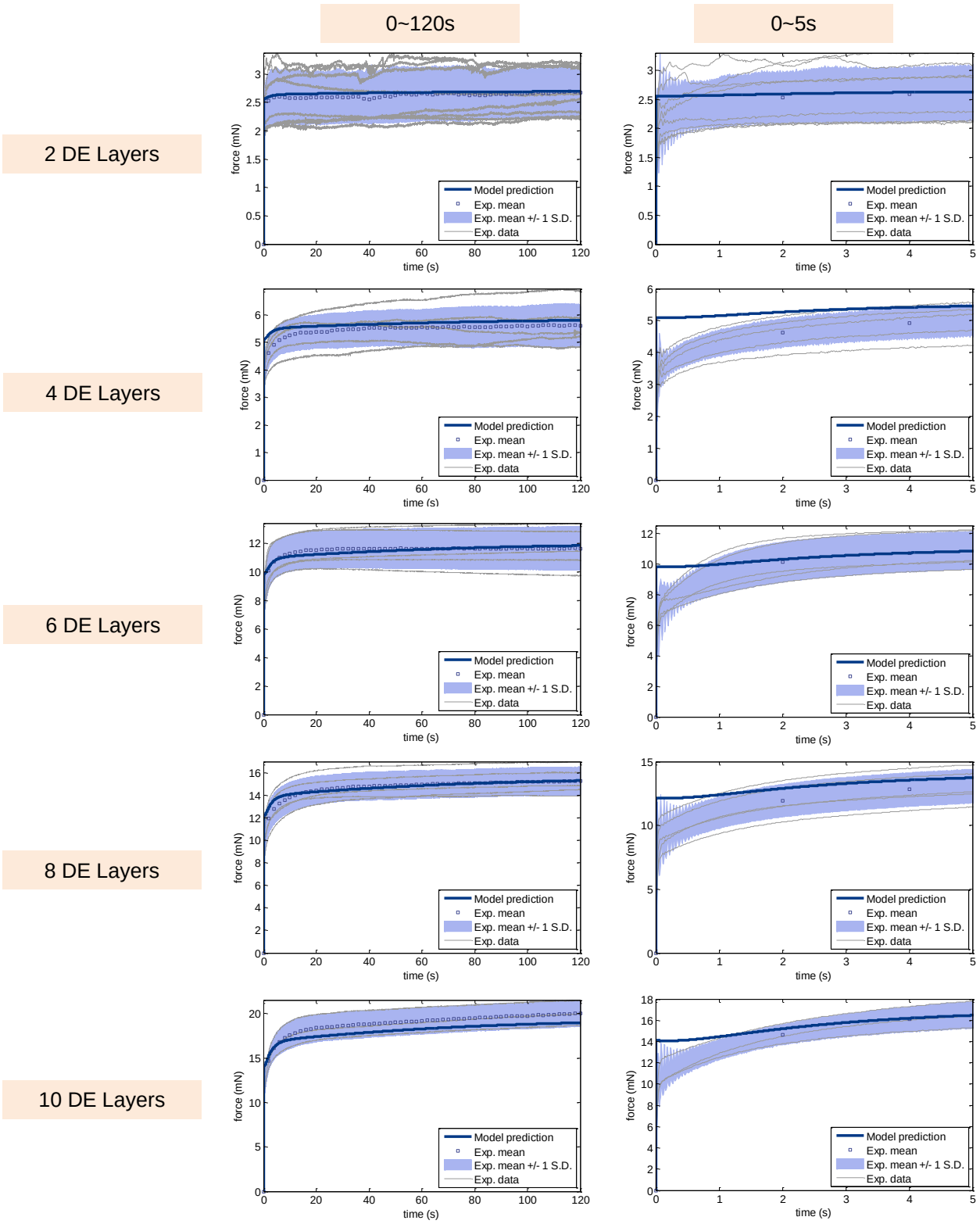

Figure 24. Blocking force from experimental data of DEA population, with model prediction.

Similar to the comparison with the experimental results of the limited dataset in Chapter 3.3.3, the viscoelastic model predictions agree reasonably well with the DEA population data. In all cases, the model predictions remain within 1 standard deviation of the experimental mean throughout most of the actuation, except for the region between $t = 0$ and $t = 2$ seconds, wherein all cases the model overpredicts the tip displacement and blocking force by as much as 79% and 51%, respectively. At later stages of deformation, at $t = 10\,\text{s}$ and $t = 120\,\text{s}$, the error remains well below 10%. The deviation of the model from the experimental mean is tabulated in Table 13 and Table 14.

Table 13. Error of model compared against population mean, for tip displacement

# of DE Layers	Tip Displacement			
	t = 0.1 s	t = 1 s	t = 10 s	t = 120 s
2	24.23%	8.42%	-1.32%	-0.27%
4	55.25%	16.92%	3.05%	-4.55%
6	78.59%	11.34%	2.24%	3.84%
8	34.25%	1.22%	-3.77%	-1.05%
10	48.13%	12.21%	-1.89%	-0.87%

Table 14. Error of model compared against population mean, for blocking force

# of DE Layers	Blocking Force			
	t = 0.1 s	t = 1 s	t = 10 s	t = 120 s
2	30.21%	4.91%	2.62%	0.85%
4	51.04%	20.02%	5.26%	3.49%
6	44.65%	8.19%	-1.94%	1.72%
8	34.88%	12.68%	1.78%	0.26%
10	27.64%	9.25%	-3.10%	-5.33%

The population data in Table 13 and Table 14 establishes that the standard deviation of the tip displacement and blocking force is highest at earlier stages of deformation (16.5% and 24.7% of the mean respectively, at $t = 0.1\,\text{s}$ averaged across all samples), and decreases at later stages of deformation (7.8% and 10.8% respectively, at $t = 120\,\text{s}$).

3.3.5 Refinement of viscoelastic model

The most significant limitation of the viscoelastic model discussed in this work is the disparity between the model predictions and collected data during the early stages of deformation, particularly in the region between 0.1 and 1 second. This disparity is due to the rather simplistic

nature of the model; particularly in the assumption that the DEA remains flat in the width-wise direction throughout the entire deformation. In reality, DEA typically have some non-negligible initial curvature along the length and width due to residual stresses formed as the liquid DEA materials cure during deposition. Although much of the curvature is often removed by annealing during post-processing, the fact that the DEA is a free standing, thin, soft film means that it will often have some degree of initial curvature.

The curvature of a DEA in the length and width directions was measured throughout its deformation over 30 seconds under an applied voltage of 500V. The DEA used consisted of 2 DE layers, and the out-of-plane displacements were measured at two points along the actuator's length and six points along its width, as shown in Figure 25. Position measurements were taken using a laser displacement sensor (LDS) (Keyence LK-081), mounted on a 2-axis stage. Curvature was estimated from position measurements using least squares curve fitting using MATLAB's *lsqcurvefit()* function with the custom equation $f(y) = -\sqrt{(1/\kappa)^2 - (y-5)^2} + z_0$. The evolution of the widthwise cross-section shape at various time steps as measured by the laser displacement sensor is shown in Figure 26, and the evolution of the widthwise tip curvature determined by curve fitting is shown in Figure 27.

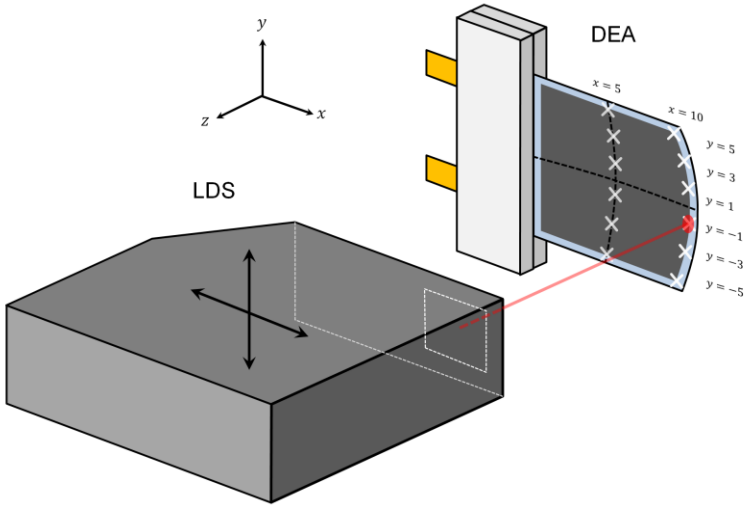

Figure 25. Profile measurement of DEA during actuation, showing measurement locations.

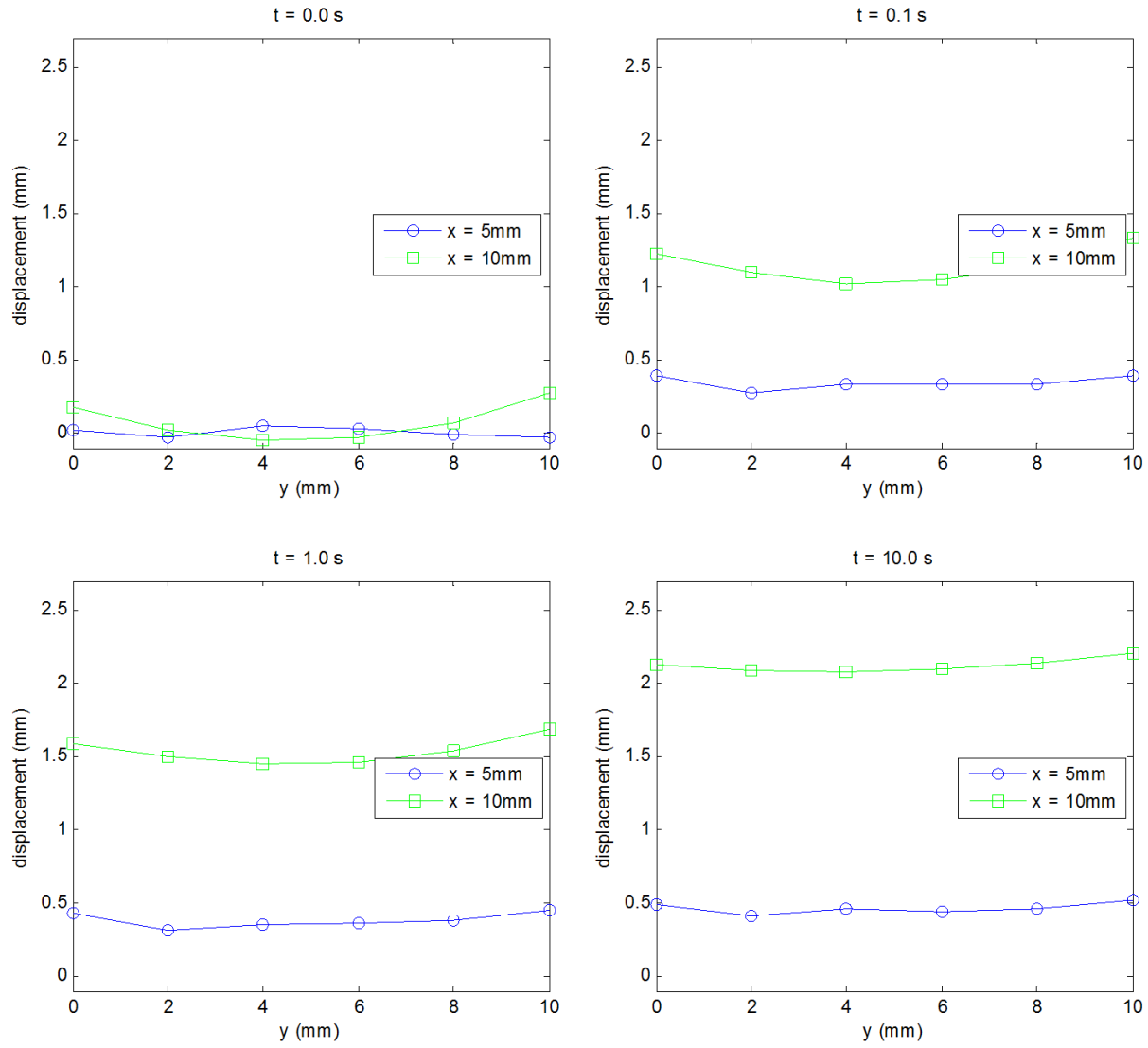

Figure 26. Evolution of widthwise cross-section shape of 2 DE layer DEA.

From Figure 27, it is observed that the initial widthwise curvature disappears during deformation, as the lengthwise curvature begins to dominate. Additionally, the majority of the curvature change occurs during the first two seconds of deformation. This implies that the overestimation of displacement by the viscoelastic model could be attributed to the fact that some fraction of strain energy is being spent "straightening out" the initial widthwise curvature of the DEA early in the deformation.

Since the viscoelastic model is basically one-dimensional, it is not expedient to calculate the widthwise curvature change. Instead, the data acquired in Figure 27 can be used in a strain energy method to compensate accordingly.

The model assumes that all strain energy is the result of bending along the length direction, while in reality biaxial bending occurs and strain energy occurs due to length and widthwise curvatures. Assuming conservation of energy between the model and experimental cases, the strain energy is equated as shown in (47). The left hand side consists of the bending strain energy in the width direction U_w and length direction U_l and the right hand side is the strain energy due to lengthwise curvature predicted by the model U_{mdl}. The quantity U_l will be useful to calculate the adjusted tip displacement and (47) is rearranged accordingly as (48).

$$U_w + U_l = U_{mdl} \tag{47}$$

$$U_l = U_{mdl} - U_w \tag{48}$$

Strain energy of a Euler-Bernoulli beam takes the form of the well-known equation expressed in (49), which is a function of the internal moment M, and bending stiffness EI. When small displacements are assumed, the moment is directly proportional to the curvature κ through (50).

$$U_{bend} = \int \frac{M^2}{2EI} dx \tag{49}$$

$$M = EI\kappa \tag{50}$$

Along the length of the DEA, the curvatures κ_l and κ_{mdl} remain constant (see Chapter 3.2.1, the radius of curvature ρ is constant with respect to the lengthwise coordinate x) and thus evaluation of the strain energy in the lengthwise directions in (51) and (52) is trivial. On the other hand, the widthwise curvature κ_w does not remain constant; it is maximized at the tip ($x = L$), with value $\kappa_{w_{tip}}$ and constrained to zero at the base ($x = 0$). Thus the widthwise curvature is assumed linearly proportional to x (54). Substituting and evaluating the integrals in (51) - (53) into (48) yields (55), which is an adjusted expression for the lengthwise curvature based on the model prediction, and the measured width curvature.

$$U_l = \int_0^L \frac{EI\kappa_l^2}{2} dx \tag{51}$$

$$U_{mdl} = \int_0^L \frac{EI\kappa_{mdl}^2}{2} dx \tag{52}$$

$$U_w = \int_0^L \frac{EI\kappa_w(x)^2}{2} dx \tag{53}$$

$$\kappa_w(x) = \kappa_{w_{tip}} \frac{x}{L} \tag{54}$$

$$\kappa_l = \left(\kappa_{mdl}^2 - \frac{1}{3}\kappa_{w_{tip}}^2 \right)^{1/2} \tag{55}$$

Figure 27 and Figure 28 show the result of Equation (55) in terms of curvature and tip displacement, respectively.

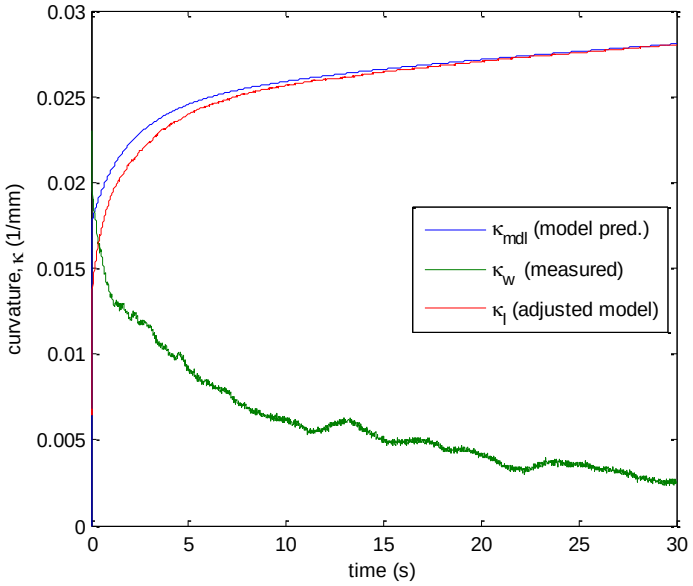

Figure 27. DEA curvature over time, measured over width and lengthwise directions.

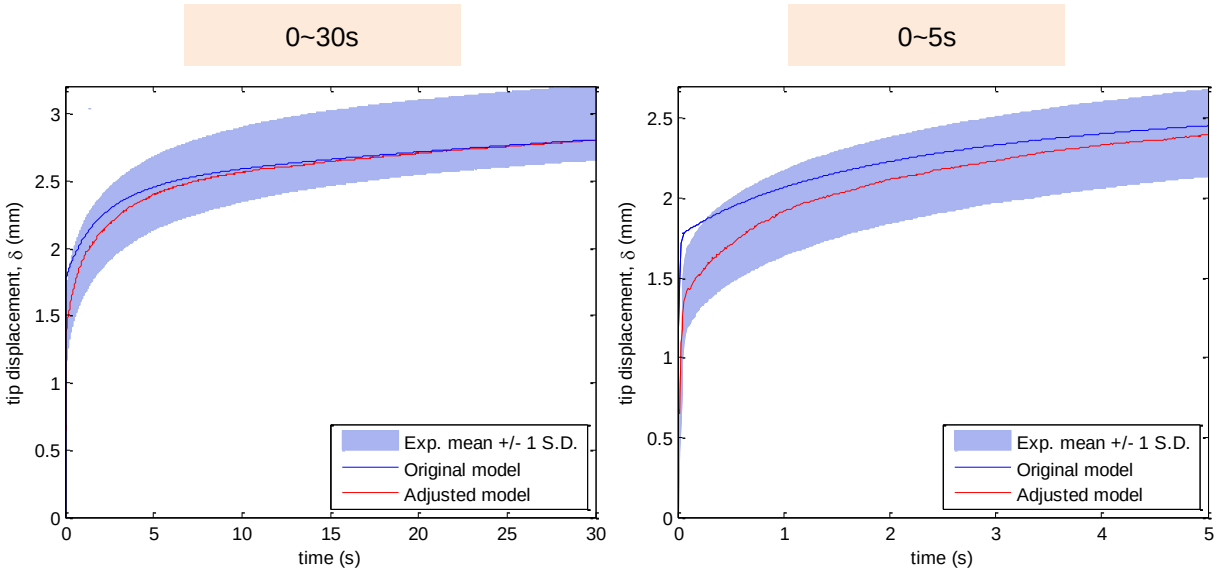

Figure 28. DEA tip displacement, with original and adjusted models compared against 2 DE layer experimental data.

In Figure 28, it is observed that the curvature-adjusted viscoelastic model matches the experimental data more closely, especially at the beginning of deformation, and remains within 1 standard deviation of the mean during the entire 30 second duration of testing. The adjusted model approaches the original model as deformation continues past 30 seconds, since the curvature returns to the flat shape assumed by the original model. This indicates that the differences observed between the original model and experimental results (Figure 22) can be explained by a mechanical means – namely that some fraction of the strain energy produced via compression under electrostatic forces is used to transition between an initial state where the DEA is curved mostly in the width direction, to the deformed state where it is curved in the length direction.

The implications of this finding are as follows. Since the disparity is attributed to a mechanical means, it indicates that the use of the Maxwell strain equation (1) is sufficient to model the electromechanical coupling of dielectric elastomers, and additional coupling is not required. For instance, the coupling between electric field and stiffness suggested by Lu [13] and strain dependent electric properties reported by Ask [39] (particularly for strains exceeding 100%, and in the case of pre-stretched materials) are not necessary to predict its time-dependent behavior. From a practical standpoint, improved response of the actuators at short time intervals after actuation could be improved by reducing the initial curvature of the DEA. This could be done by

reducing residual stresses, either in the deposition process by reducing the solvent content of the solutions, or by additional annealing processes in post-processing to reduce the widthwise curvature. Alternatively, stiffening fibers could be added to the DEA in the width direction to introduce stiffness anisotropy and set a preferential direction of curvature.

3.4 Conclusions

High driving voltage and low blocking force are key limitations of DEA fabricated from conventional materials such as silicone and acrylic elastomers using techniques such as solution casting, spray coating, and construction from thick films. Performance of existing DEA and those fabricated in this work in terms of geometry-normalized blocking force and tip displacement per kilovolt are plotted in Figure 29. The use of relatively stiff, high dielectric constant PVDF terpolymer, in conjunction with the robotic dispenser to produce thin dielectric layers allows for force figure of merit one to two orders of magnitude higher than existing work, without sacrificing displacement performance. Moreover, the use of the robotic actuator allows flexible production of DEA; a toolpath is simply changed and retooling is not required as is the case for spray deposition or screen printing.

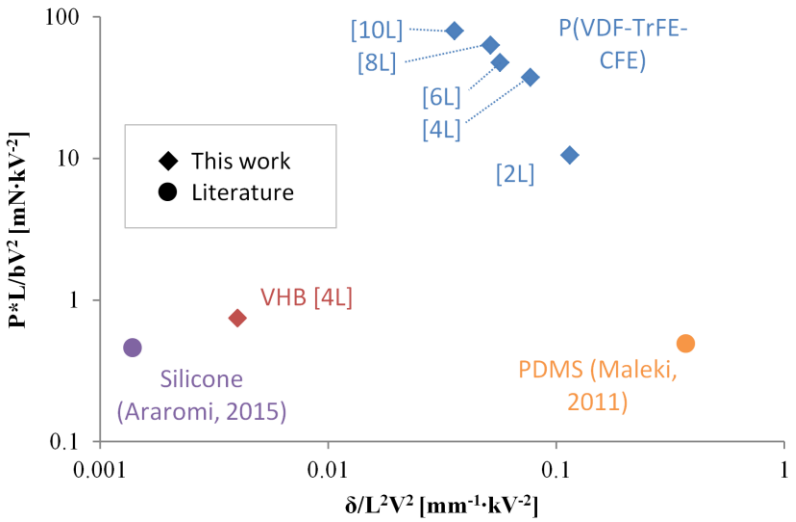

Figure 29. Figure of merit for blocking force and tip displacement for unimorph DEA tested in this work and others.

The elastic and viscoelastic models presented in this work represent the first analytical, closed form solutions for unimorph DEA displacement and blocking force. Additionally, both models are validated, agreeing well in comparisons against experimental data.

4. Variable stiffness dielectric elastomer actuators

4.1 Introduction

This chapter discusses the use of electrolaminates and electroadhesion to produce variable stiffness DEA (VSDEA). The need for DEA to feature variable stiffness properties is alluded to in Chapter 2.1 – the intrinsic softness of dielectric elastomer materials can yield large displacements, but lack large generative forces and stiffness required to manipulate heavy objects without unwanted deformation. This tends to be especially true in the case of multilayer unimorph DEA: it is apparent from the models produced in Chapters 3.2 and 3.3 that there is a clear tradeoff between generating large deformations and large forces – they cannot simultaneously produce both. For instance, an actuator with relatively few thin layers will produce large deformations but its ability to resist any external load will be limited, conversely an actuator with thicker or a greater number of layers will be stiffer, but produce proportionally lower deformation. This confounding relationship is illustrated in Figure 30. VSDEA in concept are an attractive means of achieving large deformation and large holding force in a single actuator, by modulating the stiffness of the actuators to suit the situation.

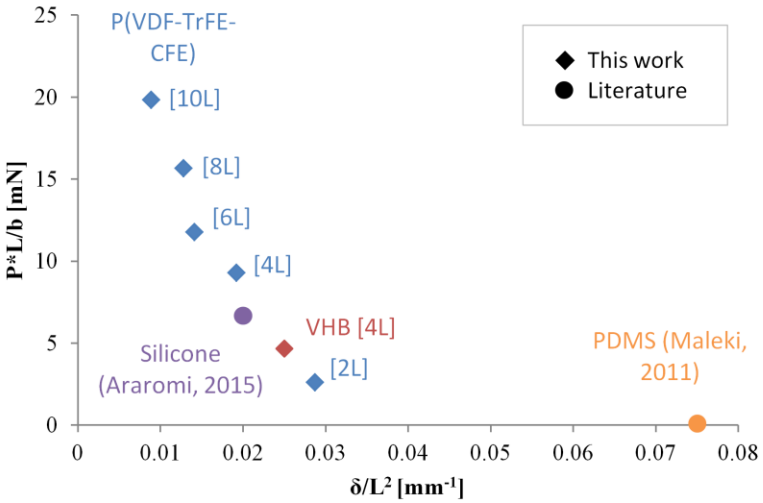

Figure 30. Relationship of figures of merit for blocking force and tip displacement among various unimorph DEA.

One actuator design has been proposed to improve the load-carrying ability of DEA, namely VSDEA based on low melting point alloy (LMPA) [22]. The main benefit of the LMPA device is its 90× stiffness change due to phase change of the LMPA, and the ability for a gripper made

from the device to lift 5.5 times its own weight. However, the energy needed produce the phase change by joule heating (~0.5 W over 30 s) dwarfs the energy used to power the DEA itself (typically tens of mW over less than 0.1 s), not to mention the slow transition time and possibility of leakage of the toxic LMPA.

This chapter will investigate the use of electrolaminates as an alternative type of VSDEA material featuring low power consumption, light weight, and high speed transition between high and low stiffness states. Electrolaminates are a composite structure comprised of alternating dielectric or insulating layers and conductive electrode layers, as shown in Figure 31. The alternating layers are connected electrically so that when a voltage is applied, opposite charges form in each layer, resulting in electrostatic clamping to control the amount of shear stress that can be supported by each interface. When no voltage is applied, the layers (which have no adhesive bonding between them) are free to slide and buckle, such that the laminate has low bending stiffness. When a voltage is applied, the layers are firmly clamped together by electrostatic force, so the laminate as a whole becomes stiffer. Two types of VSDEA are discussed in this chapter: unimorph DEA with electrolaminate variable bending stiffness passive layer, and VSDEA based on parallel units with electrostatic chucking.

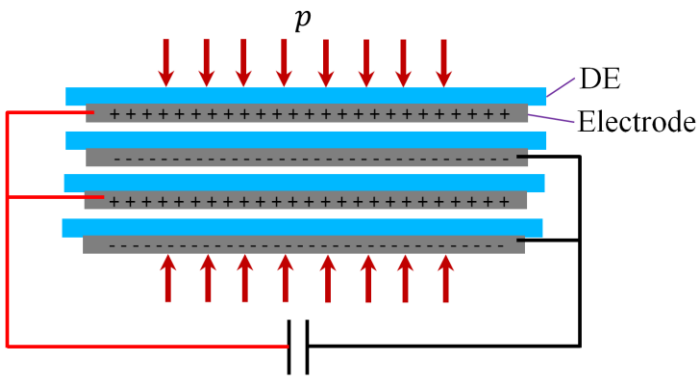

Figure 31. Diagram of electrolaminate operation.

4.2 Electrolaminate as variable bending stiffness passive layer

4.2.1 Working principle

A simple way to make a VSDEA is to attach the variable stiffness device directly to the actuator. In the case of the unimorph DEA, the passive layer is a prime location for the variable stiffness

device (Shintake [22] similarly applies the variable stiffness device to the passive layer), since its sole purpose is to resist transverse expansion of the active material and induce bending. It follows then that a VSDEA can be produced by replacing the passive layer by an electrolaminate as a variable bending stiffness passive layer. The overall structure and operating principle of the electrolaminate passive VSDEA (EP-VSDEA) is shown in Figure 32. The electrolaminate consisting of a plurality of layers is attached to the passive layer surface of a typical unimorph DEA. The EP-VSDEA has two independent voltage sources, one for the actuation voltage applied to the DEA laminate, and one for the clamping voltage applied to the electrolaminate. When the clamping voltage is applied to the electrolaminate, its layers are attracted to one another, as well as the top surface of the passive layer, resulting in larger bending stiffness of the EP-VSDEA.

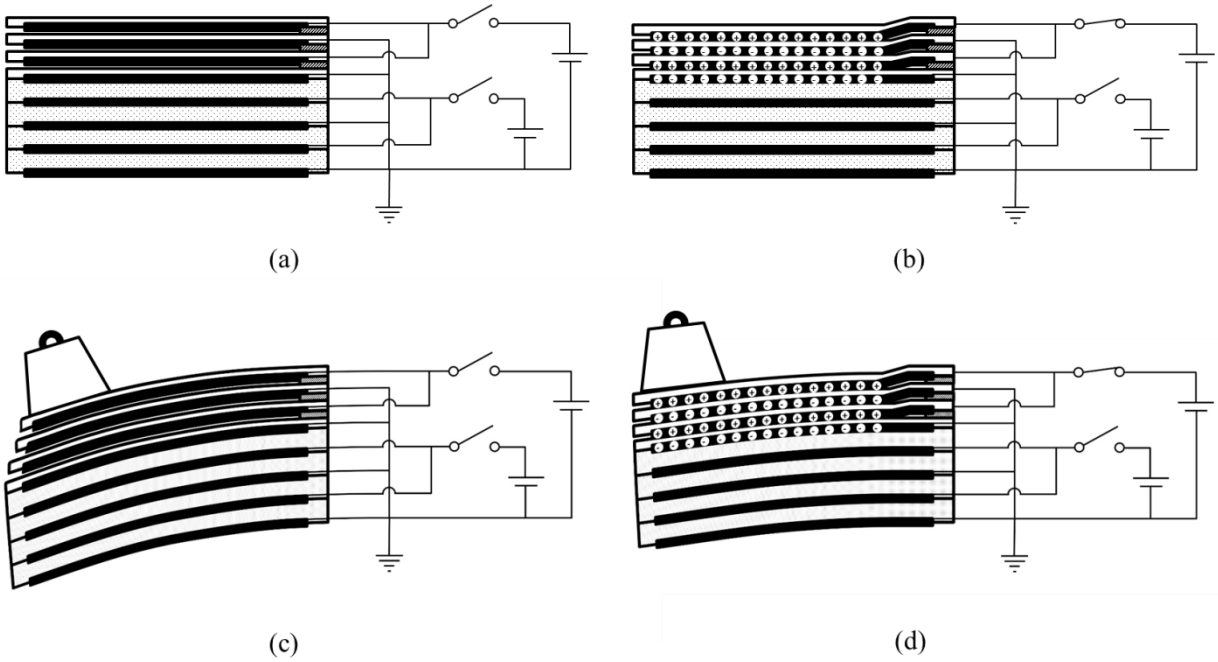

Figure 32. Construction of VSDEA in (a) unloaded, unclamped, (b) unloaded, clamped, (c) loaded unclamped, (d) loaded, clamped states.

4.2.2 Fabrication

The electrolaminate dielectric was cellophane film, 40 μm thick. Cellophane was used because it is electrically insulative, relatively stiff, and available as a flat film. Rectangular electrodes (1:1 by weight ratio of silicone emulsion polymer KM2002L-1 and 4 wt% aqueous solution of MWCNT) measuring 40 mm × 15 mm were applied to one side of each piece of cellophane dielectric by roll coating and a Parafilm mask. Alternating layers were connected electrically by

self-adhesive copper tape. Electrolaminates consisting of one, three, and five layers were constructed, and attached to unimorph actuators constructed from four layers of VHB F9469PC (see Chapter 3.1.1). The electrolaminate and unimorph DEA were secured at one end to a glass slide by polyimide tape. The ground plane of the electrolaminate is connected to the ground plane of the DEA. A completed example is shown in Figure 33.

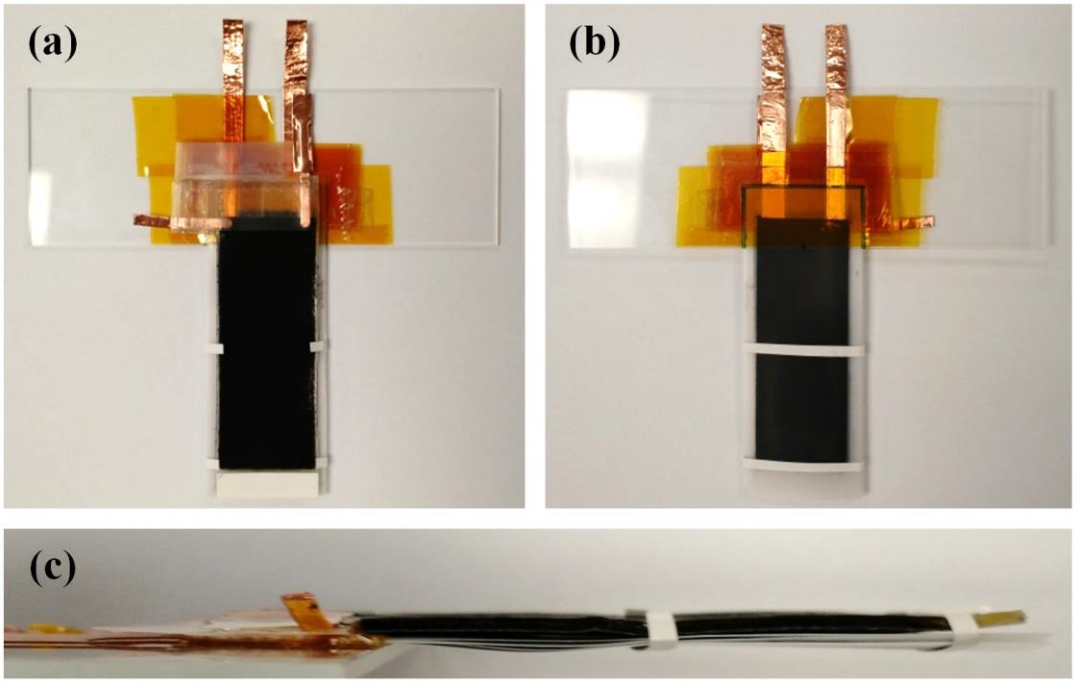

Figure 33. Completed VSDEA, shown from (a) DEA side, (b) Electrolaminate side, (c) side view

4.2.3 Experimental results

The bending stiffness of the 1, 3, and 5-layer electrolaminate VSDEA under various clamping voltages were measured by applying incremental displacement to the tip of the VSDEA, and measuring the reaction force using a 10-gram load cell. The experimental setup is shown in Figure 34, and the result is shown in Figure 35. The bending stiffness (normalized to the unclamped bending stiffness of the VSDEA) remains undergoes little change from 0-150V, but increases rapidly from 150-200V, saturating above 250V. The maximum increase in bending stiffness generally increases as a function of the number of electrolaminate layers, but appears to follow a saturating trend after more than three layers. A maximum stiffness increase of 3.7-fold was observed in the VSDEA with 5 electrolaminate layers, at a clamping voltage of 300V. The speed of the stiffness increase was fast, occurring in <1s. The first natural frequency and

damping ratio of the 5-layer VSDEA are tabulated in Table 15, showing the expected increase in natural frequency with increased stiffness, but no obvious trend in damping ratio.

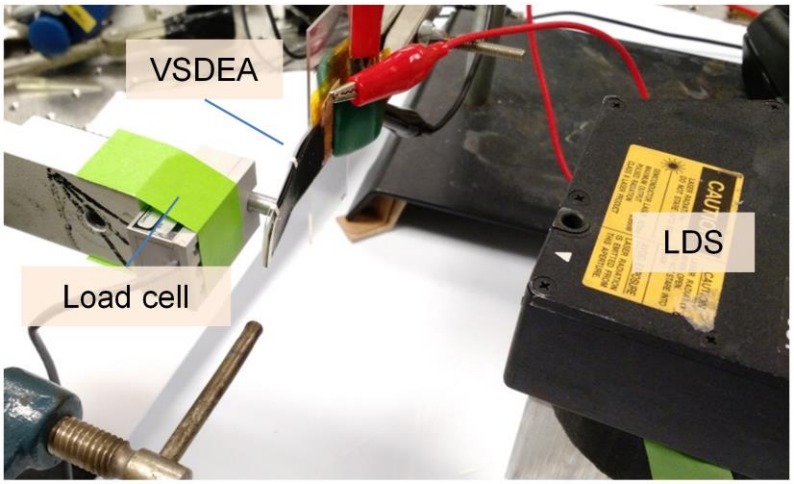

Figure 34. Stiffness measurement experimental setup.

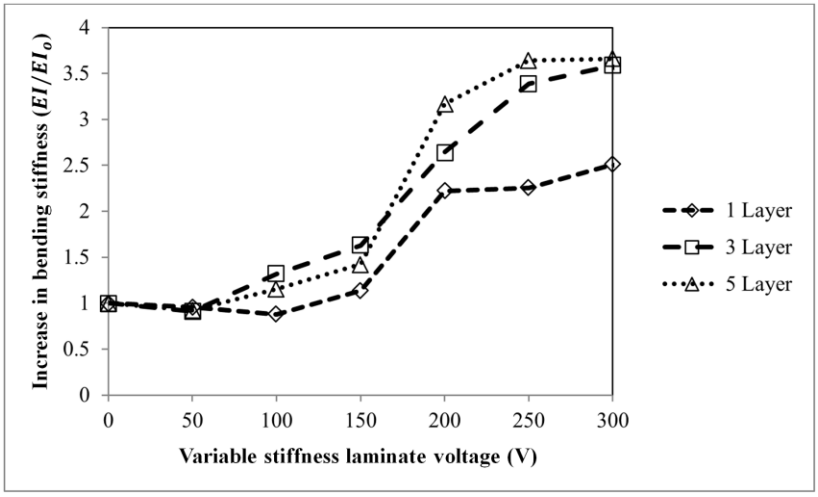

Figure 35. Increase in bending stiffness of VSDEA.

Table 15. Change in first natural frequency and damping ratio of 5-layer electrolaminate VSDEA.

V_{EL}	ω_n [Hz]	ζ
0	8.04	0.267
150	13.33	0.331
300	17.14	0.243

4.2.4 Discussion

A VSDEA using a variable-stiffness electrolaminate has been demonstrated exhibiting nearly four-fold increase in bending stiffness in less than one second. This structure can change its static and dynamic properties to suit its working environment. Some limitations are yet to be overcome, including the small stiffness change relative to phase-change devices such as LMPA.

4.3 Variable stiffness DEA based on parallel units with electrostatic chucking

4.3.1 Working principle

The EP-VSDEA demonstrated in Chapter 4.2 works reasonably well to demonstrate that electrolaminates can be employed to the desired effect in VSDEA. However, the use of electrolaminate as a passive layer does not entirely achieve the goal of increasing blocking force without appreciably decreasing the displacement (or vice versa). Increasing the number of layers in the electrolaminate serves to enhance the increase in bending stiffness, but has a deleterious effect on the displacement. Additional electrolaminate layers incur additional bending stiffness, even when the electrostatic chucking is turned off – when a chucking voltage is not applied, the electrolaminate becomes dead weight. In sum, the EP-VSDEA (in fact, likely any VSDEA incorporating a variable-stiffness element into its passive layer – including the LMPA VSDEA) still features an element of the troubling inverse relationship between displacement and blocking force.

An alternative can be found by assembling a plurality of unimorph DEA units in parallel, such that the DEA units themselves comprise an electrolaminate – this structure is henceforth referred to as the P-VSDEA (parallel VSDEA). In simplest terms, the VSDEA consists of multiple unimorph actuators with similar construction to those described in Chapter 3.1.2, but with an additional electrode to facilitate electrostatic chucking.

The unimorph DEA units consist of a passive layer, two DE layers, an insulator layer, and four electrode layers sandwiching the DE and insulator layers. These layers are configured in the order shown in Figure 36. There are three electrical terminals for each DEA unit: two electrode layers: two electrode layers are connected to a ground terminal, one is connected to a positive terminal for bending actuator, and another electrode layer is connected to a separate positive terminal for chucking.

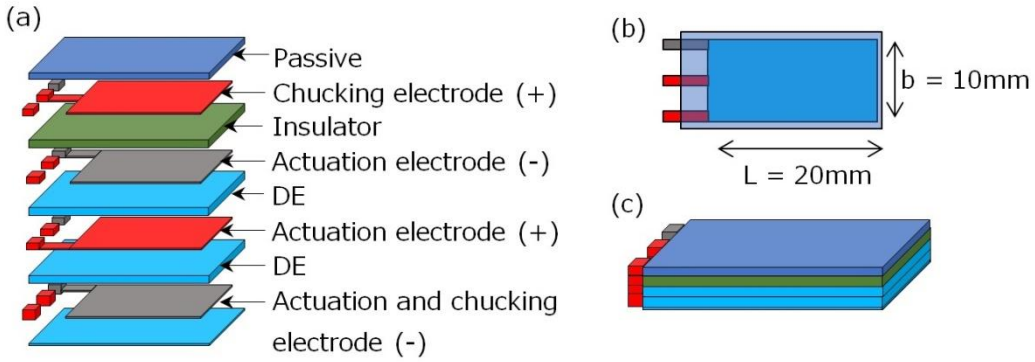

Figure 36. (a) Exploded diagram showing structure of DEA units and (b) top view and (c) oblique view of DEA units.

The P-VSDEA, shown in Figure 37, consists of numerous DEA units, stacked such that the positive chucking electrode of each DEA unit is adjacent to the ground electrode of the next DEA unit. Electrostatic force between each unit is generated by applying a voltage between these two corresponding electrodes, essentially making the entire P-VSDEA a single electrolaminate. The root areas of the DEA units near the electrode terminals are bonded together, while the remaining area is left unbonded.

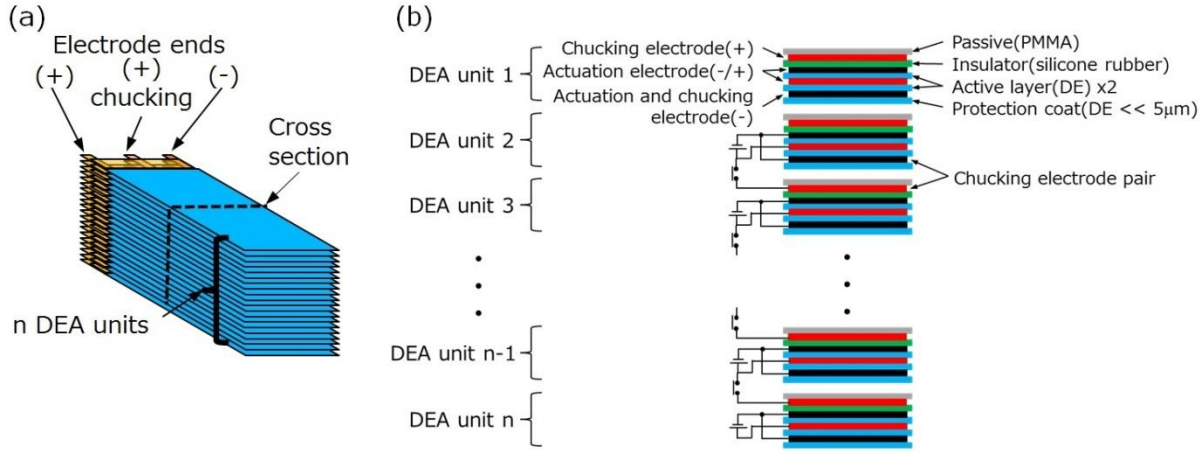

Figure 37. (a) Schematic diagram showing structure of P-VSDEA, and (b) exploded cross-section of P-VSDEA with electrical connections.

The P-VSDEA has two actuation modes: low stiffness for large displacement, and high stiffness for large holding force. Figure 38 demonstrates the use of both modes to manipulate a heavy object. In the low-stiffness mode, electrostatic chucking is turned off and the interfaces between the DEA units are free to slip, resulting in low stiffness of the P-VSDEA. Thus, when voltage is applied to the actuation electrode, the P-VSDEA can undergo large deformation to conform to an

object. When electrostatic chucking is turned on, the electrostatic attraction between the positive charge held on the chucking electrode and negative charge on the adjacent ground electrode causes the interfaces to become tightly bonded, and the VSDEA becomes correspondingly stiffer. In this stiff state, the VSDEA can then manipulate the object with greater authority. With this VSDEA concept, the displacement and holding force characteristics are determined separately: maximum displacement is determined by the design of the DEA unit (e.g. DE layer thickness and stiffness, number of DE layers, DEA unit length), while the bending stiffness of the VSDEA is controlled by the number of DEA units. The ability to control each parameter of the VSDEA's actuation independently is a great advantage.

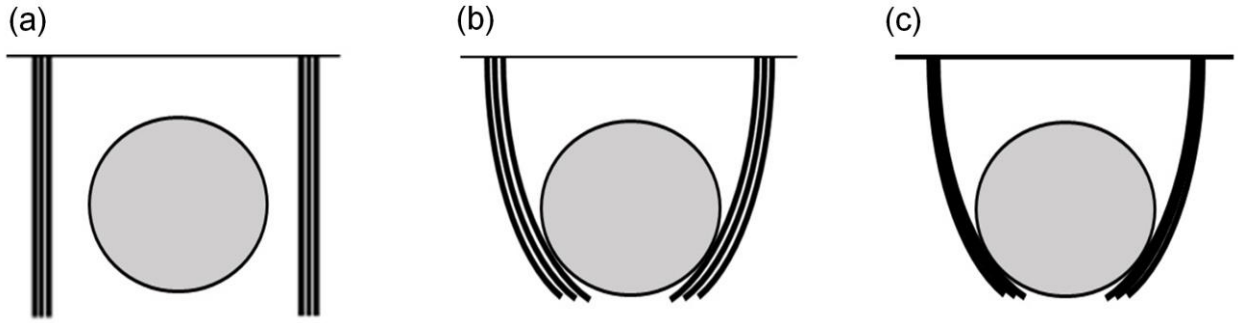

Figure 38. Operating process of P-VSDEA claw gripping an object, with actuators (a) no actuation or chucking voltage applied, (b) actuation voltage applied, (c) actuation and chucking voltage applied.

4.3.2 Modeling of VSDEA performance

The holding force of the P-VSDEA depends on the increase in stiffness by electrostatic chucking between the DEA units. In this section, equations for tip displacement of the fully-chucked VSDEA are derived (wherein all DEA units are perfectly bonded by electrostatic attraction). Axial and shear stress distributions are also derived to determine the interfacial shear strength required to support a given load. In the following analysis, it is assumed that (i) static equilibrium holds, (ii) Euler-Bernoulli beam theory holds, and (iii) no slip occurs at all bonding surfaces. The stiffness of the P-VSDEA is evaluated in the deformed shape as shown in Figure 39, with radius of curvature R and subtended angle θ. The actuator is fixed at S at $\alpha = \theta$, with a concentrated load (decomposed into radial and tangential components) due to weight of the object acting at its free end T at $\alpha = 0$.

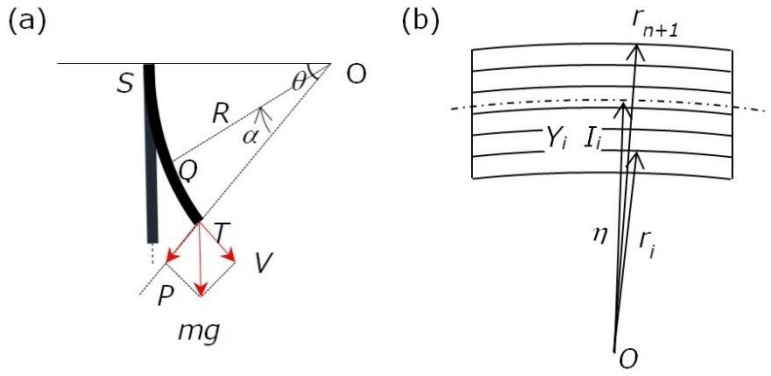

Figure 39. (a) Shape of deformed P-VSDEA and acting forces, (b) configuration of lamina.

The P-VSDEA consists of n laminae shown in Figure 39b. The neutral axis radius η is a function of the Young's modulus of each lamina Y_i' and laminar radii r_i (56). Bending stiffness of the actuator D is derived as (57), where b denotes the width of the actuator beam and I is the moment of inertia about the neutral axis.

$$\eta = \frac{\sum_i^n Y_i'\left(r_{i+1}^2 - r_i^2\right)}{2\sum_i^n Y_i'\left(r_{i+1} - r_i\right)} \tag{56}$$

$$D = \sum_i^n Y_i' I_i = \frac{b}{3}\sum_i^n Y_i'\left\{(r_{i+1}-\eta)^3 - (r_i-\eta)^3\right\} \tag{57}$$

A strain energy method (Castigliano's theorem) is used to predict the displacement of curved P-VSDEA due to the weight of the object. A bending moment M occurs due to radial force P and tangential force V at Q (58). The strain energy U is a function of the bending moment (59).

$$M = VR(1-\cos\alpha) - PR\sin\alpha \tag{58}$$

$$U = \int_0^\theta \frac{M^2}{2D} R d\alpha \tag{59}$$

Evaluation of the integral in (59) and differentiation with respect to the tangential and radial forces yields the tip displacements in the tangential and radial displacements, respectively as (60) and (61).

$$u_V = \frac{\partial U}{\partial V} = \frac{R^3}{2D}\left\{V\left(3\theta - 4\sin\theta + \frac{1}{2}\sin 2\theta\right) + P\left(2\cos\theta - \frac{1}{2}\cos 2\theta - \frac{3}{2}\right)\right\} \tag{60}$$

$$u_P = \frac{\partial U}{\partial P} = \frac{R^3}{2D}\left\{V\left(2\cos\theta - \frac{1}{2}\cos 2\theta - \frac{3}{2}\right) + P\left(\theta - \frac{1}{2}\sin 2\theta\right)\right\} \tag{61}$$

Since the P-VSDEA consists of many laminae bonded by electrostatic force, having an expression for the shear stress distribution in the actuator is important to predict the maximum weight the actuator can hold. The balance of forces by a shear stress τ at an arbitrary face at the radius $r = r_c$, and change of axial stress σ at a differential length dx along the lengthwise direction of the beam is shown in Figure 40. Consider the equilibrium of forces at arbitrary face ($r = r_c$): T_1 is a shear force at a surface $r = r_c$ in the k-th lamina, T_2 is the normal force, realized as the integral of the axis stress over the area of the bottom surface $r = r_1$ to the surface $r = r_c$ (62) - (64).

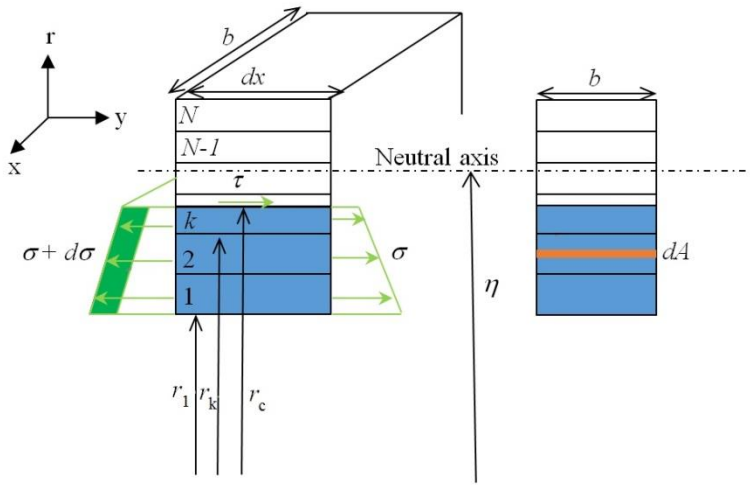

Figure 40. Axial stress distribution and equilibrium of forces.

$$T_1 + T_2 = 0 \tag{62}$$

$$T_1 = \tau b dx \tag{63}$$

$$T_2 = \int_{r_1}^{r_c} d\sigma dA \tag{64}$$

Solving for the shear stress yields (65), where the axial stress distribution is written as (66) and the differential length dx is written as (67). The differential of stress σ is written as (68). Finally substituting (68) into (65) yields (69), the expression for shear stress at a given radial and

tangential position in the actuator. It is also noted that *r'* denotes the distance from the neutral axis (70).

$$\tau = \frac{1}{b}\int_{r_1}^{r_c} \frac{d\sigma}{dx} dA \tag{65}$$

$$\begin{aligned} \sigma &= \frac{Y_i' M}{D}(r-\eta) \\ &= \frac{Y_i'\{VR(1-\cos\alpha) - PR\sin\alpha\}}{D}(r-\eta) \end{aligned} \tag{66}$$

$$dx = Rd\alpha \tag{67}$$

$$\frac{d\sigma}{dx} = \frac{1}{R}\frac{d\sigma}{d\alpha} = \frac{V\sin\alpha - P\cos\alpha}{D} Y_i'(r-\eta) \tag{68}$$

$$\begin{aligned} \tau(r,\alpha) &= \frac{V\sin\alpha - P\cos\alpha}{D}\int_{r_1}^{r_c} Y_i'(r-\eta)dr \\ &= \frac{V\sin\alpha - P\cos\alpha}{2D}\left\{\sum_{i=1}^{k-1} Y_i'\left(r_{i+1}'^2 - r_i'^2\right) + Y_k'\left(r_c'^2 - r_k'^2\right)\right\} \end{aligned} \tag{69}$$

$$r' = r - \eta \tag{70}$$

The above analysis assumes that the elements of the P-VSDEA are fully adhered to each other, but the strength of the interface between each DEA unit actually depends on the shear strength of the interface. Thus, to obtain the maximum possible increase in stiffness of the P-VSDEA, it is necessary for the chucking interfaces to have shear strength greater than the maximum shear stress predicted by (69). The shear strength can be described by the following equation utilizing Coulomb force. In this case, the Johnsen-Rahbek effect is ignored for the sake of simplicity [40]. Here, μ denotes the coefficient of static friction, t_D is the dielectric layer thickness, t_{CL} is the contact layer thickness, and δ is a physical gap between the interfacial surfaces.

$$\tau_r = \frac{\mu\varepsilon_0 E^2}{2}\left(\frac{\varepsilon_r}{t_D + \varepsilon_r(\delta + t_{CL})}\right)^2 \tag{71}$$

4.3.3 Fabrication of DEA units

The materials used for the DEA units are as follows. PVDF terpolymer P(VDF-TrFE-CFTE) (Piezotech S.A.S.) was used as a dielectric material, in 5.55 wt% solution dissolved in MEK

(Methyl Ethyl Ketone). This material was used rather than the P(VDF-TrFE-CFE) used in Chapter 3.1.2 due to unavailability of the material, though both materials have similar permittivity and stiffness. The electrodes consisted of silicone emulsion polymer (KM2002L-1, Shin Etsu Corporation) and 4 wt% aqueous dispersion of MWCNT (Nanocyl S.A.). The passive layer was made from 12 wt% PMMA (120,000 MW, Sigma-Adrich) solution in chloroform.

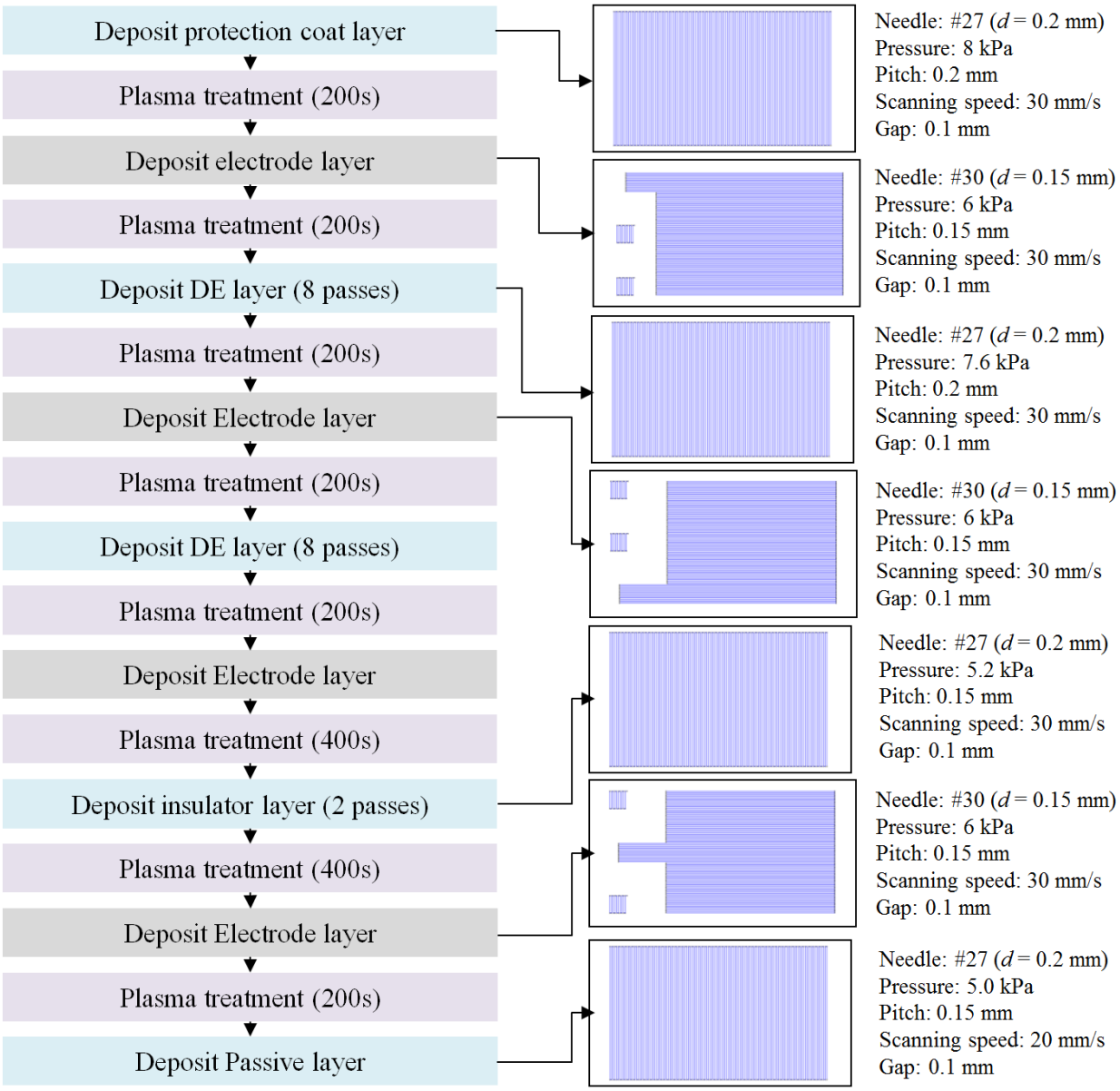

Figure 41. Fabrication flow chart for DEA and deposition parameters.

All samples were fabricated using the robotic dispenser system, using plasma treatment between deposition steps, with a similar method as described in Chapter 3.1.2. A flow chart of the fabrication process is shown in Figure 41.

4.3.4 Assembly of VSDEA

After the production of the desired number of DEA units, the P-VSDEA materials are qualified and assembled in the following steps:

1. DEA units are tested against dielectric breakdown by applying 550V to the actuation terminal for 2 minutes.
2. DEA units are tested against breakdown of the insulating and passive layer by applying 55V to the chucking terminal for 10 seconds.
3. DEA are stacked and adhered at the root by instant adhesive, as shown in Figure 42.
4. External connections to electrode connections are established using copper tape, and DEA stack is sandwiched between glass plates at the root.
5. Root of P-VSDEA between glass plates is potted in epoxy resin.

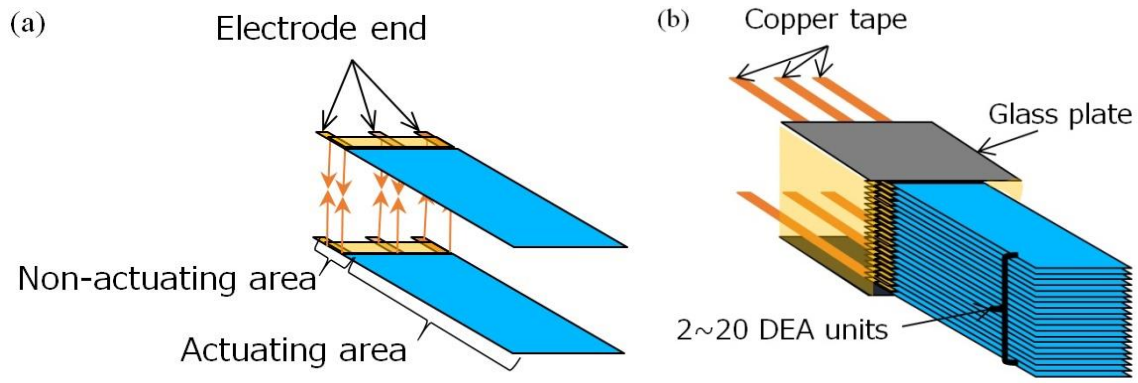

Figure 42. (a) Bonding of DEA units, (b) schematic diagram of assembled VSDEA.

The success rate of the breakdown tests in steps 1 and 2 were 85.3% and 84.6%, respectively, resulting in a total success rate of 72%, out of all DEA units fabricated. A completed P-VSDEA with 15 DEA units is shown in Figure 43.

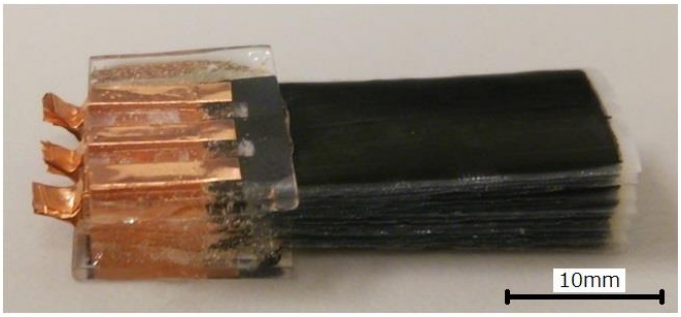

Figure 43. Completed VSDEA consisting of 15 DEA units.

In the deposition process, it was observed that the DEA unit thickness was inhomogeneous, being thicker along their edges. The thickness distribution of 3 samples along their width was measured using a micrometer; the result is shown in Figure 44.

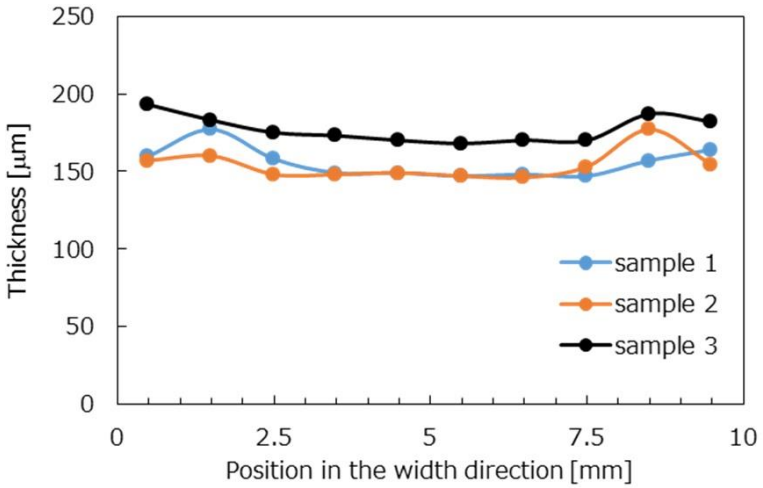

Figure 44. Thickness distribution in the width direction.

4.3.5 Experimental results

Bending displacement and blocking force of the DEA units was performed. A laser displacement sensor (Keyence LK-081) was used to measure the tip displacement, and a load cell (Transducer Techniques GSO-10) was used for the blocking force measurements. All voltages were applied as a step input. Measurements taken after 1 s of deformation are shown in Figure 45, compared to results from the elastic model derived in Chapter 3.2.1. Input data for the model is tabulated in Table 16. Progression of the widthwise and lengthwise curvature of the DEA units is shown in Figure 46.

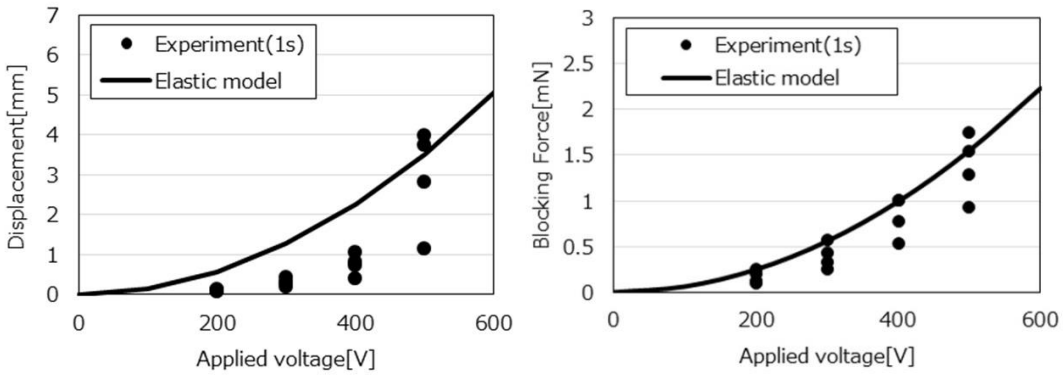

Figure 45. Comparison of measured displacement and blocking force, and elastic model.

Table 16. Thickness and material properties for P-VSDEA.

	Thickness	Young's modulus	Poisson's ratio	Dielectric constant
DE layer	10.6 μm	250 MPa	0.5	50
Electrode layer	18.7 μm	4.02 MPa	0.5	-
Insulator layer	56.3 μm	1.00 MPa	0.5	-
Passive layer	16.1 μm	1720 MPa	0.35	-

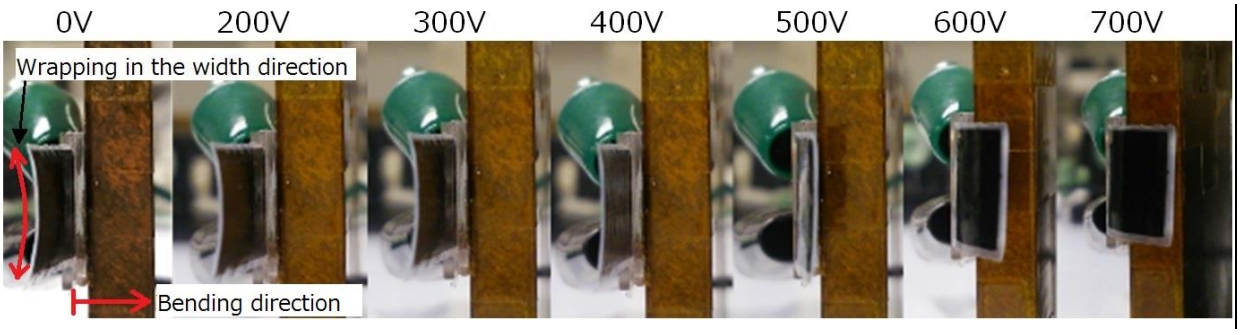

Figure 46. Bending deformation at each applied voltage.

Knowing the shear strength of the DEA unit interfaces against the bending moment in P-VSDEA is important to predict the limitation of the bending stiffness of the actuator. The shear strength was measured by the measurement setup shown in Figure 47. DEA 1 is held and DEA 2 is connected to a force gauge (Shimpo FGV-1XY) fixed on a sliding stage. The sliding stage can be moved manually by a micro adjuster. The area of electrostatic chucking is 10 x 20 mm. Measured shear strength at each voltage are shown with the prediction by equation (71) in Figure 48. The prediction line based on Coulomb chuck model corresponds to ε_r = 3.5, μ = 0.5, t_D = 16.1 μm, t_{CL} = 1 μm and δ = 0.

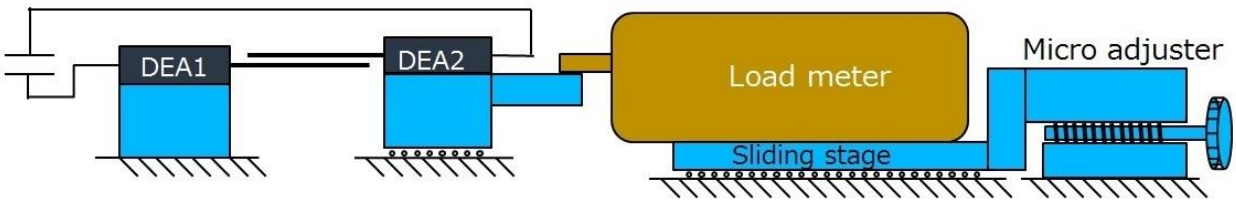

Figure 47. Experimental setup for shear strength measurement.

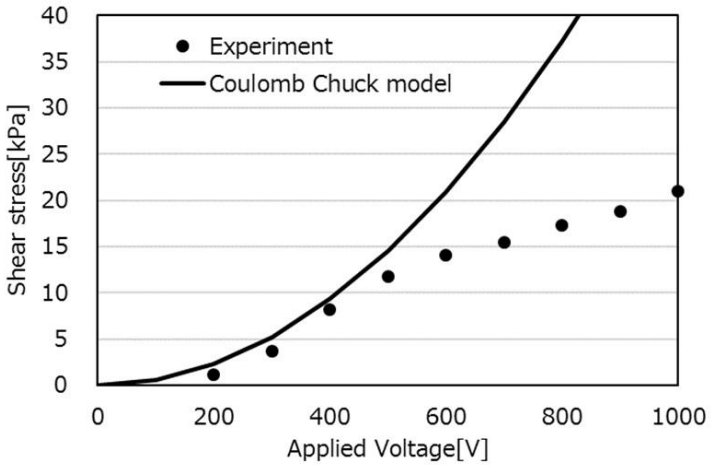

Figure 48. Measured shear strength and Coulomb model.

Bending stiffness of P-VSDEA consisting of 2, 4, 6, 8, 10, 15, and 20 DEA units was performed. VSDEA were deformed by applied voltage, and then the chucking voltage was applied. The stiffness of the actuators was measured in the deformed shape to simulate a situation similar to the actual operation of the actuator, as shown in Figure 49. The measured bending stiffness is shown in Figure 50, along with the theoretical maximum bending stiffness predicted by Equation (61). The maximum stiffness increase observed in the P-VSDEA is shown in Table 17.

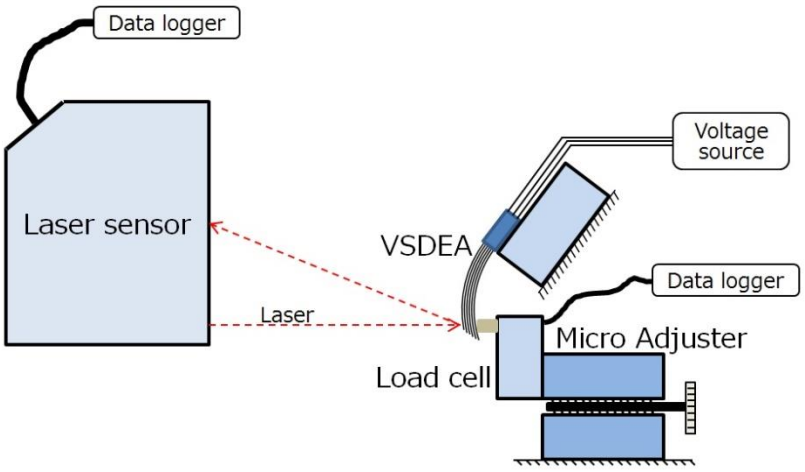

Figure 49. Experimental setup for measurement of bending stiffness.

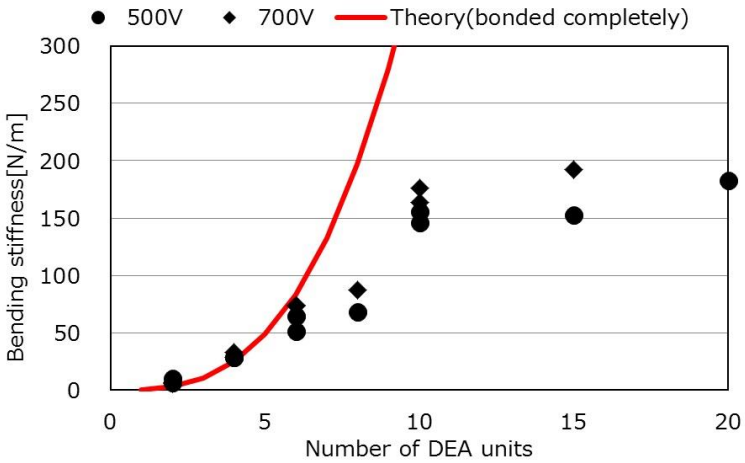

Figure 50. Bending stiffness of P-VSDEA at 500V and 700V, with prediction based on model with completely bonded interfaces.

Table 17. Stiffness increase observed in P-VSDEA at 700V. *Measured at 500V

# of DEA units	Stiffness increase (at 700V)
2	11.5
4	18.0
6	27.4
8	24.3
10	39.1
15	30.4
20*	20.3*

A claw actuator based on P-VSDEA was designed to hold a target weight of 10g. A schematic image of the claw actuator is shown in Figure 51. It consists of two P-VSDEA units, each

consisting of six DEA units. Equations (60) and (61) were used to predict the axial and shear stress in the actuators while holding the 10g mass, and results are shown in Figure 52, where each curve indicates the axial or shear stress along the thickness of the P-VSDEA. As stated earlier, it is important that the shear strength of the electrostatically chucked interfaces exceeds the maximum shear stress predicted to exist in the P-VSDEA under loading. To this end, the maximum shear stress expected in the P-VSDEA is approximately 2.5 kPa, which is much lower than the measured shear strength of the interface at 500V shown in Figure 52, 11.8 kPa.

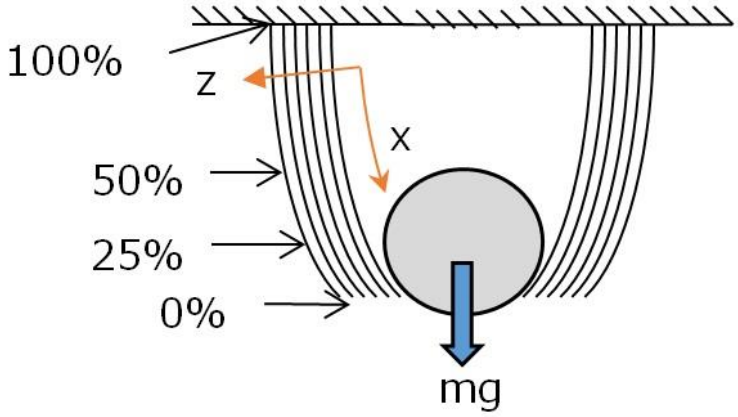

Figure 51. Schematic of two-claw actuator, showing positions along actuator length corresponding to predictions in Figure 52.

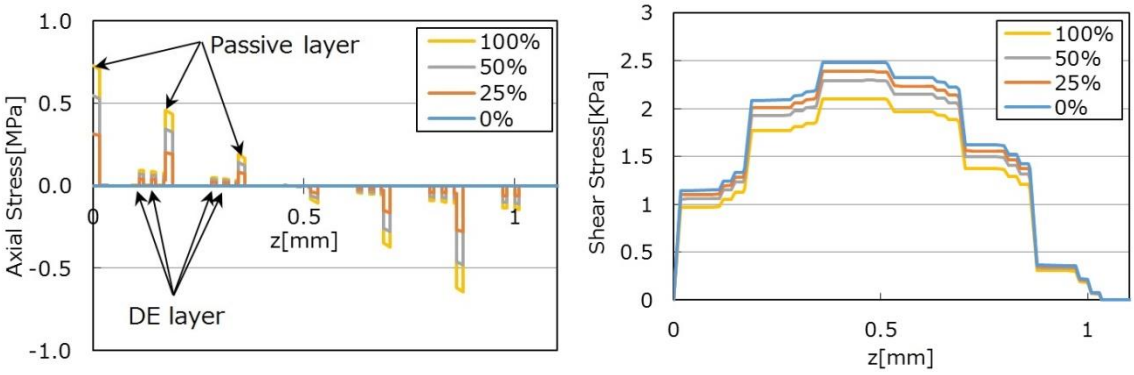

Figure 52. (a) Axial and (b) shear stress distribution though the thickness of the P-VSDEA.

A gripping test was conducted wherein the claw actuator would attempt to lift objects of successively larger mass until the object slipped from its grasp. The object, supported by a platform, was placed at approximately 25% of the actuator length from the tip, and the actuation and chucking voltages were applied such that the actuator grasped the object. The object's support was removed so that it was being solely supported by the claw actuator. A demonstration

of the maximum weights held during the gripping test is shown in Figure 53. The maximum weights that the claw actuator could support were 2.5g, 5.8g, and 10.2g at 500V, 600V, and 700V, respectively. The test at 700V demonstrates the ability for the claw actuator to lift 17 times its own weight (10.2g / 0.6g).

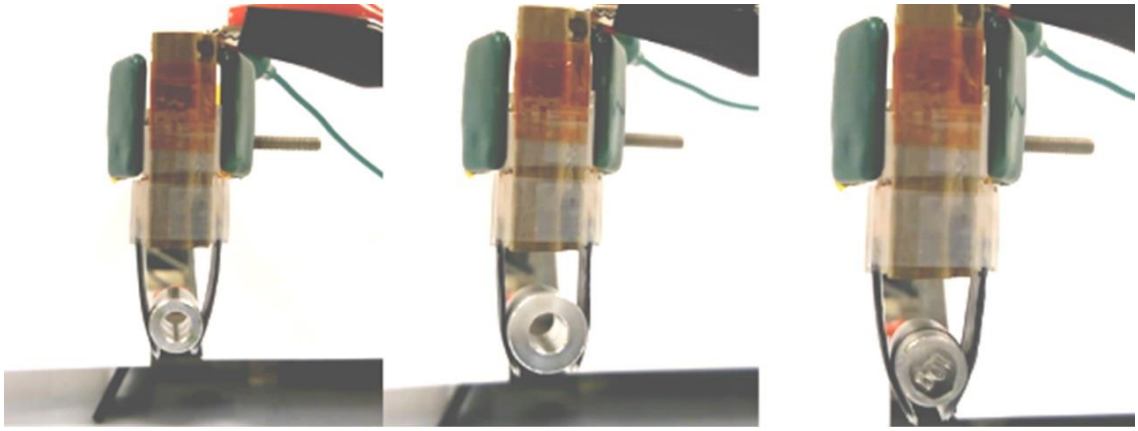

Figure 53. Gripping test of claw actuator, supporting (a) 2.5 g (b) 5.8 g, (c)10.2 g objects.

4.3.6 Discussion

The experimental data for bending displacement and blocking force (Figure 45) agrees reasonably well with the elastic model predications, except for the region from 200-400V in the case of the bending displacement. This is likely due to the strong initial curvature of the DEA units, which is only overcome at higher voltages. This effect is shown in Figure 46, where the DEA only transitions to a flat shape at around 500V. The agreement in the case of blocking force is much better, since the tip of the units is fixed, so the initially warped shape does not affect the performance of the DEA units.

The experimental data for shear strength generated by electrostatic chucking (Figure 48) agrees reasonably well with the model predictions, up to about 500V, beyond which the model overpredicts the shear strength. The model predicts quadratic increase of the shear strength, while beyond 500V the experimental data appears to increase linearly. One possible reason for this disparity is leakage of electric charge, though it is difficult to discern exactly the cause. Another possible reason is that microscopic gaps between the chucking surfaces due to surface roughness cannot be overcome by successively greater chucking voltage, so the increase in shear strength does not occur as rapidly.

The measured bending stiffness of VSDEA (Figure 50) agrees well with the model prediction for P-VSDEA with fewer numbers of DEA units (i.e. N = 2, 4, 6) but for larger quantities, the measured stiffness is much lower. There are two reasons in particular why this may occur:

1. Inhomogeneity of the DEA units in the width direction causes gaps between the units when chucking is turned on, particularly because the thickness inhomogeneity increases proportionally to the number of units. Figure 54 illustrates this problem, showing that not all DEA units may be chucked, having a deleterious effect on bending stiffness.
2. It is difficult to enforce contact of the DEA units near the root of the P-VSDEA, because of the presence of the adhesive used to bond them. Even though this gap is not visible to the naked eye, each unit is separated at the root by approximately 15 μm exists because of the finite thickness of the glue. This gap at the root area can cause buckling of the actuator when loading is applied. This issue is illustrated in Figure 55.

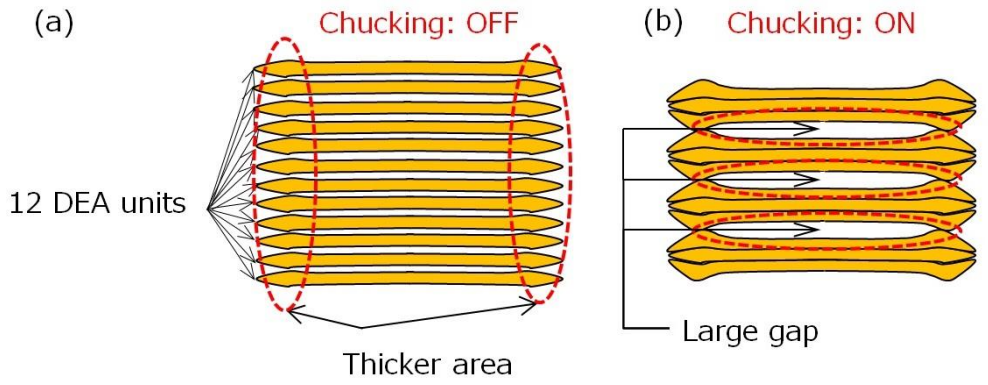

Figure 54. Influence of uneven thickness distribution in DEA units, shown with (a) chucking turned off and (b) turned on.

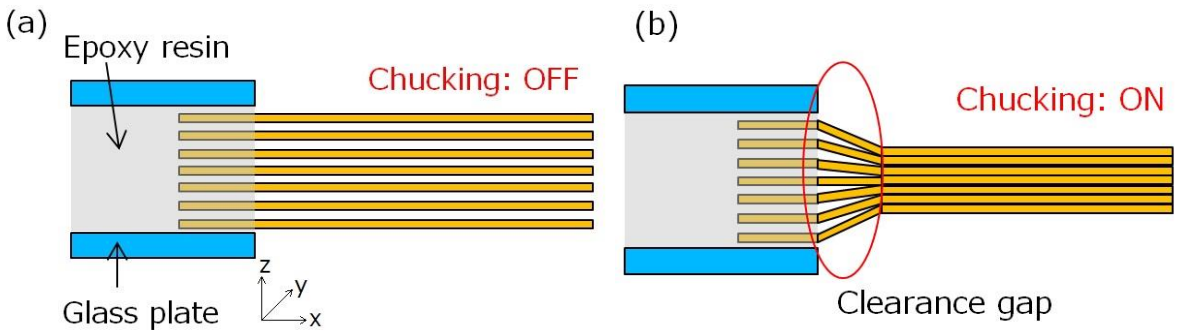

Figure 55. Influence of gaps between DEA units at root, shown with (a) chucking turned off and (b) turned on.

Despite the above reasoning, it was expected that the P-VSDEA claw actuator would be able to lift a 10g object at a chucking voltage of 500V; instead 700V was required. The shear strength measured at 500V (11.8 kPa) exceeded the predicted maximum shear stress (2.5 kPa), and the measured stiffness of the chucked 6-unit P-VSDEA matched reasonably well with the theoretical prediction. The experimental increase in stiffness between 500V and 700V is only approximately 35%, yet the weight that the actuator could lift increased over four-fold, from 2.5g to 10.2g. It seems possible that even at 500V, due to inhomogeneity of the DEA units, a gap between the units may have occurred. By increasing the voltage to 700V, the electrostatic attraction was sufficient to decrease this gap. It has been observed that increasing the chucking voltage causes a positive feedback loop – increasing the electrostatic force causes the gap between the units to close, even further increasing the force until the gap is closed. Looking back to Chapter 4.2.3, this sort of behavior is exhibited in Figure 35, where the electrolaminate stiffness increases vastly between 150V and 200V. Increasing the voltage from 500V to 700V in the P-VSDEA case may have been the catalyst to close any remaining gaps and cause the four-fold increase in load-carrying capacity.

4.4 Conclusions

The intrinsic softness of dielectric elastomer actuator materials offers unique advantages for soft robots compared to existing robots consisting of rigid frames and actuators. However, their softness limits their applications due to their low load capacity. Variable stiffness actuators based on electrolaminates with stiffness change of up to 39× with fast transition time under 1 second have been demonstrated. An actuator constructed from two such actuators was able to lift 17 times its own weight. This type of variable stiffness DEA meets or exceeds the capabilities of

prior variable stiffness DEA based on phase change of low-melting-point alloys. That said, there are challenges for implementing electrolaminate-based VSDEA; namely the available stiffness increase saturates rapidly with increasing number of DEA units; inhomogeneity from the fabrication process unequivocally has deleterious effects on its performance.

5. Dielectric elastomer sensors

5.1 3D Tactile force sensing DES array

5.1.1 Working principle

The transducer nature of DE allows it to be used as a sensor. Deformation of the DE membrane results in a number of phenomena which can be leveraged as a sensing material, including generation of charge and change in impedance. A simple tactile DE sensor can be made by sandwiching a planar piece of DE between two compliant electrodes, forming a parallel plate capacitor, with capacitance determined by the well-known parallel-plate equation (72). Applying a force normal to the surface of the sensor compresses the membrane, decreasing the electrode separation and thus increasing the sensor's capacitance. Similar capacitive DE sensors rely on deformation of DE membrane in the plane, observing the capacitance change due to the change in electroded area.

$$C = \frac{\varepsilon_o \varepsilon_r A}{d} \tag{72}$$

Normal and shear tactile forces can be determined by measuring the capacitance change of a DES with a segmented electrode due to reaction forces at the base of a protruding feature such as a soft dome (Figure 56). Dividing the electrode into four segments forms four capacitors with a common ground. The magnitude and sign of the capacitance change of each of the DES' segments depends on the magnitude and direction of the tactile force acting on the dome (Figure 57). Pure normal force acting on the dome results in compression and thus increased capacitance of all four segments of the sensor. On the other hand, pure shear force results in compression and increased capacitance of the segments on one side of the sensor, and has the converse effect on the other. By measuring the capacitance change of all four segments of the segmented sensor, it is possible to determine the normal and shear components of the tactile force acting on the sensor. A 3x1 array of 3D tactile sensors was fabricated to evaluate their performance.

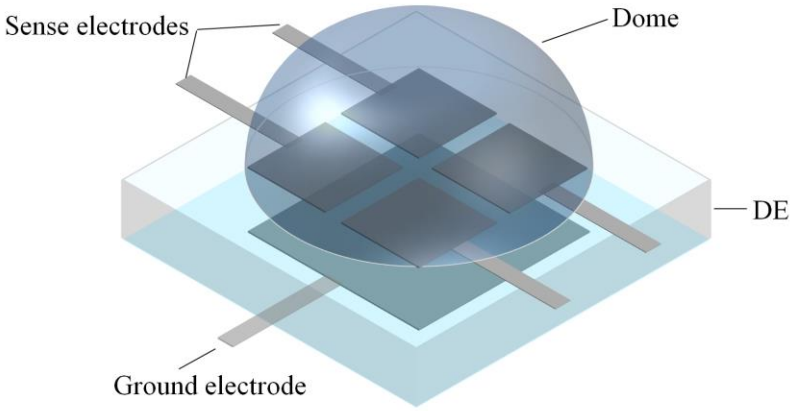

Figure 56. Structure of 3D tactile force sensing DES.

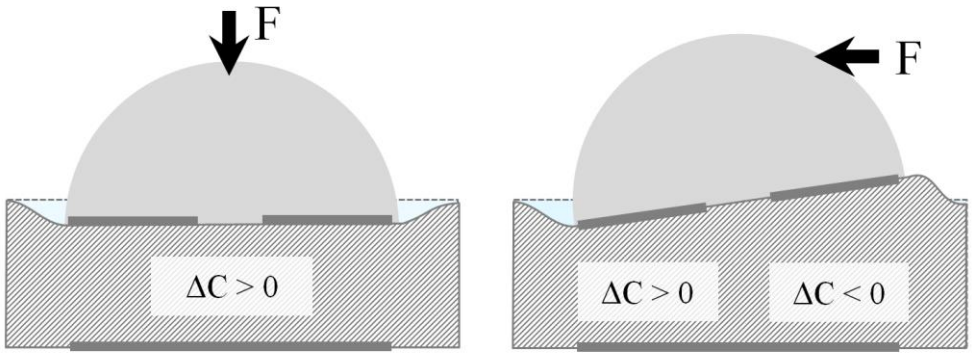

Figure 57. Cross-sectional views of tactile DES under normal and shear force.

5.1.2 Fabrication

Material properties of the DES materials are summarized in Table 18. A silicone emulsion polymer (KM2002L-1, Shin-Etsu Chemical) was used as the DE material. Silicone was selected for its low stiffness, as the sensor's sensitivity is proportional to its compliance. Additionally, the silicone emulsion polymer has low viscosity and cures rapidly in air without heat acceleration, which lends itself to deposition by a dispenser. The electrode solution consisted of a solution of multiwall carbon nanotubes (MWCNT) dispersed in water (Nanocyl NC7000) and the silicone emulsion polymer. The solution was mixed by a planetary centrifugal mixer for 10 minutes. The aqueous dispersion and mixing prevents aggregation and thus clogging of the MWCNT in the dispenser. PMMA (120,000MW, Sigma-Aldrich) 10 wt% in chloroform was used a support layer for peel-off from the glass substrate.

Table 18. Summary of DES material properties

	Young's Modulus [MPa]	Dielectric Constant	Sheet Resistance [kΩ/sq.]
KM-2002L-1	0.2	3.0	-
Nanocyl [2 wt%] + H_2O [48 wt%] + KM-2002L-1 [50 wt%]	3	-	0.37
PMMA (MW =120,000)	1600	-	-

The DES laminate was fabricated by deposition of liquid solutions by the robotic dispenser system. The dispensing patterns are shown in Figure 59, and a summary of deposition parameters is tabulated in Table 19. A glass slide was used as the substrate, prepared by cleaning with ethanol. The initial glass substrate and the sensor surface after each round of deposition was treated by plasma etching for 120s to improve wettability and adhesion between layers. Layers 1 and 2 consisted of DE and PMMA, respectively. The layer of soft DE material between the stiff glass and PMMA acts as a release agent, so that the DES could be peeled off of the substrate after completion. Layer 3 was an active shield consisting of the electrode solution. Shield layers were connected to the CDC and driven with the same signal as the sensor input so that no potential difference exists between the sensor and shield. As a result, interference due to parasitic capacitance becomes coupled to the shield and not the sensor. Layer 4 consisted of DE and insulates the shield from the ground electrode deposited in Layer 5. Layer 6 consisted of DE and is the dielectric material between the ground electrode of Layer 5 and sense electrodes of Layer 7. The capacitance of the sensor was measured between the aforementioned sense and ground electrodes. Layer 8 was another DE insulating layer between the sense electrodes and a second active shield was deposited in Layer 9. Layer 10 was a final insulating and protecting layer. This completes the dispensing process. The completed DES laminate is shown in Figure 58, and can be peeled off of the glass substrate.

Figure 58. Completed DES laminate after removal from glass substrate.

The dome-shaped features were molded from PDMS (Sylgard 184, Dow Corning) in an aluminum mold, and cured at 150°C for 15 minutes. The mixing ratio of silicone to hardener was 10:1 by weight. The PDMS after curing was slightly self-adhesive, allowing sufficient bonding to the surface of the DES laminate without adhesive. Each dome is 3mm in diameter, with 12mm pitch. Electrical connections to the DES were made by manually bonding wires to the trace terminations using the electrode solution.

The area of each sense electrode is approximately 1.2 mm^2 and the four sense electrodes have a combined footprint of approximately 8 mm^2. The sensor pitch is 12mm. Traces are approximately 500µm in width and have 1mm pitch, expanded to 1.4mm at the terminations. The total thickness of the DES laminate is 230µm. Each DE layer is approximately 20µm thick and the PMMA and electrode layers are each approximately 25µm thick.

Table 19. Summary of DES deposition parameters

Layer number	Material	Needle	Pressure [kPa]	Scanning speed [mm/s]
1, 2	Silicone, PMMA	30G (0.15mm)	6	100
3, 9	Silicone + MWCNT		6	60
4, 6, 8, 10	Silicone		8	60
5, 7	Silicone + MWCNT		5, 6	100/60/25

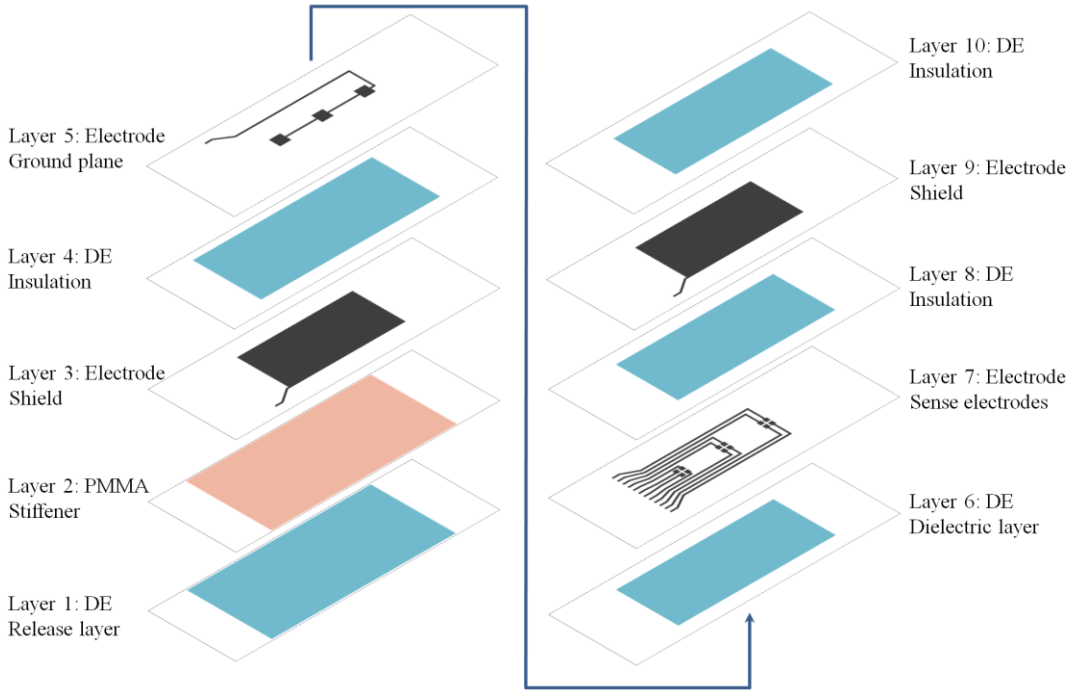

Figure 59. Dispensing patterns and dispensing order of DES laminate.

5.1.3 Signal processing

Capacitance of each sensor segment was measured by a CDC integrated circuit (Texas Instruments FDC1004 EVM), providing four capacitance measurements at 16-bit effective resolution at a rate of 100Hz. The 3x1 DES array requires 12 independent capacitance measurements. To this end, a 16-channel multiplexer (Texas Instruments CD74HC5067) routes the 12 capacitive inputs of the DES array to a single measurement channel of the CDC. The CDC and multiplexer are configured by a microcontroller (Atmel ATmega32u4) which transmits capacitance data to a PC via serial connection. The entire array can be scanned at approximately 8Hz. The sampling frequency of the CDC can be increased to 200Hz or 400Hz to increase the array scan rate to 16Hz or 32Hz, however at the expense of resolution. The signal processing system of the DES is shown in Figure 60.

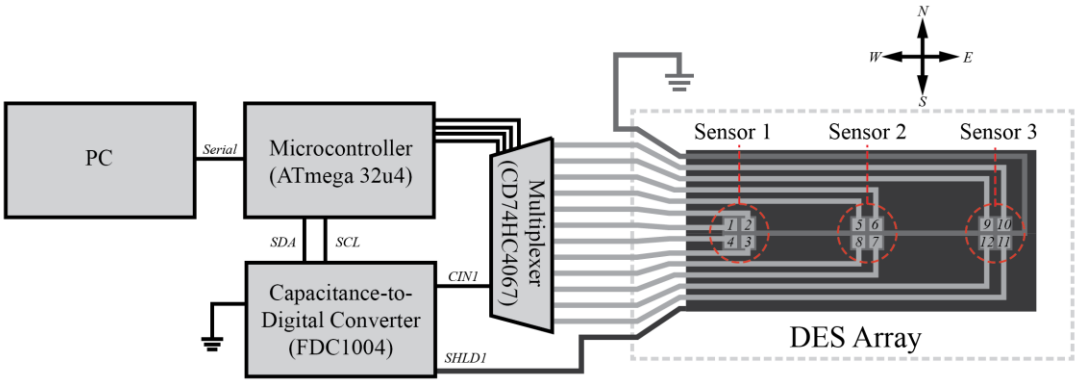

Figure 60. Signal processing system of DES array.

Capacitance data from the DES is reconstructed to approximate the tactile forces acting on the sensor using the following scheme. The capacitance changes measured from the four segments of each sensor are numbered according to the convention given in Figure 60 and stored in vector $\boldsymbol{C} = \{\Delta C_1, \Delta C_2, \Delta C_3, \Delta C_4\}$. Each segment's normal force sensitivity is determined empirically and stored in $\boldsymbol{S} = \{S_1, S_2, S_3, S_4\}$. The varying sensitivity of each segment due to variations in electrode area, thickness, and alignment of the dome layer, is normalized by the elementwise produce (73), where N is a vector of weights (74) based on the sensitivity of each segment.

$$\boldsymbol{N} = \frac{1}{\sum_{i=1}^{4} S_i} \boldsymbol{S} \tag{73}$$

$$\boldsymbol{C'} = \boldsymbol{N} * \boldsymbol{C} \tag{74}$$

The normalized signal is separated into shear and normal force components (76). The normal force component of the signal is the mean of the capacitance change, since a pure normal force is assumed to cause a uniform change in capacitance. The signal in capacitance is converted to shear and normal components by dividing by the sensor's sensitivity in the normal and shear directions (77)-(79).

$$C_n{}' = mean(\boldsymbol{C'}) \tag{75}$$

$$\boldsymbol{C_s}{}' = \boldsymbol{C}{}' - \boldsymbol{C_n}{}' \tag{76}$$

$$F_n = \frac{C_n'}{mean(\boldsymbol{S})} \tag{77}$$

$$F_W = \frac{(C_{s1}' + C_{s4})' - (C_{s2}' + C_{s3}')}{4S_W} \tag{78}$$

$$F_W = \frac{(C_{s1}' + C_{s2})' - (C_{s3}' + C_{s4}')}{4S_N} \tag{79}$$

5.1.4 Experimental results

The performance of the DES was evaluated via several experiments. The test setup shown in Figure 61 was used to apply normal and shear tactile forces to the DES and measure its response. It consists of a manually-operated 2-axis stage, and two force gauges each with resolution 1mN.

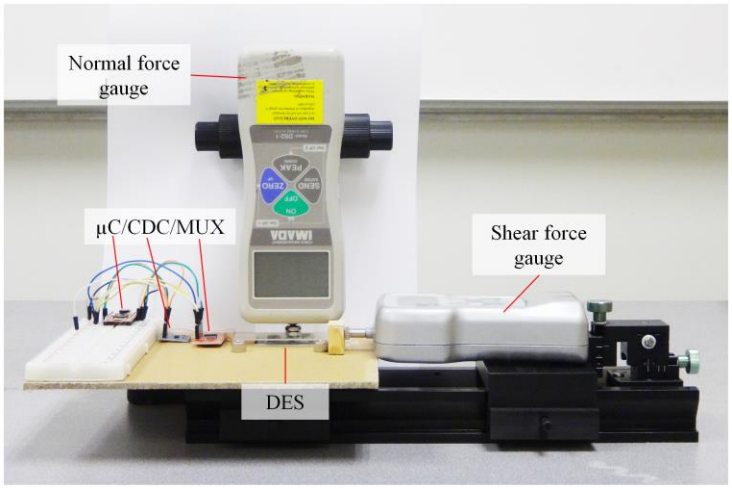

Figure 61. Test setup for applying tactile forces to DES.

The DES' response to normal and shear force is shown in Figure 62. Sensitivity to normal force was measured by applying force up to 5N in increments of 0.5N normal to the dome. Similarly, sensitivity to shear force was measured by applying a static 5N normal force to the dome, and subsequently applying increments of 0.5N in the west and north directions. The sensitivity to normal and shear force averaged across the four segments of a single sensor was 0.0188 pF/N, 0.0075 pF/N, and 0.0075 pF/N, respectively. Considering the 0.5fF effective resolution of the CDC, the effective resolution of the sensor was 27mN for normal force and 67mN for shear force.

A subsequent test was performed to evaluate the ability of the DES to approximate tactile forces using the method described in Section 5 and the measured sensitivity values. Figure 63 shows the sensor response when 5N normal force is applied, followed by 3N along the north-south axis, and along the northwest-southeast direction. In the north-south loading case, the average normal and shear force resolved by the sensor was 5.35N and 2.84N respectively. In the northwest-southeast loading case, the average normal and shear force resolved by the sensor was 5.29N and 3.16N respectively.

To evaluate crosstalk between the three sensors of the array, a 5N normal force was applied to each of the three sensors sequentially. The response is shown in Figure 64. Application of force to Sensors 2 and 3 had virtually no effect on the measurement of Sensor 1 but crosstalk is observed on Sensors 2 and 3, typically less than 20% of the peak value of the sensor. Sensors 2 and 3 have long traces which deform when tactile forces act on other sensors, resulting in a disturbance in their signal.

The DES' response to objects in close proximity due to capacitive coupling is shown in Figure 65. Three objects of varying size and dielectric constant were used; cardboard (45 x 45 x 5mm), aluminum (45 x 45 x 5mm) and a human hand.

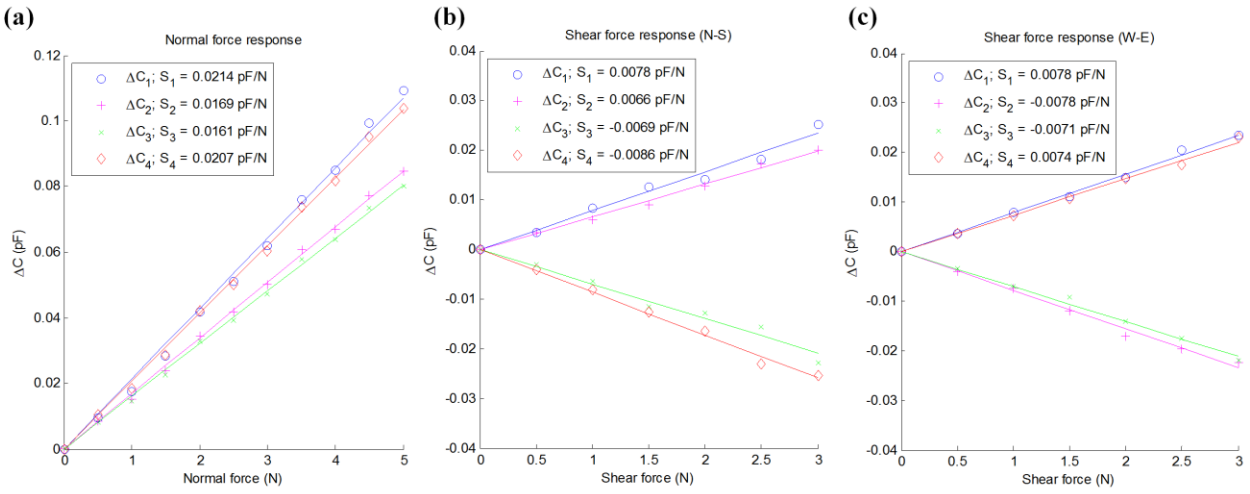

Figure 62. Response of DES to (a) normal, (b) shear in north-south direction, (c) shear in west-east direction.

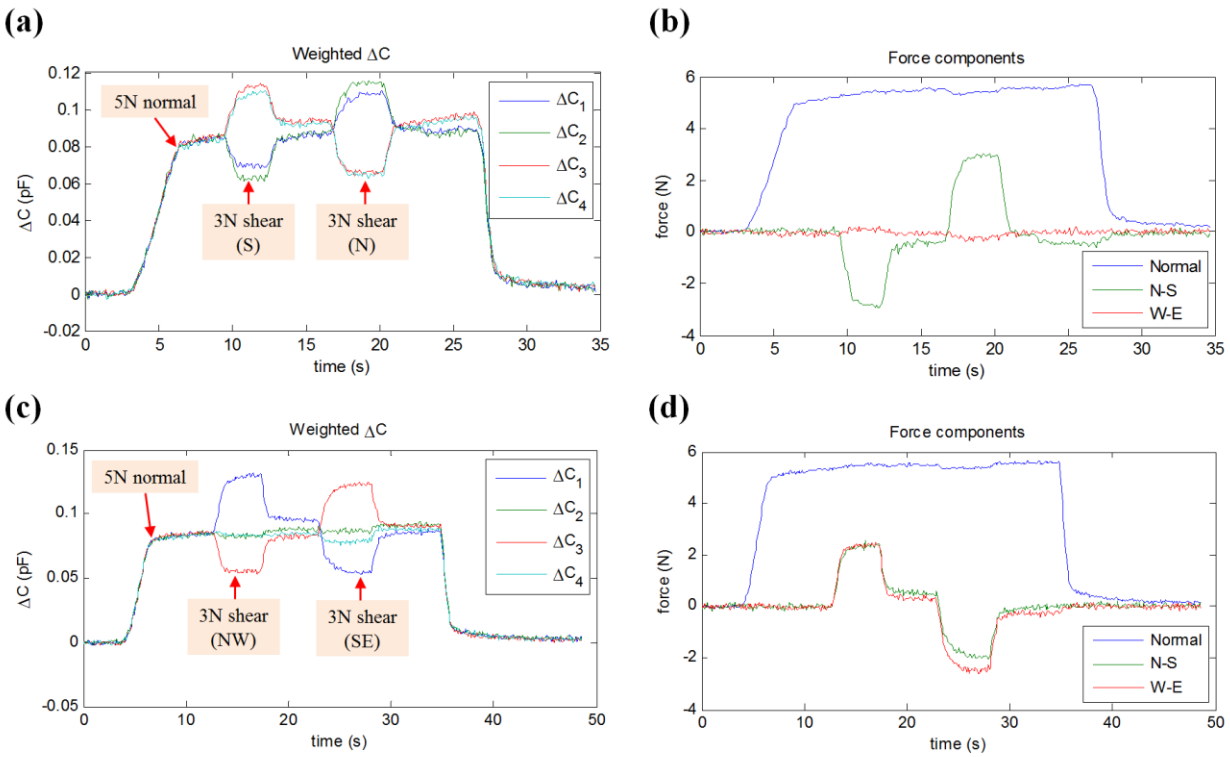

Figure 63. Response of DES to mixed normal and shear tactile forces in north-south direction (a, b), and northwest-southeast direction (c, d).

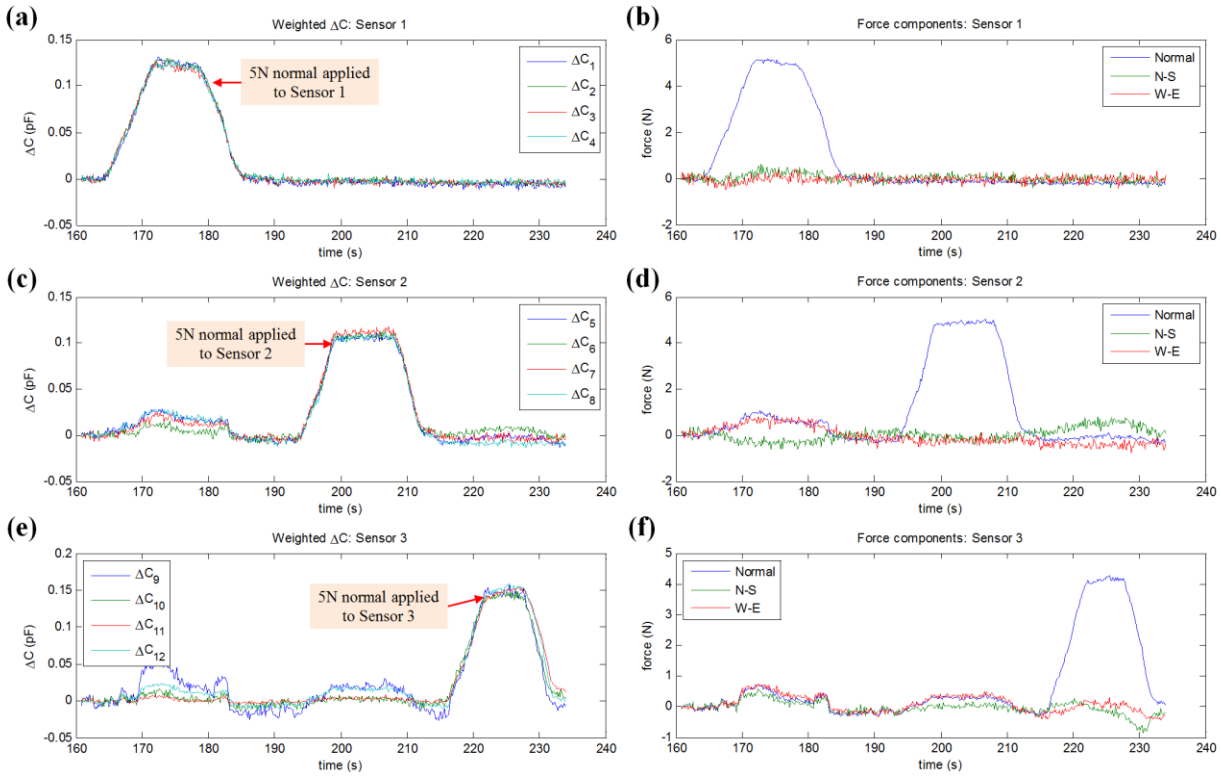

Figure 64. Response of DES array to normal force on sensor 1 (a, b), sensor 2 (c, d), and sensor 3 (e, f).

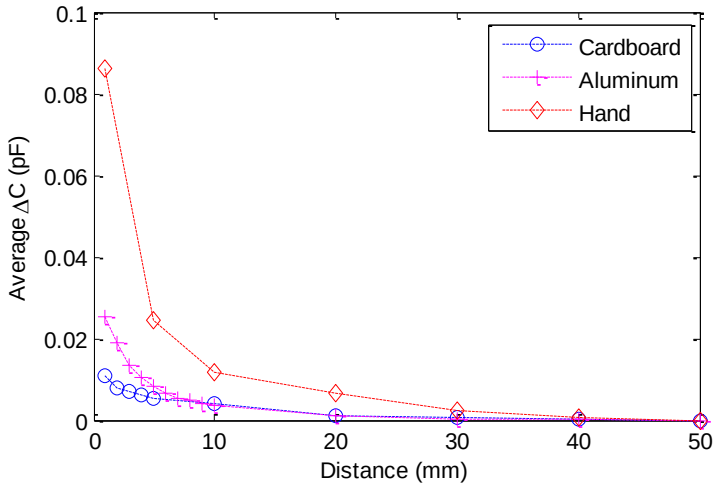

Figure 65. Proximity sensing behavior of DES for various objects.

5.1.5 DES laminate as a sensing passive layer

A tactile sensor-integrated DEA (TSDEA) is introduced, illustrated in Figure 66, consisting of a DEA laminate (fabrication discussed in Chapter 3.1) bonded to a DES laminate (fabrication and characterization discussed in Chapter 6). The structure is essentially a unimorph actuator;

expansion of the DEA laminate under applied voltage is constrained on one side by the DES laminate, resulting in bending. The DEA laminate consisted of four layers of 3M VHB F9469PC, with carbon black powder electrodes, with a final shape of 15mm by 35mm. The DEA and DES laminates were bonded using a spray adhesive (3M Super 77), and electrical connections were made by bonding wires to the trace terminations using the electrode solution. The completed TSDEA is shown in Figure 59.

Electromagnetic interference (EMI) on the DES caused by actuation of the DEA (2kV square wave, 0.1Hz) is shown in Figure 68. When voltage is applied to the DEA, the DES exhibits a transient spike in capacitance, approximately 0.03pF in height, which rapidly decays to an offset of approximately 0.008 pF. The offset remains after the voltage is switched off, possibly due to charge remaining on the actuator. The EMI seems to be partially mitigated by the active shielding layers of the DES, and the transient spikes in capacitance could be eliminated by a low-pass filter in post-processing of the data.

Figure 69 shows simultaneous actuation and sensing of the device with 2kV applied to the DEA. The displacement increases until $t = 4s$, when the tip contacts a steel object. Average capacitane of the three sensors of the array increases due to EMI from the DEA and also due to capacitive coupling with the steel object. Sensor 3 at the tip o the device exhibits the largest capacitance increase because of its proximity to the object, whereas the proximity effect on Sensors 1 and 2 is diminished. It was not possible to use the DES to measure the tactile forces induced by the DEA itself, since the 4-layer VHB DEA's maximum generative force was smaller than the minimum force resolvable by the sensor.

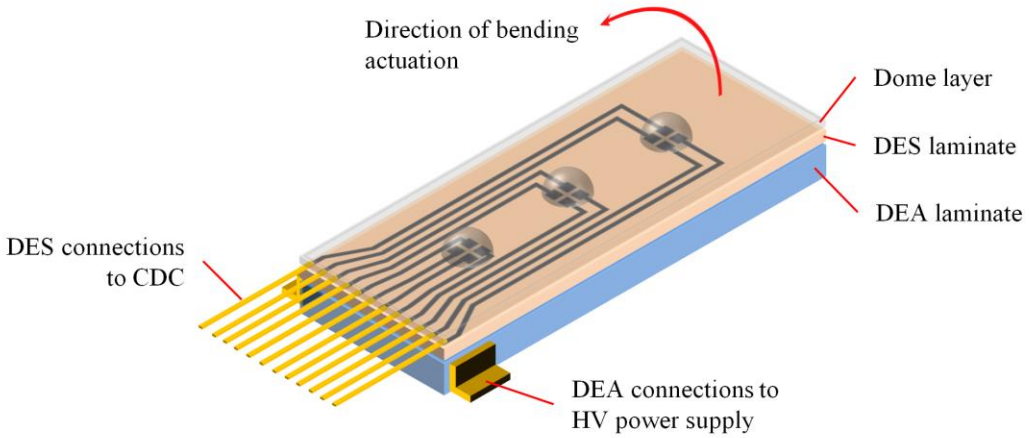

Figure 66. Design of tactile-sensor integrated dielectric elastomer actuator (TSDEA).

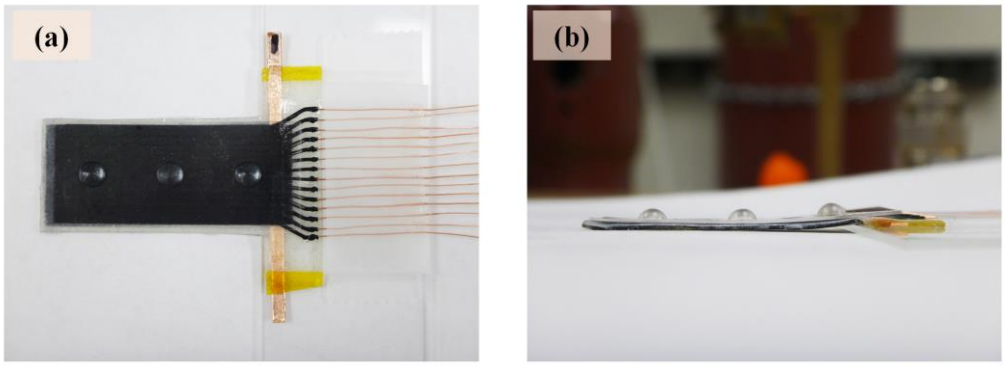

Figure 67. (a) Top view and (b) side view of completed TSDEA.

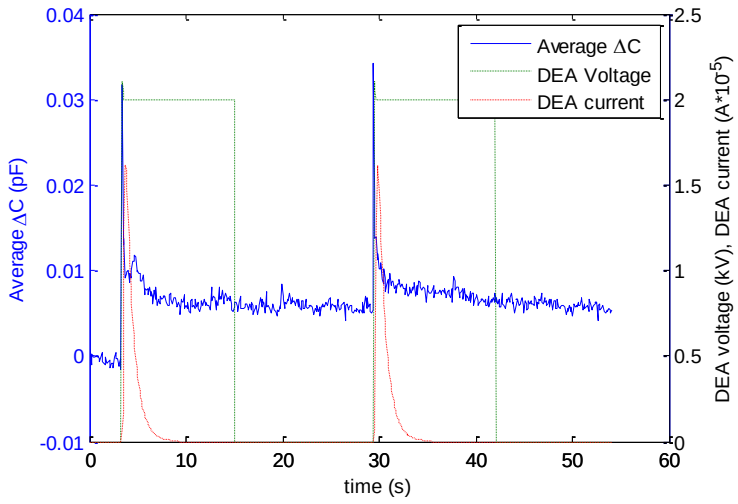

Figure 68. Influence of EMI from DEA actuation on DES response.

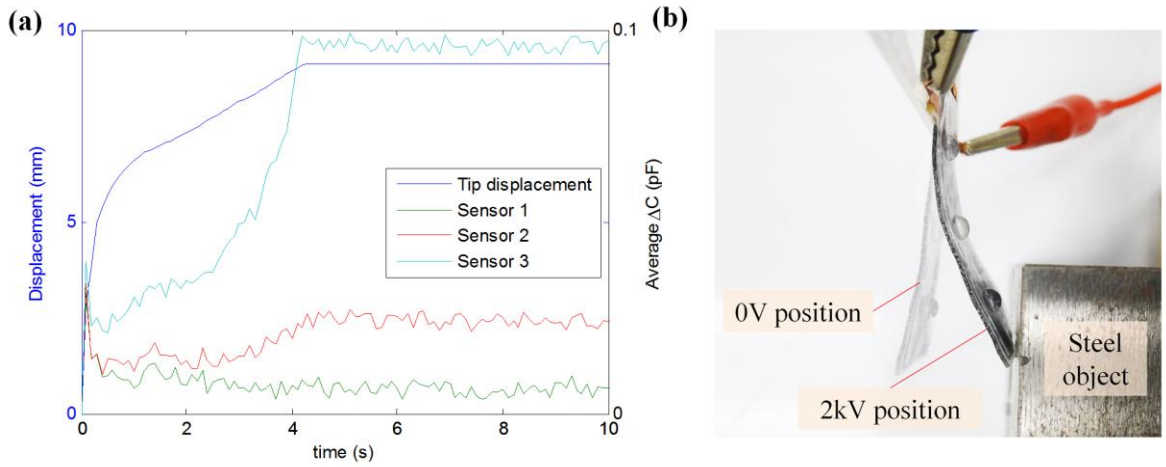

Figure 69. Simultaneous actuation and proximity sensing of TSDEA.

5.1.6 Discussion

A 3D tactile force sensing DES array was successfully fabricated using a robotic dispenser. The sensor's ability to discriminate between normal and shear forces was demonstrated, with error typically less than 15%. Additionally, proximity sensing is possible due to capacitive coupling with nearby objects. To avoid interference with force measurement, the capacitance change observed due to capacitive coupling could be subtracted by differential measurement. Some crosstalk between the sensors in the array was observed, especially in the sensors positioned furthest from the CDC, however the magnitude of the crosstalk was typically less than 20% of the applied load.

5.2 Artery mapper

5.2.1 Background

This chapter will detail the development of a high-resolution tactile DE sensor array, henceforth referred to as the "artery mapper." As described in Chapter 5.1, DE can be used as a tactile and proximity sensor, demonstrated by the use of a segmented tactile sensor to measure 3D force components of an impinging force at a discrete point on the sensor. However, there may be situations in which it is desirable to quantify the distribution of forces on a surface, requiring a well-distributed array of tactile sensors. One potential application requiring such distributed, high-resolution, flexible tactile sensor arrays is the case of arterial cannulation, which is the process of inserting a catheter or hypodermic needle into an artery, particularly in the case of medical intervention. Such catheters may be used for real-time monitoring of blood pressure and

mean arterial pressure or sampling of blood for analysis, and are generally inserted into the radial artery near the wrist, although other insertion points are possible. A significant challenge for a doctor or nurse attempting arterial cannulation is location of the artery, which may be obscured by a number of factors, including hypotension or depth and tortuousness of the artery. Moreover, repeated failed insertion of the catheter, besides being painful to the patient, can cause the artery to spasm, making insertion more difficult.

A popular alternative to manually locating the target artery is to use a medical ultrasound device. However, the device and required procedure have numerous challenges: ultrasounds are expensive, bulky, and must remain sterile for the procedure. As a result, ultrasounds may be shared between several operating rooms, and the process of waiting for availability, moving large equipment, and sterilization is not ideal to provide a patient with immediate care and increases the burden on healthcare professionals.

An array of DE tactile sensors is proposed as a more convenient, less expensive means of visualizing the trajectory of a target artery. In theory, the use of DE as an artery mapper transducer material features a number of advantages; it is soft and flexible to conform to a patient's wrist, silicone-based DE and electrode material is inexpensive and can be dispensed without costly microfabrication techniques, and support electronics for capacitance measurement is readily available from off-the-shelf components and can be miniaturized to fit into a compact package.

5.2.2 Working principle

The artery mapper consists of three main components, shown in Figure 70: (i) the DE sensor array, deposited on a PDMS substrate, (ii) support electronics consisting of a capacitance-to-digital converter (CDC), multiplexers, and a microcontroller, and (iii) a display to indicate the location of the artery. The overall operation of the device follows thusly:

1. Pulsatile force from the artery causes deformation of an element of the DE sensor array, which is in contact with the patient above the presumed artery location.
2. Deformation of the DE sensor array is measured as a capacitance change by the support electronics.

3. Display indicates locations of greatest capacitance change, as indicated by color change, etc.

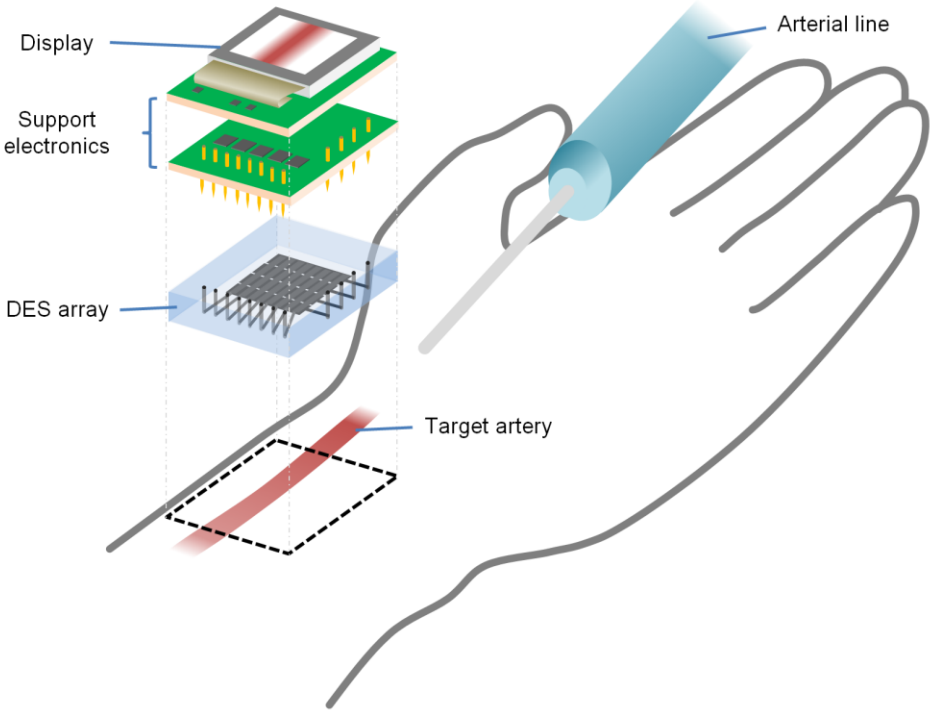

Figure 70. Exploded diagram of artery mapper showing main components and placement over target artery, with typical insertion positioning of arterial line.

5.2.3 DE sensor array

The artery mapper DES uses a perpendicular grid of sense electrodes and ground electrodes (Figure 71), unlike the configuration used in Chapter 5.1 of a common ground and discrete sense electrodes. The latter configuration requires a prohibitive number of electrical connections, as an "$m \times n$" array of sensors requires $m{\cdot}n{+}1$ electrical connections (one ground plane, plus $m{\cdot}n$ sense electrodes), and accessing the sensors in the interior of the array becomes increasingly difficult. The grid configuration is particularly advantageous for large arrays, since only $m + n$ electrical connections are required (m sense electrodes, and n ground electrodes). Moreover, there is no difficulty in accessing sensor in the interior of the array, as the electrical connections of the grid are terminated at its periphery. In this scheme, any sensor in the array (for instance, sensor (i, j) can be addressed by connecting the appropriate row and column to the capacitance input and ground of the CDC. There are additional considerations for properly addressing each sensor while minimizing parasitic capacitances, as will be discussed later.

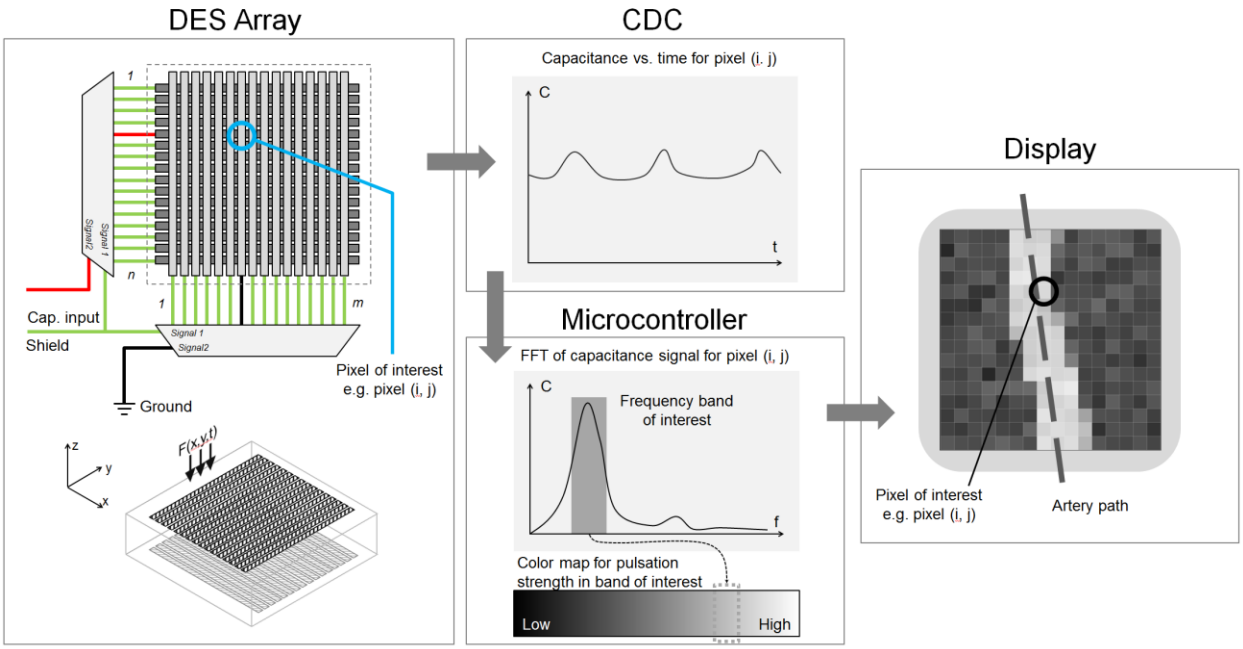

Figure 71. Flowchart showing artery mapper operation, configuration of DES array, signal processing, and display as visual aid for arterial line insertion.

One considerable difficulty of developing soft sensors in general is establishing reliable connections with traditional hard electronics composed of copper, fiberglass, etc. In the sensor shown in Chapter 5.1, the soft electrical terminals of the sensor are manually bonded to relatively rigid copper wire, which provides a fragile connection. Such a bonding method would not be likely to survive in an application with repeated strain. Moreover, replacing the sensor is impossible without de-soldering and re-soldering the copper joints, or adding an intermediate connector, which would increase its bulk and complexity. Instead, the artery mapper establishes connection to its support electronics using a pin-via connection. Vias are formed by cutting holes through the thickness of a PDMS substrate and filling with conductive material. Connection to a substrate is done by penetrating the via with a conductive pin; contact between the conductive material and pin is sufficient to establish contact, and compressive stress produced by penetration of the pin anchors the sensor in place.

5.2.4 Support electronics and signal processing

The circuitry required to measure the capacitance of each sensor of the DES array is shown in Figure 71, consisting of a CDC and one or more SPDT (single-pole dual-throw) analog multiplexers, and a microcontroller. The CDC measures capacitance between a number of

internally or externally multiplexed capacitive input channels and electrical ground. To address sensor *(i, j)* as shown in Figure 71, the multiplexers are configured such that the capacitive input is connected to row *i*, and only column *j* is grounded. In this case, the only capacitance change observed will be due to the deformation of sensor *(i, j)*. The microcontroller is used to configure and collect data from the CDC, configure the multiplexers, and also drive the display.

Since the rows (capacitance input, 2.5 kHz, 2.4 V_{pp}) and columns (grounded, 0 V) are held at different potentials, it is possible that parasitic capacitance between each of the rows and columns can affect capacitance measurement. In practice, this is observed as crosstalk between the columns of the array. To reduce parasitic capacitances, the unused rows and columns are excited by a shield signal having the same waveform as the capacitance input excitation; therefore there is no current between them and the capacitance input and the charge transfer (and thus capacitance measurement) is unaffected. Among the columns, switching between ground and the shield signal is handled by an SPDT multiplexer. Among the rows, switching between capacitive input and shield signal is handled either internally by the CDC, or externally by a separate SPDT multiplexer, depending on the required number of rows. For instance, the internal multiplexers of the CDC used in this work (TI FDC1004) support four channels of capacitive input; additional channels require an additional multiplexer.

Once the sensor is placed on the presumed artery location, the support electronics operate as follows to map the target artery:

1. Multiplexers address sensor *(1,1)*, by connecting capacitive input to row *1* and all other rows to shield signal, and connecting ground to column *1* and all other columns to shield signal.
2. CDC measures k continuous samples, stored in vector C, where $k = 2^n$. The time data C is pre-processed by a 10-point moving average, removing DC offset and linear drift, and applying a Hann window function before applying a Fast Fourier Transform (FFT) to determine the frequency content of the signal. The number of samples k is chosen such that given the CDC sampling frequency f_s, the frequency resolution of the FFT df is less than the expected fundamental frequency of the signal, 1 Hz (60 BPM) ($df = f_s / k$).

3. The sum of the FFT bins at the fundamental frequency (expected to be the heart rate of the patient) and first *m* harmonics is mapped to a color value, which is displayed corresponding to the sensor location on the display.
4. Steps 1-3 are repeated, cycling through the rows and columns until all sensors have been evaluated.

The support electronics facilitate the scanning of a 4 x 8 array and consist of a Texas Instruments FDC1004 capacitance-to-digital converter, using the internal multiplexer to route four capacitive input channels (rows). Eight ground connections (columns) are facilitated by eight TI SN74LVC1G3157 SPDT analog switches. The microcontroller used was an Atmel ATmega32u4, driving a Solomon Systec SSD1331 96 x 64 OLED display. The sampling rate of the CDC is set to approximately 85 Hz and the entire 4 x 8 array can be scanned at approximately 2.65 Hz. Schematic drawings and PCB layouts for the support electronics are shown in Appendix B.

5.2.5 Fabrication

PDMS (Sylgard 184, Dow Corning Corporation) was used as the substrate for the artery mapper DES. A 5:1 ratio of PDMS to crosslinking agent was mixed in a centrifugal mixer (Thinky Corp.) for 5 minutes to remove air bubbles. 3.75g of the mixed PDMS solution was poured into 40 mm plastic petri dishes, to produce 3 mm thick PDMS discs. Heat curing was performed in an oven at 100°C for 35 minutes, then reducing the temperature to 60°C for 72 hours to allow all volatiles, including cross-linking agent, to evaporate. Cured PDMS discs were removed from the petri dishes and cut to 25 mm x 25 mm squares.

The bottom of the PDMS substrate (the side in contact with petri dish during curing) was treated by plasma etching for 180 seconds (Sakigake YHS-R) to improve adhesion via double-sided tape to the glass dispenser substrate during drilling and later deposition processes. Holes were drilled in the substrate by a sharpened 23 gauge (0.40 mm) needle. Removal of hole debris was done by tweezers or pressurized air, and the holes were further cleaned by a stream of ethanol. The top surface and inside of the holes were treated by plasma etching for 180 seconds to improve adhesion of the conductive via material to the hole walls. The holes were filled with a 2:1 by weight mixture of silicone emulsion polymer (KM2002-L-1, Shin Etsu Corporation) and 4 wt% aqueous carbon nanotube solution (Nanocyl S.A.) using a 30 gauge (0.15 mm) needle

pressurized to 9 kPa. The vias were dried for 1 hour at 60°C. Vias after drilling and filling are shown in Figure 72.

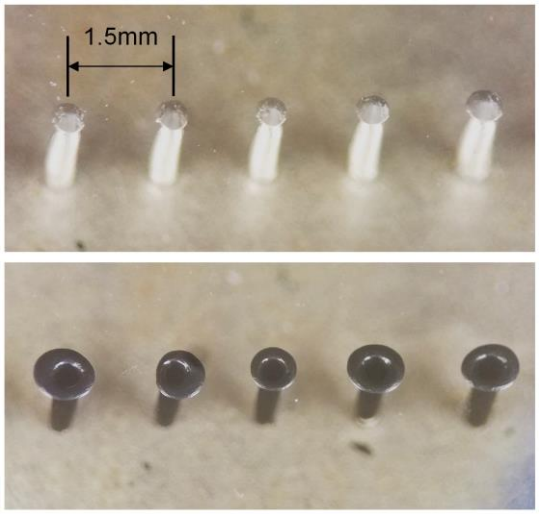

Figure 72. Vias after drilling and cleaning (top) and filling with conductive material (bottom)

A DES array consisting of 32 sensors arranged in a 4 x 8 grid (shown in Figure 73) was fabricated using a 3-axis robot and pneumatic dispenser. The array active area is 7.6 mm x 7.55 mm. The rows and columns form rectangular sensors, with active areas measuring 0.60 mm x 1.55 mm, with horizontal and vertical pitch of 1 mm and 2 mm, respectively. The rectangular sensors take advantage of the fact that higher resolution is generally needed perpendicular to the target artery and not parallel to it, as its path can usually be predicted by the proceduralist – larger pixels allow for greater coverage of the target area, and sensitivity of capacitive tactile sensors increases proportional to their area.

The sensor array was deposited on the PDMS substrate in four layers, using the process illustrated in Figure 74. Once the drying of the vias was complete, four horizontal electrode "rows" and their associated traces were deposited, followed by the dielectric elastomer layer, eight vertical rows and their associated traces, and finally a protective cover layer consisting of dielectric elastomer. The dielectric elastomer was silicone emulsion polymer (KM2002L-1, Shin Etsu Corporation), and the electrode material was 1:1 by weight mixture of silicone emulsion polymer (KM2002-L-1, Shin Etsu Corporation) and 4 wt% aqueous carbon nanotube solution (Nanocyl S.A.). Following the deposition process, the sensor array was dried at 60°C for 1 hour.

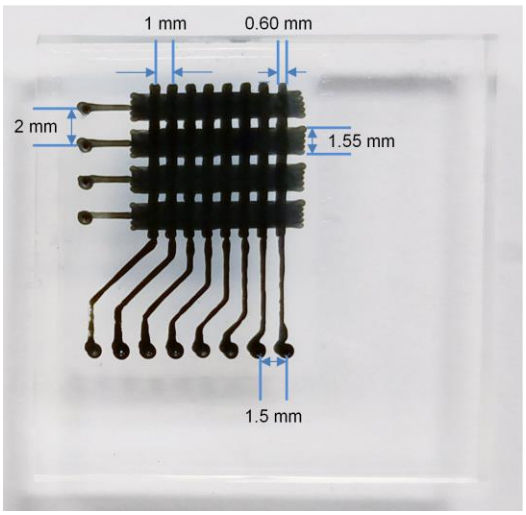

Figure 73. Completed 8 x 4 DE sensor array, with annotated dimensions.

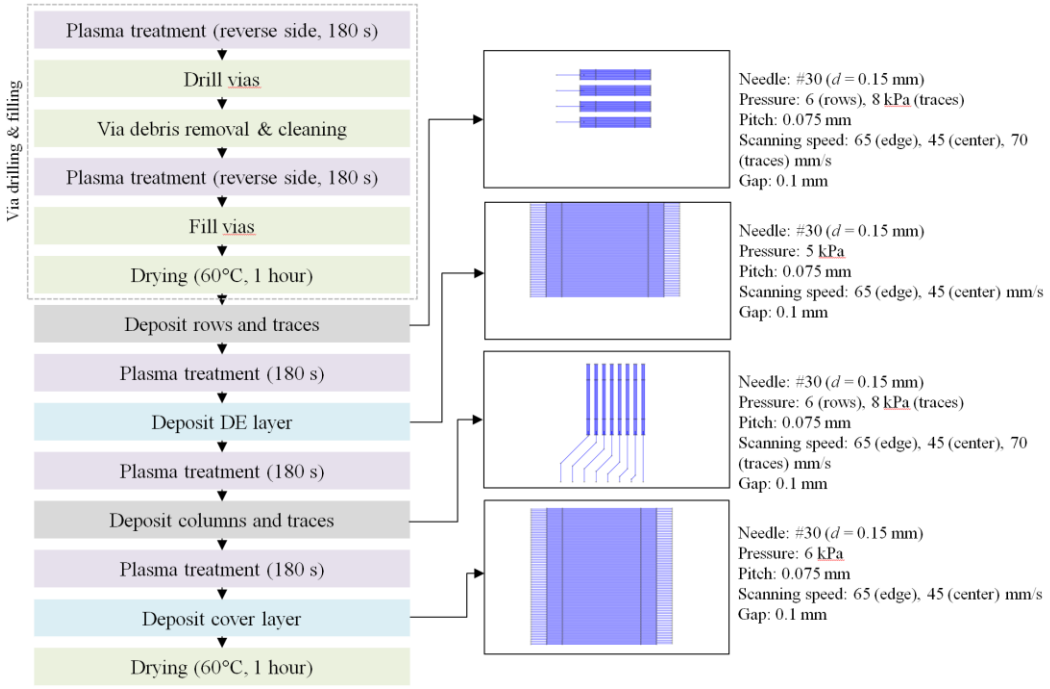

Figure 74. Fabrication scheme for 8 x 5 DE sensor array.

5.2.6 Experimental results

Incremental static loads ranging from 0.1 N to 4 N (16 kPa to 1.2 MPa) were applied to the DES array using a force gauge (Imada DS-1) and manual linear stage. The force gauge makes contact with the DES array via a 2.5 x 2.5 mm square PDMS indenter. Loading was applied in nine locations with the indenter positioned such that it covered four adjacent sensor elements, for instance in the northwest quadrant the indenter is placed over sensors *(1,1)*, *(1,2)*, *(2,1)*, *(2,2)*. An excerpt of the sensor output at the two loading extremes is shown in Figure 75, and the sensor

sensitivity is tabulated in Table 20. Complete sensor output from each force increment is included in Appendix C.

Throughout the range of applied loads, the area under loading is clearly discernible from the remainder of the array, as the maximum capacitance change consistently occurs in the sensors directly under the indenter. Sensitivity varies by as much as 14.8% over the surface of the array, tending to decrease in the west-to-east direction. Variation in sensitivity occurs because of variations in the electroded area or thickness of the dielectric layer. In this case it is likely that the PDMS substrate did not have homogeneous thickness; varying tip-to-substrate distance affected the amount of dielectric elastomer material deposited over the array. Some crosstalk appears to visible along the rows of the array. Although some "mechanical crosstalk" is expected because of the deformation field, the rows containing loaded sensors exhibit a higher capacitance change than neighboring rows, even distant from the load (for instance comparing sensors *(3,1)* and *(2,1)* in the SE quadrant of the 4 N test, Figure 75). In the 4 N test, it was observed that sensors in a loaded row distant from the load exhibited 8.7 ± 2.1% greater capacitance change (as a percentage of the peak capacitance change observed) compared to a neighboring non-loaded row. This crosstalk effect is possibly due to parasitic capacitive coupling to the force gauge, through the indenter, and could potentially be reduced by adding a shielding layer to the surface of the array. In comparison to the 3D tactile force sensor presented in Chapter 5.1, the shielding layer was omitted to reduce complexity, and because interference from high voltage was not expected in this application.

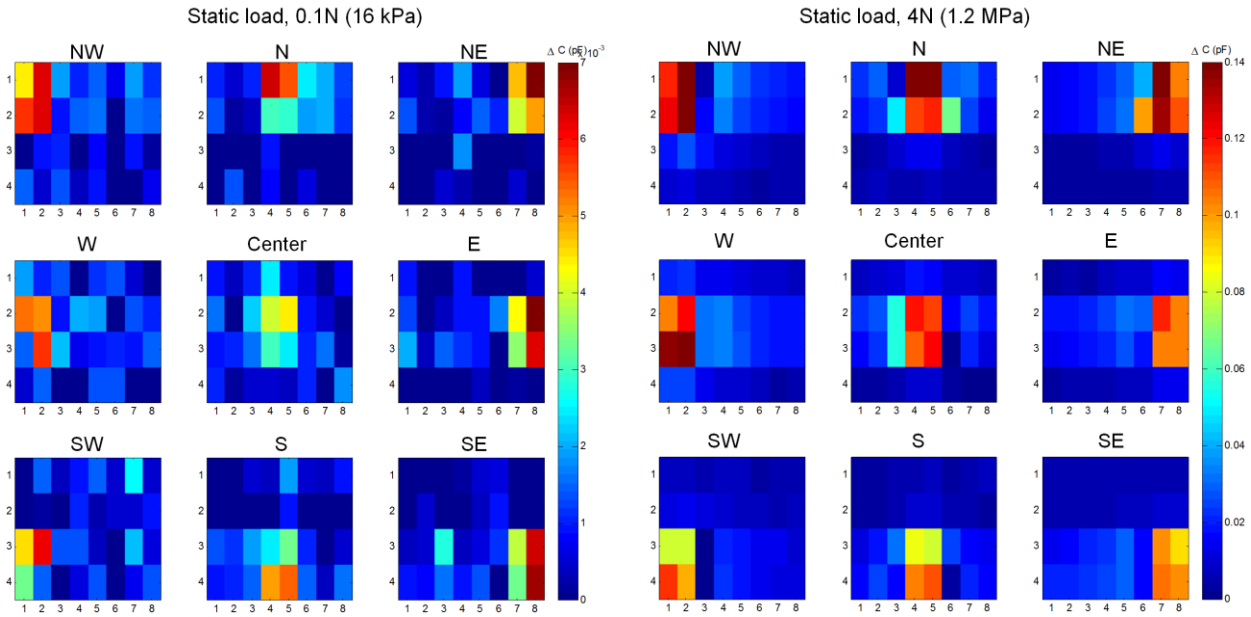

Figure 75. Capacitance change of DE sensor array under various static load magnitude and locations, visualized by color map from blue (lowest ΔC) to red (greatest ΔC)

Table 20. Force sensitivity over sensor surface.

Sensitivity [pF/N, (pF/MPa)]					
NW	0.0322 (0.201)	**N**	0.0314 (0.196)	**NE**	0.0247 (0.154)
W	0.0321 (0.201)	**Center**	0.0286 (0.179)	**E**	0.0268 (0.168)
SW	0.0286 (0.179)	**S**	0.0269 (0.168)	**SE**	0.0294 (0.184)
Mean	0.0290 (0.181)		**S.D.**	0.0024 (0.015)	

Cyclic loading was applied to the DES array to simulate the dynamic load caused by a target artery. To estimate the arterial force exerted on the sensor, a force gauge was positioned approximately above the radial artery on the wrist of a healthy volunteer. An excerpt of the resulting force measurement is shown in Figure 76, indicating a 0.1 N (14.1 kPa) fluctuating load, when a 1.45 N preload force is applied.

A range of fluctuating stresses were applied to the DES array using a 3-axis robot (Musashi Engineering SHOTminiΩ_x) and load cell (Imada FGV-1XY), with stresses above and below the

previously measured stress to simulate individuals with higher or lower pulse pressure. Fluctuating stresses with amplitudes in increasing increments of approximately 7 kPa were applied to sensor *(1,1)*, with frequency between 1 and 2 Hz (precise control of frequency was not possible due to limited speed resolution of the robot). The measured force and capacitance waveforms are shown in Figure 77.

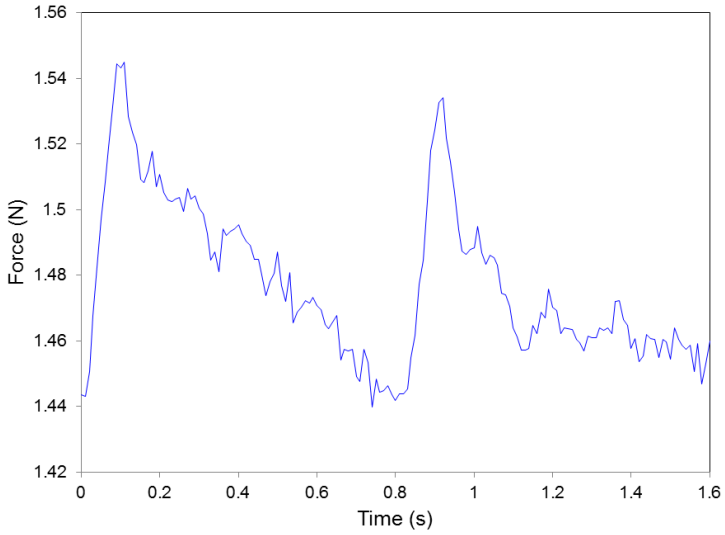

Figure 76. Force measured at radial artery by force gauge.

The results in Figure 77 indicate that the DES array is capable of measuring fluctuating stresses on the same order of magnitude of that of the radial artery. The minimum fluctuating stress (7.74 kPa) that could be applied was limited by the repeatability of the robot; but considering the sensitivity determined in the previous section and the theoretical effective resolution of the FDC1004, the minimum resolvable stress is as low as 2.8 kPa.

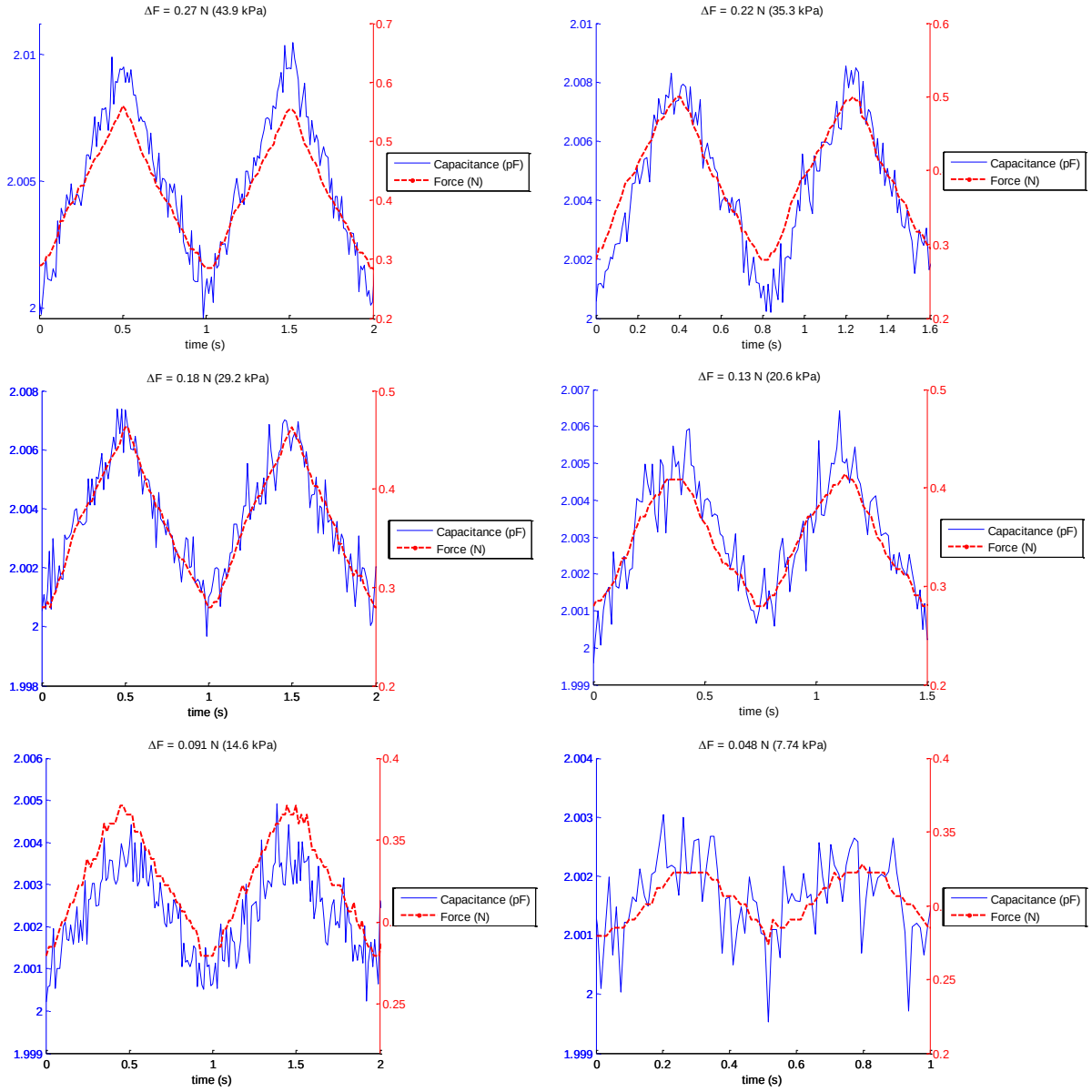

Figure 77. Response of DE sensor under various dynamic loads.

The DES array was placed on a volunteer's wrist above the radial artery to measure its response. Due to the prohibitive size of the artery mapper prototype's driving electronics, it was not possible to scan the full array. Instead, only four adjacent sensors were connected to the CDC, covering a 4 x 1 mm area. The DES array and CDC were placed on the volunteer's wrist such that Sensor 1 was placed directly over the path of the radial artery (Figure 78). The sensor outputs were recorded at six locations over the volunteer's wrist, shifting the DES array approximately 2.5 mm medially in increments of 0.5 mm. No additional preload was used to secure the array against the wrist, besides its own weight (approximately 0.1 N). For each sensor,

256 samples were recorded at 85 Hz, followed by removal of DC bias and linear trends by MATLAB's *detrend()* function and finally the FFT of each sensor's output was calculated.

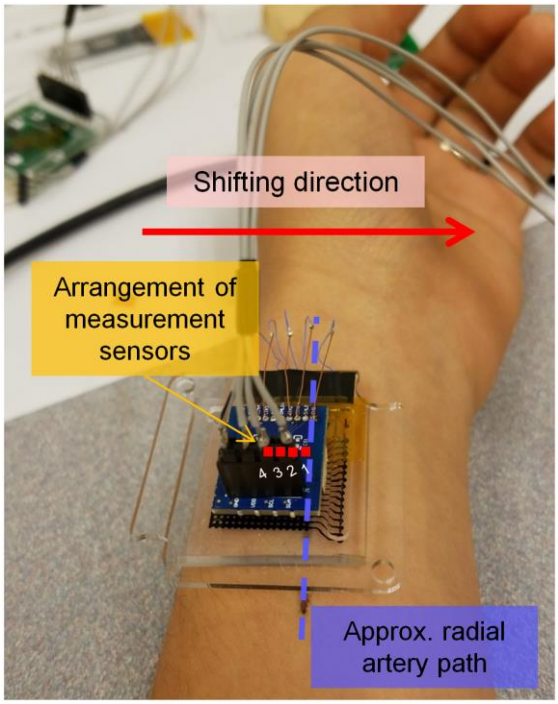

Figure 78. Placement of DES array and CDC on volunteer's wrist above radial artery.

The output of the array when located at Position 1 is shown in Figure 79. The sensor waveforms are qualitatively similar to the arterial force measured by the force gauge in Figure 76, featuring the same sawtooth-like wave appearance. The frequency of the waveform is equal to the volunteer's resting heart rate, 1.4 Hz (86 BPM). Accordingly, the FFT bin with the largest value was centered at 1.33 Hz, for all four sensors. The value of the bin likewise corresponded to the distance from the artery, the maximum value occurs at Sensor 1 and decreases monotonically. As the array is repositioned medially, the peak value occurs on different sensors, shifting from Sensor 1, to 2, and finally 3 as shown in Figure 80. Another effect observed is that the signal strength gradually decreases as the array is repositioned, particularly at Positions 4-6. This could be related to the curvature of the wrist or protruding tendons (i.e. flexor carpi radialis, palmaris longus) preventing contact between skin and the array surface.

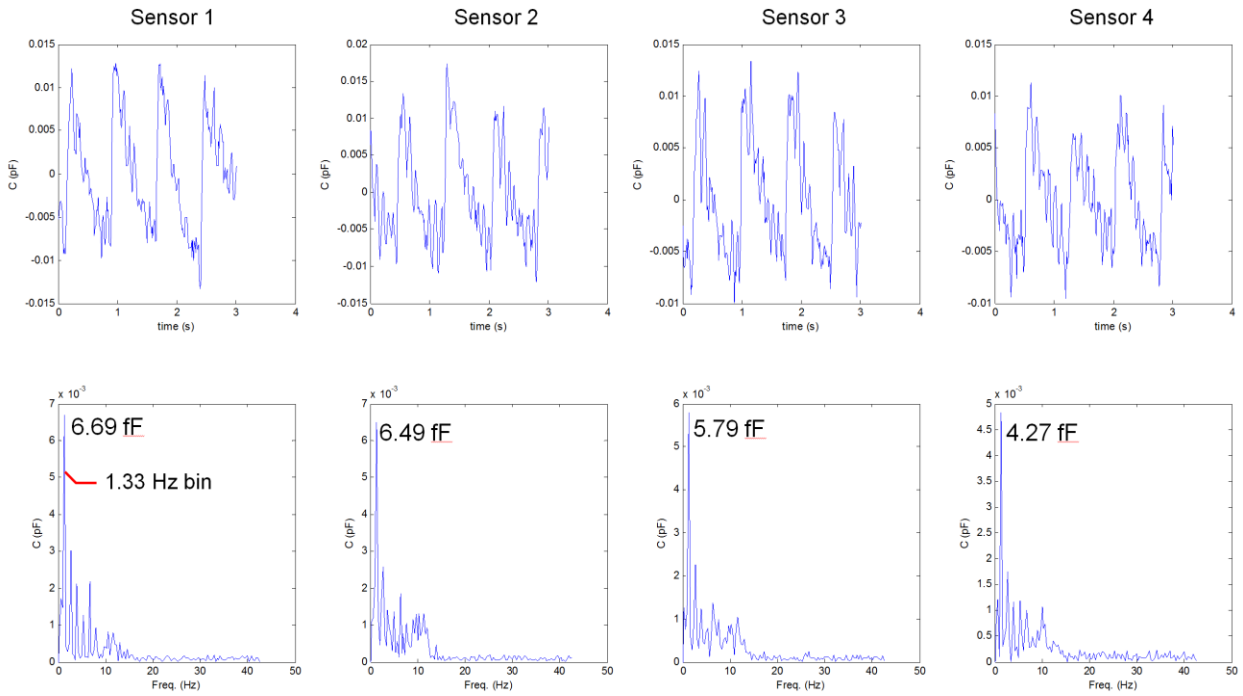

Figure 79. Sensor response and corresponding FFT at Position 1.

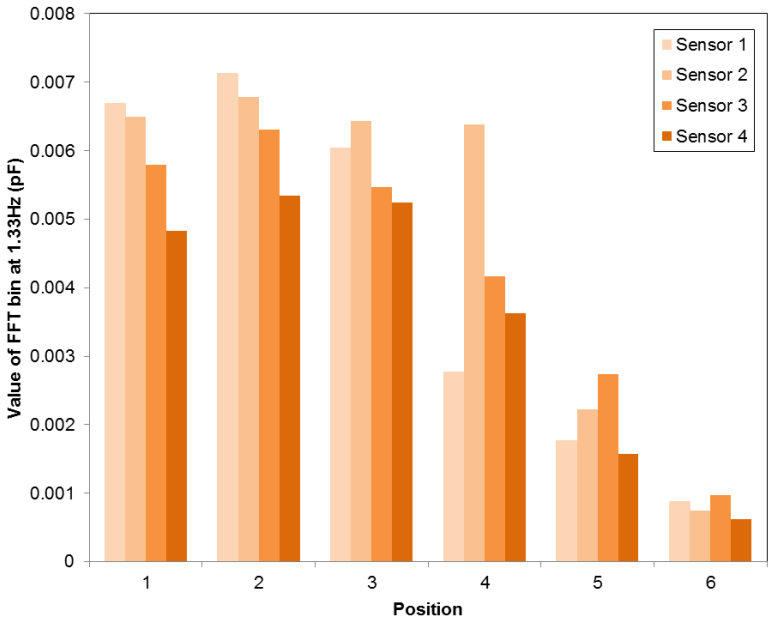

Figure 80. FFT values at 1.33 Hz as DES array is moved medially over radial artery.

The artery mapper was placed on a volunteer's wrist above the radial artery, in three orientations as shown in Figure 81, with the columns of the array approximately parallel to the radial artery, and rotated approximately 45 degrees clockwise and counterclockwise. Before placing the artery mapper, the approximate path of the radial artery was determined manually and marked on the

volunteer's skin. This path is superimposed, along with the approximate placement of these sensor array. In this test, the array geometry differed slightly from the sensor shown in Figure 73 namely that the sensor pitch along the rows was changed from 1.5 mm to 1 mm. The artery was mapped using the scheme shown in Figure 71 and detailed in Section 5.2.4. The MATLAB script and Arduino firmware used to implement this method are shown in Appendix E and F. Output from the artery mapper in the three orientations is visualized in Figure 81. It is noted that in this figure, the maximum and minimum values of the colormap, corresponding to green and blue respectively, were calculated separately for each row of the array in order to more clearly indicate the artery position, as signal magnitude tended to vary strongly across each row, possibly due to differing degrees of capacitive coupling between the volunteer's skin and the capacitance input channel connected to each row of the array. Overall, patterns corresponding to the known position of the artery are discernible by observing the sensor output in Figure 81.

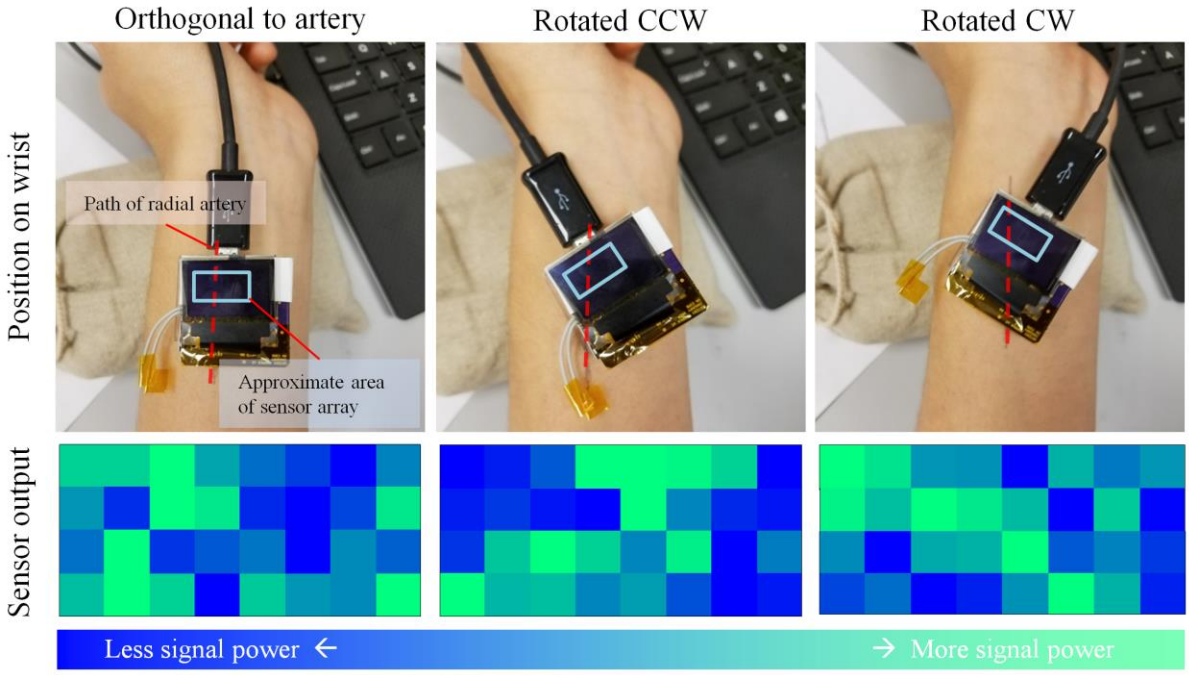

Figure 81. Orientation and output of artery mapper for mapping of radial artery.

5.2.7 Discussion

The concept of an artery mapper utilizing a DES array was presented as an alternative means of artery location for the process of arterial cannulation. A DES array consisting of 32 sensors was fabricated using a robotic dispenser, and shown to be capable of detecting the fluctuating stresses

produced by a target artery. Moreover, the location of the artery corresponded to the magnitude of the FFT of the sensor data at the fundamental excitation frequency.

In addition to its use in an artery mapper, the DES array shown in this section exemplifies the ability to use dielectric elastomers as high sensitivity and high resolution tactile sensors, featuring flexibility, low cost, and a relatively simple fabrication scheme. Although the array size and resolution were somewhat limited in order to meet the requirements (low cost, compact size), the upper limits of sensor count and pitch are mostly limited by the supporting electronics; as the array size increases so does the number of channels switched by the supporting electronics – which was beyond the scope of this work.

Demonstration of the artery mapper shows promise for the use of dielectric elastomer sensor arrays in point-of-care medical devices. However, a significant body of work remains to be done before employing the device in a clinical setting. The device was demonstrated on a healthy individual, whereas the target population may suffer from hypotension or deep and tortuous arteries which make the detection of faint pressure fluctuation from the wrist more difficult – thus testing on a diverse range of subjects is necessary.

5.3 Conclusions

The 3D tactile force sensor demonstrated in this chapter demonstrated the ability to simultaneously measure and discriminate shear and normal forces, without the fragility and cost of similar actuators presented in other works [2] [34]. Moreover, since it utilizes materials and a fabrication method consistent with the construction of DEA, it is easily integrated into a sensor-actuator unit. The sensitivity, spatial resolution, and active area of a DES array with grid configuration was shown to be suitable for measuring the pulse and locating a target artery in a human subject. Such DES arrays are capable of measuring force distributions over their surface, and show promise for expansion into arrays of greater size and spatial acuity.

6. Conclusions and recommendations

6.1 Conclusions

6.1.1 Fabrication of dielectric elastomer actuators

Dielectric elastomers (DE) are a soft electroactive material which can be used as flexible actuator devices. This work explored the use of a robotic dispenser system to deposit thin (tens of μm) elastomer films without the need for secondary processes such as trimming or masking found in more typical practices such as spray or roll coating. To our knowledge, this is the first demonstrated use of a robotic dispenser to fabricate DEA. Successful fabrication of multilayer unimorph dielectric elastomer actuators (DEA) consisting of 2, 4, 6, 8, and 10 DE layers with target DE thickness of 10 μm was demonstrated. To improve the performance of the actuator, PVDF terpolymer with high dielectric constant, and silicone emulsion polymer/MWCNT composite with good conductivity and low stiffness was used. Depending on configuration, the actuators exhibited tip displacement of several millimeters, and blocking force up to 20 mN at 500V. Compared to other multilayer unimorph DEA shown in other works, the dispenser-fabricated DEA exhibited vastly improved blocking force performance per kV. Repeatability of the process was also characterized, with standard deviation of tip displacement and blocking force of less than 10% and 15% of the mean value at 120 seconds, among all samples tested.

6.1.2 Modeling of dielectric elastomer actuators

Elastic and viscoelastic models were developed to predict the behavior of multilayer unimorph DEA. The elastic model is based on Euler-Bernoulli beam theory with electromechanical coupling via the Maxwell stress equation, and is an expansion on works done by previous researchers on piezoelectric laminates. The viscoelastic model follows from the elastic model, using the elastic-viscoelastic correspondence principle to predict time-dependent behavior, which is important as all actuators tested did not exhibit steady-state behavior after 120 seconds of deformation. Viscoelastic behavior of DEA materials was determined by stress relaxation tests and curve fitting by Prony series. Both models agreed well with experimental data, with the viscoelastic model remaining within 1 standard deviation of the mean of the experimental data throughout most of the deformation. The model tends to over predict both deformation and blocking force immediately after and until approximately 1-2 seconds after deformation, by as much as 78%. However, this disparity is explained by rapid abatement of widthwise curvature

during the initial stages of deformation, since the model assumes that the actuator remains flat along its width during actuation. The viscoelastic model derived in this work represents the first analytical solution for the viscoelastic behavior of multilayer unimorph DEA.

6.1.3 Variable stiffness dielectric elastomer actuators

Although DEA can exhibit large deformations thanks to their high compliance, for the same reason it is difficult for them to support large loads. Thus, for a robotic end effector, a variable stiffness property is desirable. This work introduces the concept of using electrostatic attraction to modulate the shear strength and thus bending stiffness of laminar structures of DEA. The concept of an electrostatic variable stiffness DEA (VSDEA) was demonstrated by using an electrolaminate as the passive layer in an otherwise standard DEA, achieving a stiffness increase of nearly four-fold, over clamping voltages from 0V to 300V. Even greater performance was achieved by using a multitude of DEA units in parallel to form a VSDEA, exhibiting remarkable stiffness increase of up to 39× using clamping voltage up to 700V. A claw actuator consisting of two VSDEA were demonstrated supporting 17 times their own weight, which is greater than the figure achieved by VSDEA using phase change of low melting point alloy. Equations are presented to predict the stiffness change and shear strength of such VSDEA to reasonable agreement, although inhomogeneity in the fabrication process leads to some disagreement.

6.1.4 Dielectric elastomer sensors

Besides their use as soft actuators, dielectric elastomers are also useful as a sensing material. This work demonstrates two novel applications of dielectric elastomer sensors (DES). A tactile sensor array with a dome feature was demonstrated to resolve the components of impinging forces, envisioned as a useful device for determining contact condition between an end effector and foreign body. Although EAP sensors with a similar dome structure have been demonstrated using IPMC membranes or PDMS patterned by soft lithography techniques, the sensor in this work arguably exhibits greater durability (compared to IPMC) and ease of fabrication using the robotic dispenser. The integration of this device into a dielectric elastomer actuator was also demonstrated. The second device was a larger, denser tactile sensor array intended as the sensing component in a device used to map the location of target arteries for arterial cannulation. The sensor array exhibited the ability to distinguish the location of tactile forces with little crosstalk, and also to distinguish dynamic loads as small as 7 kPa. In testing with a human volunteer, the

sensor array was able to determine the position of the radial artery at the wrist, even after the device was repeatedly repositioned.

6.2 Recommendations for future research

Additive fabrication using a pneumatic dispenser shows promise for fabrication of high performance multilayer DEA, but some challenges remain. First is the issue of scale – the active area of the DEA demonstrated in this work was only 20 × 10 mm. Increasing the area of DEA produced by the dispenser appears to also increase the rate of failure by dielectric breakdown. This notion is intuitive; if the probability of a breakdown-causing defect over a unit area remains more or less constant, increasing the area increases the rate of failure. Thus, successful fabrication of larger actuators is contingent on reducing the rate of defects such as thickness inhomogeneity in the deposited layers. Second is the variance in deposited layer thickness between deposition sessions – it was observed that even when all deposition parameters remain constant, the amount of material dispensed in a given session tends to vary, based on changes in solution temperature or viscosity, or partial occlusion of the needle by cured material. Control of the dispenser is open loop, so the task of keeping layer thickness consistent falls to the operator and a time-consuming trial-and-error process. Third, thickness inhomogeneity – which is thought to be deleterious to the P-VSDEA stiffness change performance – occurs due to the coffee stain effect, and because the speed of the needle varies particularly at the edges of the DEA, since needle is accelerating and decelerating in these regions. For these reasons it would be advantageous to implement closed loop control, monitoring the needle speed and flow rate to modulate the deposition pressure in order to keep the deposited volume constant.

Variable stiffness DEA based on electrostatic chucking developed in this work exhibited similar stiffness change to LMPA-based devices, without some of their disadvantages, such as slow transition time, toxicity, and high power consumption. One challenge is reliability of such devices. Despite testing of the DEA units for breakdown above their actuation voltage, failure of entire P-VSDEA due to dielectric breakdown of a single unit occasionally occurs during actuation. This is thought to be because of gradual breakdown of a DE layer near a defect, which causes increased local current flow and heating, and eventual failure. Short-circuiting of a single failed DEA unit renders the entire P-VSDEA inoperable, since the electrical terminals of each unit are joined. Isolation of DEA units by built-in thermal fuses, such as sacrificial electrode

traces which degrade when excessive current is applied, could be used to produce more robust P-VSDEA, capable of operation even after failure of multiple DEA units.

Finite element analysis of the deformation of unimorph DEA using viscoelastic elements is suggested, when it is expected that the DEA will exhibit transitional behavior between primarily widthwise and lengthwise curvature during the initial stages of deformation. Although adjustment of the models presented in the present work can be done using explicit formulations, measurement of the widthwise curvature change is necessary, as the current model does not allow such predictions. That said, expenditure of strain energy to produce or remove widthwise curvature has negative effects on tip displacement of unimorph DEA. Mitigation of curvature by further annealing processes or embedding stiffening fibers along the actuator width is recommended to reduce disparity between experimental results and model predictions, and improve overall performance. In addition, it is important to note the assumptions of small-deformation beam theory and linear stress-strain behavior embedded in both the elastic and viscoelastic models. For most unimorph actuators, the strain exhibited is typically very small (and this is a very good assumption in the case of PVDF terpolymers, where the Maxwell strain is well under 1%), but for edge cases utilizing this model where extremely soft elastomers are utilized, adaptation of nonlinear stress-strain constitutive models and large deformation beam theory is suggested.

Fabrication of dielectric elastomer sensor arrays with enhanced spatial resolution and coverage is contingent on efficient routing of signal lines and compact electronics design of the multiplexing and capacitance-to-digital conversion circuitry. To this effect, it is suggested to improve integration of the soft sensor array and stiff electronics. Some work has been done to this end, particularly in the case of the artery mapper where the support electronics are populated on a rigid PCB supporting the sensor – though the compliance of the entire arrangement is thus limited; switching to a polyimide substrate may allow fabrication of a more flexible sensor array. Moreover, to reduce the non-sensing perimeter around the active array area, it would be advantageous to route the signal lines in a more three-dimensional sense, through the thickness of the array. Development of such three-dimensional circuitry is ostensibly possible using the dispenser system, though it has not yet been attempted.

6.3 Acknowledgements

I would like to express my sincere gratitude to the following parties, in no particular order:

- Professor Minoru Taya, who supported me and gave me encouragement as my advisor, and whose door was always open to discuss my questions about research and future career.
- Dr. Sheena Hembrador, the progenitor of the Artery Mapper concept, whose mentorship has been invaluable for this multidisciplinary research.
- Professor Mitsumi Kimura and Saki Takahashi of Shinshu University, for their insight in developing and testing the silicone-MWCNT electrode material utilized throughout this work.
- Professor Keishi Naito of Gifu University, whose knowledge of polymer processing was of immense help to me during his tenure as a postdoc at UW, and whose continued correspondence has been of great encouragement throughout my research.
- Hiroya Imamura of Nabtesco Corporation, for without his perseverance and hard work, the successful processing of DEA and P-VSDEA would not have been possible.
- Past and present members of CIMS, for their friendship, advice, and everything that they have taught me.
- My family, particularly my parents and my grandparents; who made it possible for me to pursue this research and encouraged me when I doubted myself. This work is dedicated to my grandmother, who taught me that knowledge and education is the best gift in life.
- My wife Keturah, whose love and never-ending patience was a cornerstone which I could always depend upon in the pursuit of this research.

This research was supported by a contract from Nabtesco Corporation to the Center for Intelligent Materials and Systems (CIMS) at University of Washington.

7. References

1. Gerbode S, Puzey J, McCormick A, Mahadevan L. How the cucumber tendril coils and overwinds. Science. 2012;(337): p. 1087-1091.

2. Wang J, Sato H, Xu C, Taya M. Bioinspired design of tatile sensors based on Flemion. Journal of Applied Physics. 2009; 105(8): p. 083515.

3. Sareh S, Jiang A, Faragasso A, Noh Y. Bio-inspired tactile sensor sleeve for surgical soft manipulators. IEEE International Conference on Robotics and Automation. 2014;: p. 1454-1459.

4. Taya M, Volkenburgh E, Mizunami M, Nomura S. Bioinspired Actuators and Sensors Cambridge: Cambridge University Press; 2016.

5. Smits JG, Choi W. The constituent equations of piezoelectric heterogeneous bimorphs. IEEE Transactions on Ultrasonics, Ferroelectrics, and Frequency Control. 1991; 38(3): p. 256-270.

6. Pelrine R, Eckerle J, Chiba S. Review of artificial muscle approaches. Proceedings of the 3rd International Symposium of Micro Machine and Human Science. 1992;: p. 1-19.

7. Kornbluh R, Pelrine R, Joseph J. Elastomeric dielectric artificial muscle actuators for small robots. Proc. of the Materials Research Society Symposium. 1995; 600: p. 119-130.

8. Pelrine R, Kornbluh R, Joseph J. Electrostriction of polymer dielectrics with compliant electrodes as a means of actuation. Sensors and Actuators A. 1998; 64: p. 77-85.

9. Pelrine R, Kornbluh R, Eckerle J, Jeuck P, Oh S, Pei Q, et al. Dielectric Elastomers: Generator Mode Fundamentals and Applications. Proc. SPIE 4329. 2001;: p. 148-156.

10. Shankar R, Ghosh T, Spontak R. Dielectric elastomers as next-generation polymeric actuators. Soft Matter. 2007; 3: p. 1116-1129.

11. Kussmaul B, Risse S, Kofod G, Wache R, Wegener M, McCarthy D, et al. Enhancement of dielectric permittivity and electromechanical response in silicone elastomers: molecular

grafting of organic dipoles to the macromolecular network. Advanced Functional Materials. 2011;(21): p. 4589-4594.

12. Bauer F, Fousson E, Zhang QM. Recent advances in highly electrostrictive P(VDF-TrFE-CFE) terpolymers. IEEE Transactions on Dielectrics and Electrical Insulation. 2006.

13. Le MQ, Capsal JF, Gallineau J, Ganet F, Yin X, Yang M, et al. All-organic electrostrictive polymer composites with low driving electrical voltages for micro-fluidic pump applications. Scientific Reports. 2015;(5): p. 11814.

14. Balakrisnan B, Smela E. Challenges in the Microfabrication of Dielectric Elastomer Actuators. Proc. SPIE 7642. 2016.

15. Araromi OA, Conn AT, Ling CS, Rossiter JM, Vaidynathan R, Burgess SC. Spray deposited multilayered dielectric elastomer actuators. Sensors and Actuators A: Physical. 2011; 167: p. 459-467.

16. Lotz P, Matysek M, Schlaak H. Fabrication and application of miniaturized dielectric elastomer stack actuators. IEEE/ASME Transactions on Mechatronics. 2011; 16(1): p. 58-66.

17. Duduta M, Wood R, Clarke D. Flexible, stretchable electroadhesives based on acrylic elastomers. Proc. SPIE 9798. 2016;(97981D).

18. Choi ST, Kwon JO, Bauer F. Multilayered relaxor ferroelectric polymer actuators for low-voltage operation fabricated with an adhesion-mediated film transfer technique. Sensors and Actuators A: Physical. 2013; 203: p. 282-290.

19. Risner J. Investigation of dielectric elastomer actuation for printable mechatronics. University of California, Berkeley, ProQuest Dissertations Publishing. 2008;(3331779).

20. Zhang R, Lochmatter P, Kunz A, Kovacs G. Spring Roll Dielectric Elastomer Actuators for a Portable Force Feedback Glove. Proc. SPIE 6168. 2006;(61681T).

21. Araromi O, Burgess S. A finite element approach for modelling multilayer unimorph

dielectric elastomer actuators with inhomogeneous layer geometry. Smart Material Structures. 2012; 21(3 032011).

22. Shintake J, Schubert B, Rosset S, Shea H. Variable stiffness actuator for soft robotics using dielectric elastomer and low-melting point alloy. IEEE/RSJ International Conference on Intelligent Robots and Systems. 2015;: p. 1097-1102.

23. Pelrine R, Kornbluh R. Variable stiffness mode dielectric elastomer devices. Advances in Science and Technology. 2008; 61: p. 192-201.

24. Shintake J, Rosset S, Schubert B, Mintchev S, Floreano D, Shea H. DEA for soft robotics: 1-gram actuator picks up a 60-gram egg. Proc. SPIE 9430. 2015.

25. Zhang J, Tang L, Lit B, Wang Y, Chen H. Modeling of the dynamic characteristic of viscoelastic dielectric elastomer actuators subject to different conditions of mechanical load. Journal of Applied Physics. 2015; 117: p. 084902.

26. Lai W. Characteristics of dielectric elastomers and fabrication of dielectric elastomer actuators for artificial muscle applications. Iowa State University Graduate Theses and Dissertations. 2011;(12183).

27. McKay T, O'Brien B, Cailus E, Anderson I. Soft generators using dielectric elastomers. Applied Physics Letters. 2011;(98).

28. O'Brien B, Thode J, Anderson I, Cailus E, Haemmerle E, Xie S. Integrated extension sensor based on resistance and voltage measurement for a dielectric elastomer. Proc. SPIE. 2007;: p. 652415.

29. Jung K, Kim KJ, Choi HR. A self-sensing dielectric elastomer actuator. Sensors and Actuators A: Physical. 2008; 143(2): p. 343-351.

30. Kim DS, Chuc NH, Jin SM, An KJ, Phuc VH, Koo J, et al. A flexible fingertip tactile sensor. Proc. SPIE. 2010;: p. 76420F.

31. Hwang DY, Kim B, Cho HJ, Li Z, Lee Y, Nam JD, et al. Development of microsized slip sensors using dielectric elastomer for incipient slippage. Proc. SPIE. 2014;: p. 906128.

32. Kim BC, Shin S, Chung J, Lee Y, Nam JD, Moon H, et al. A dual axis shear force film sensor for robotic tactile applications. Proc. SPIE. 2011;: p. 797628.

33. Tiwana M, Shashank A, Redmond S, Lovell N. Characterization of a capacitive tatile shear sensor for application in robotic and upper limb prostheses. Sensors and Actuators A: Physical. 2011;: p. 164-172.

34. Cheng MY, Lin CL, Lai YT, Yang YJ. A polymer-based capacitive sensing array for normal and shear force measurement. Sensors 10. 2010;: p. 10211-10225.

35. Rosset S, Shea H. Flexible and Stretchable Electrodes for Dielectric Elastomer Actuators. Applied Physics A. 2012.

36. Weinberg MS. Working equations for piezoelectric actuators and sensors. Journal of Microelectromechanical systems. 1999; 8(4): p. 529-533.

37. Dunsch R, Breguet JM. Unified mechanical approach to piezoelectric bender modeling. Sensors and Actuators A: Physical. 2007; 134(2): p. 436-446.

38. Loy RJ, de Hoog FR, Anderssen RS. Interconversion of Prony series for relaxation and creep. Journal of Rheology. 2015; 59(1261).

39. Ask A, Menzel A, Ristinmaa M. Modelling of viscoelastic dielectric elastomers with deformation dependent electric properties. Procedia IUTAM. 2015;(12): p. 134-144.

40. Sogard MR, Mikkelson AR, Nataraju M, Turner KT, Engelstad RL. Analysis of Coulomb and Johnsen-Rahbek electrostatic chuck performance for extreme ultraviolet lithography. Jornal of Vacuum Science & Technology B. 2007; 25(6): p. 2155.

41. Lu S, Chen X, Levard T, Diglio P, Gorny L, Rahn C, et al. Large displacement in relaxor ferroelectric terpolymer blend derived actuators using Al electrode for braille displays.

Scientific Reports. 2015; 5(11361).

42. Yip M, He D, Winokur E, Balderrama A, Sheridan R, Ma H. A flexible pressure monitoring system for pressure ulcer prevention. EMBC 2009, Annual International Conference of the IEEE. 2009;: p. 1212-1215.

Appendix A: DEA cross section micrographs

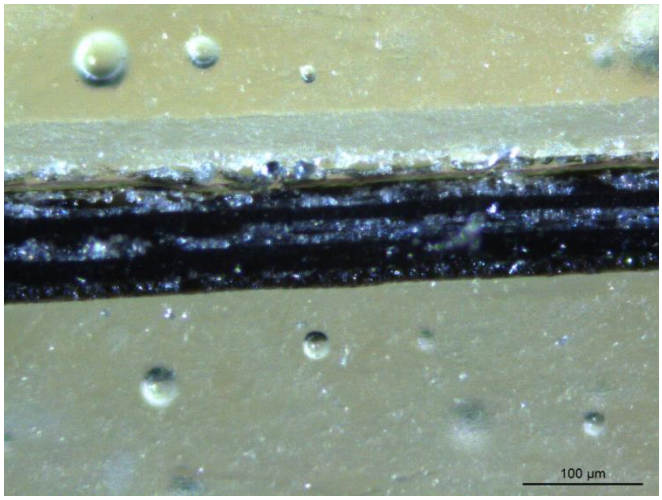

Figure A1. 200x micrograph cross section of 2 DE layer DEA.

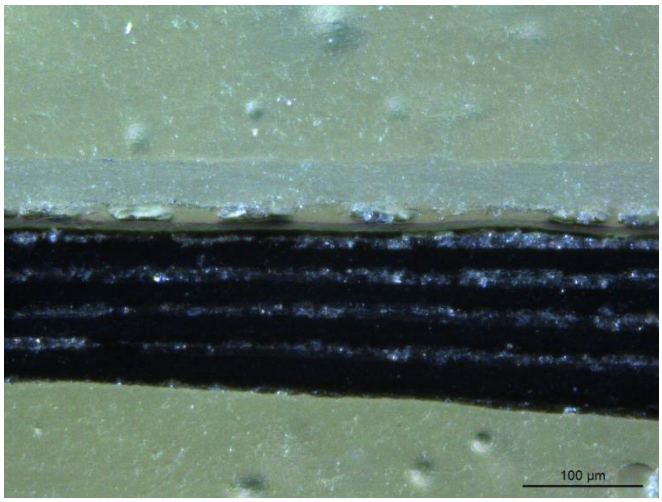

Figure A2. 200x micrograph cross section of 4 DE layer DEA.

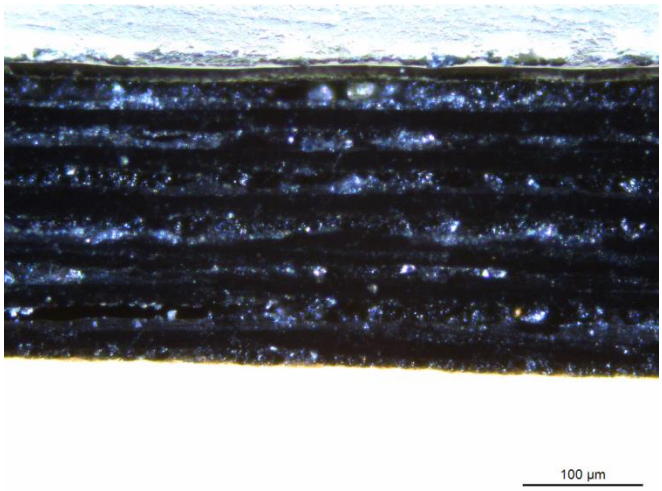

Figure A3. 200x micrograph cross section of 6 DE layer DEA.

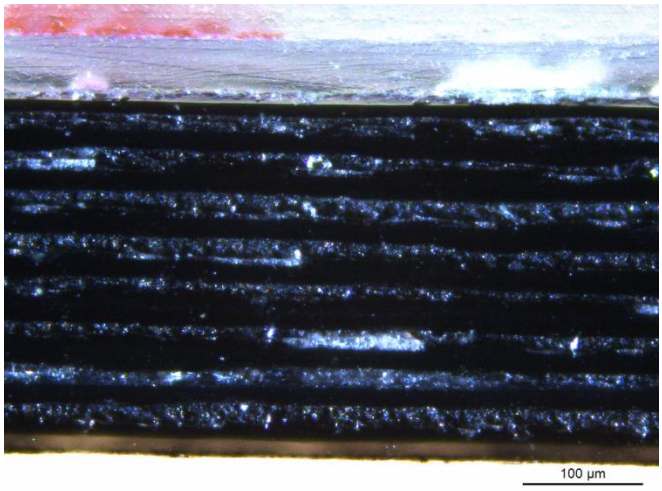

Figure A4. 200x micrograph cross section of 8 DE layer DEA.

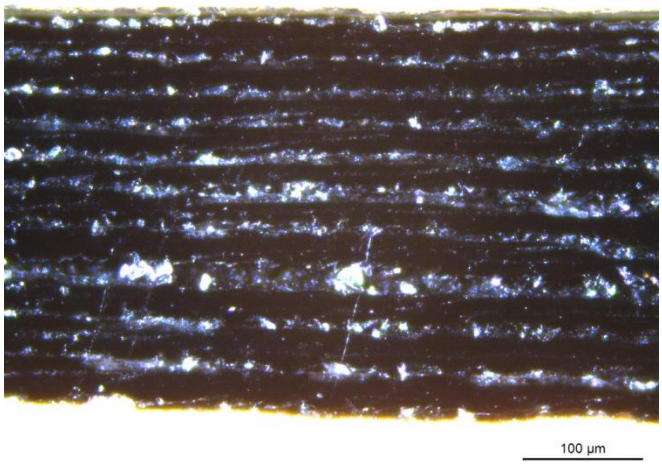

Figure A5. 200x micrograph cross section of 10 DE layer DEA.

Appendix B: Artery mapper support electronics

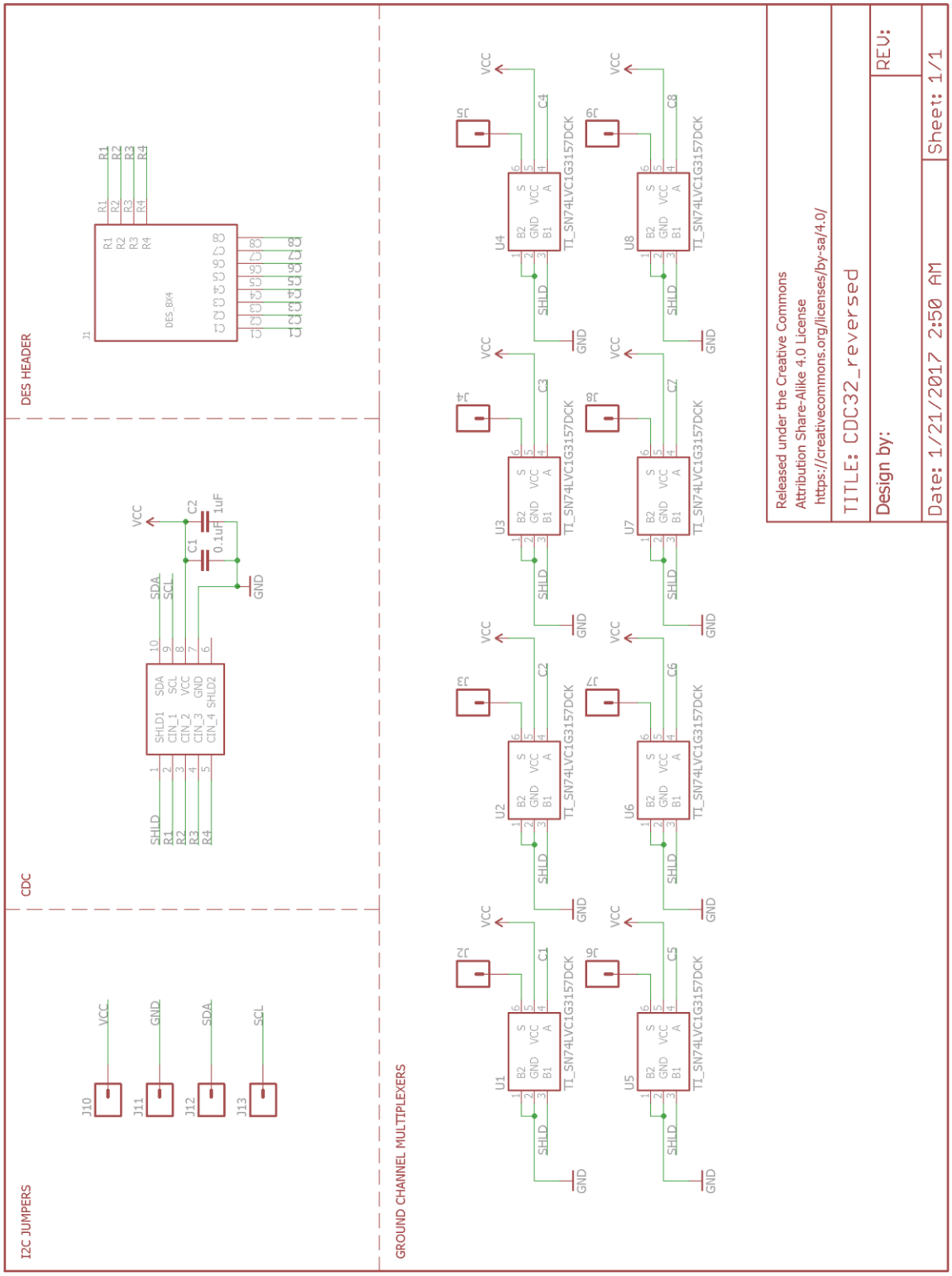

Figure B1. Schematic of CDC + MUX board.

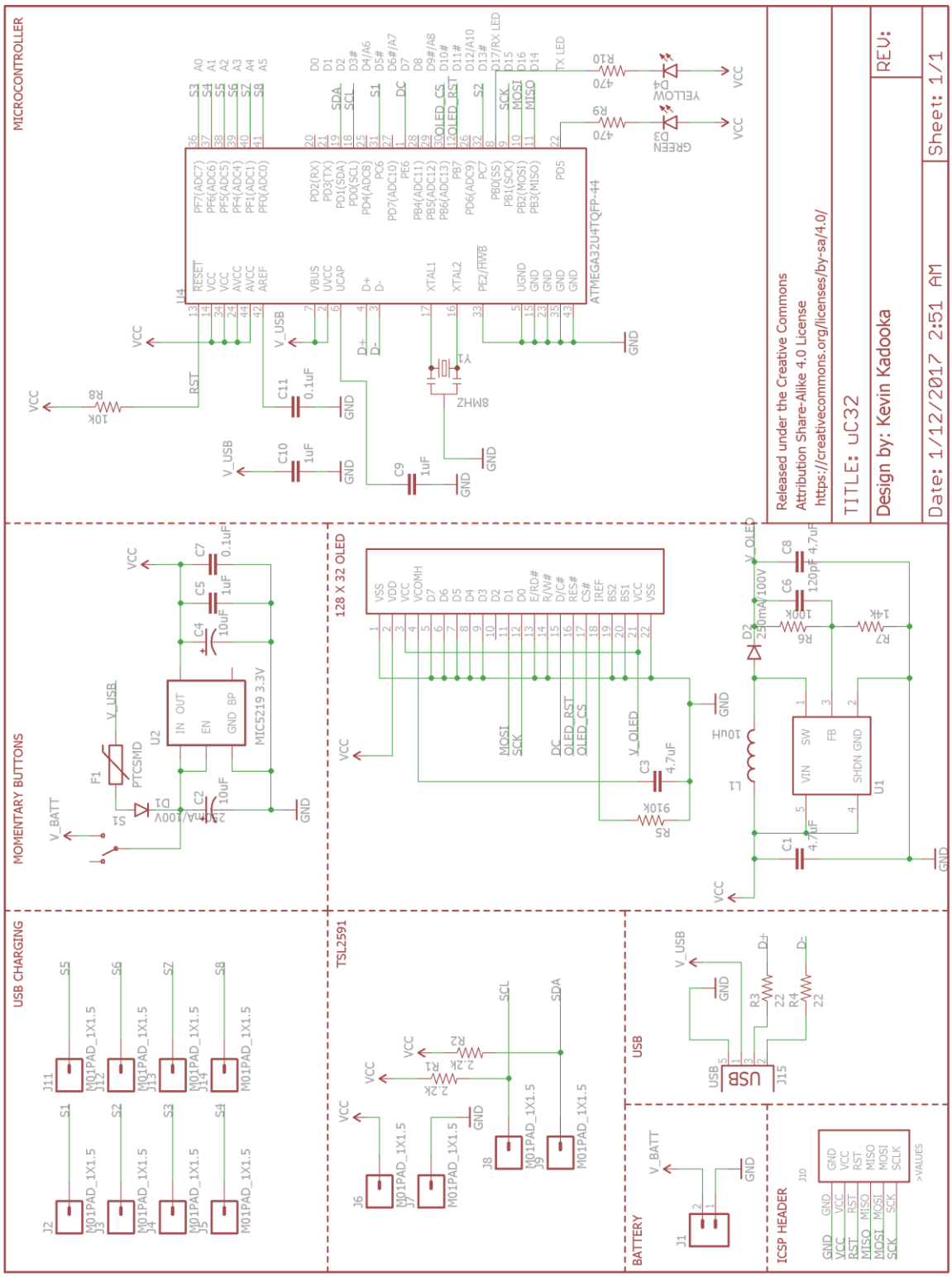

Figure B2. Schematic of uC + Display board.

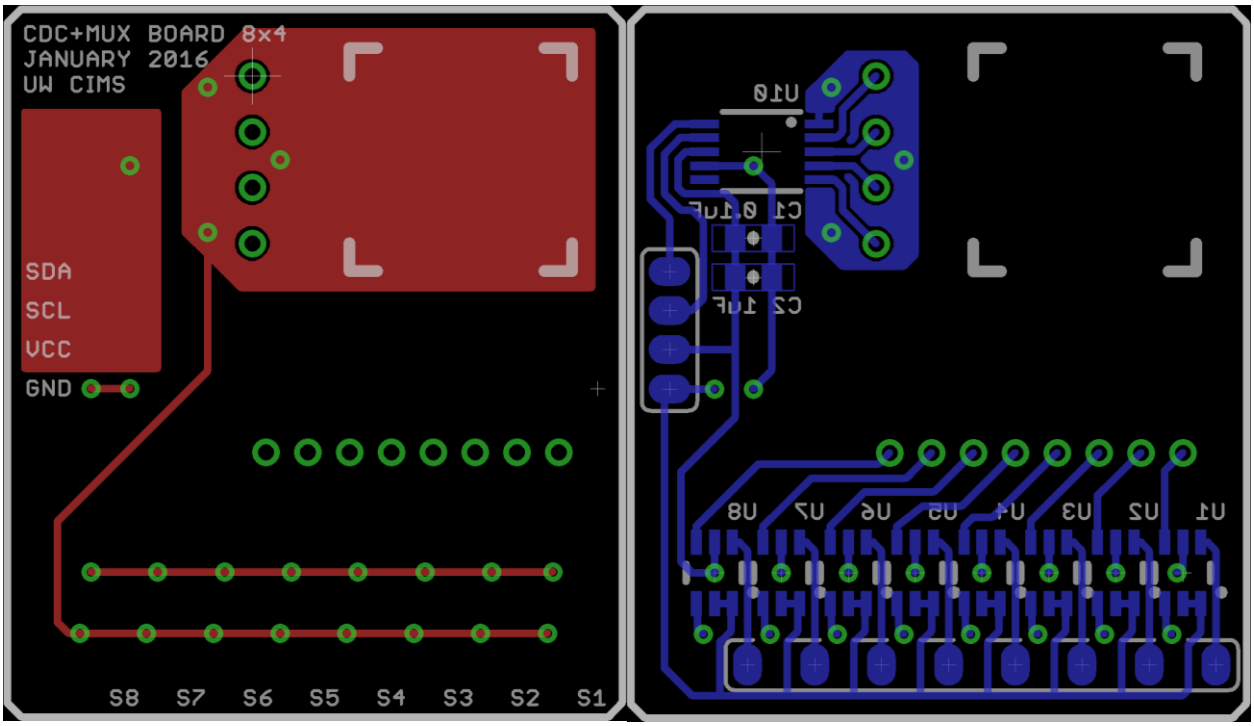

Figure B3. Board layout of CDC + MUX board, top (left) and bottom (right)

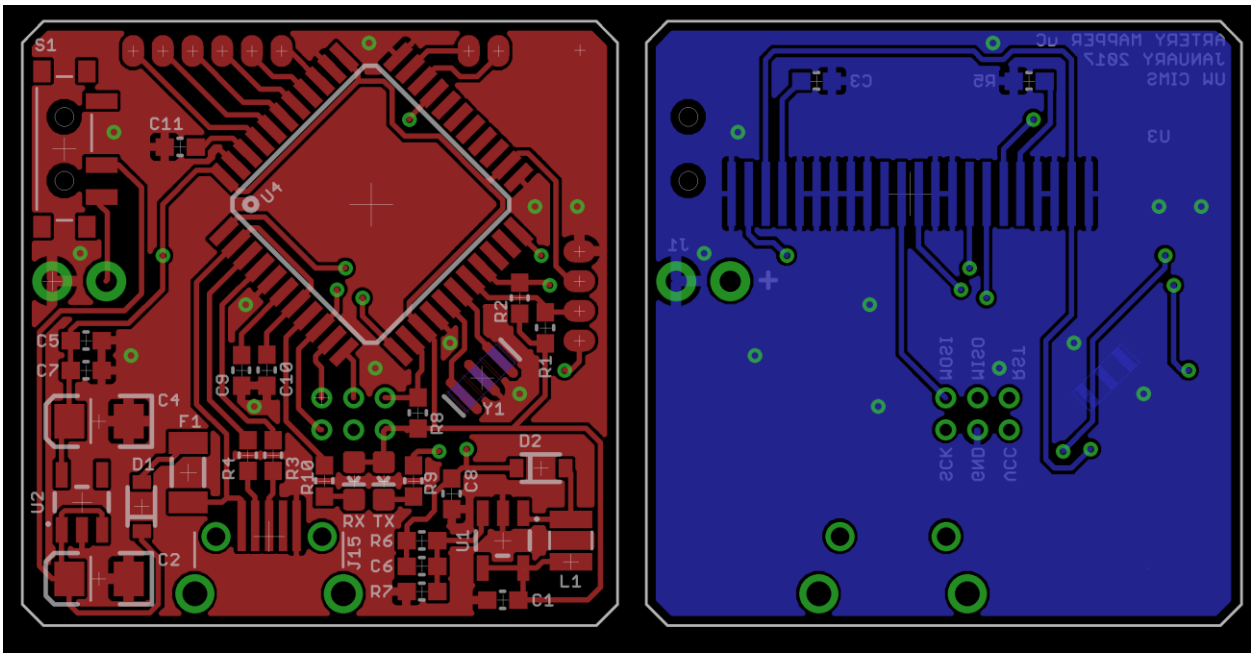

Figure B4. Board layout of uC + Display board, top (left) and bottom (right)

Appendix C: Artery mapper static test plots

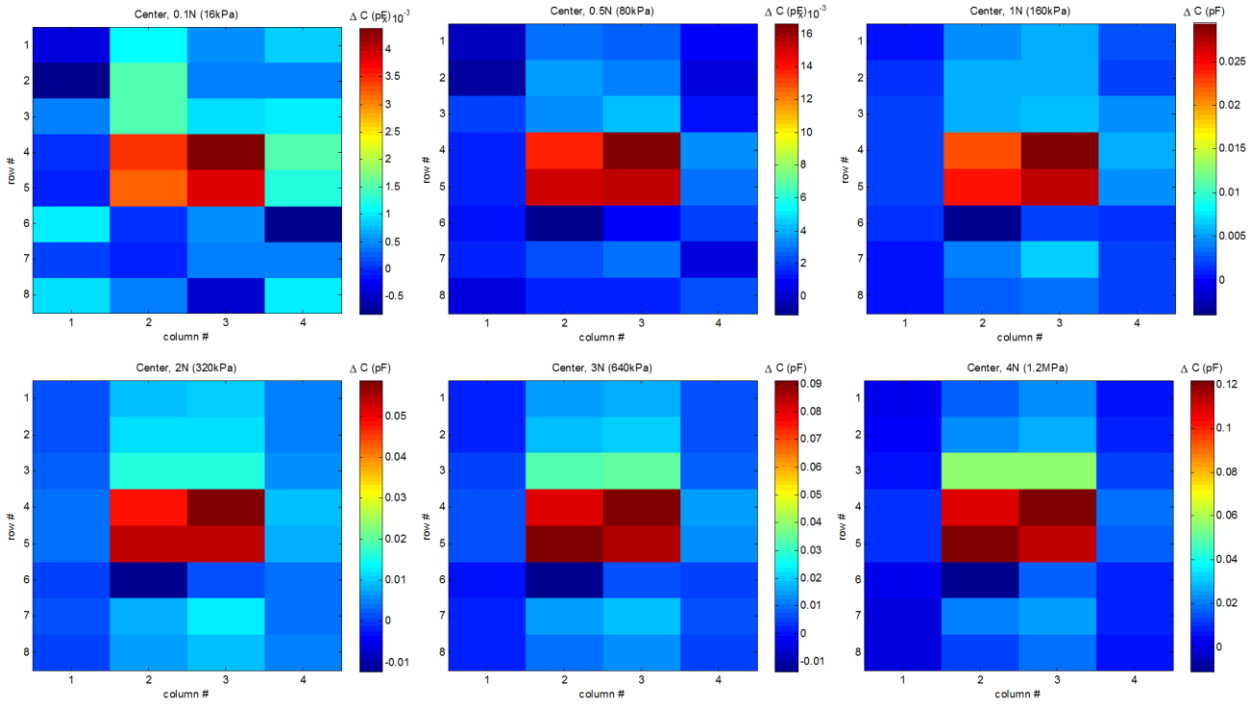

Figure C1. Indenter over sensors *(4,2) ~ (5,3)*

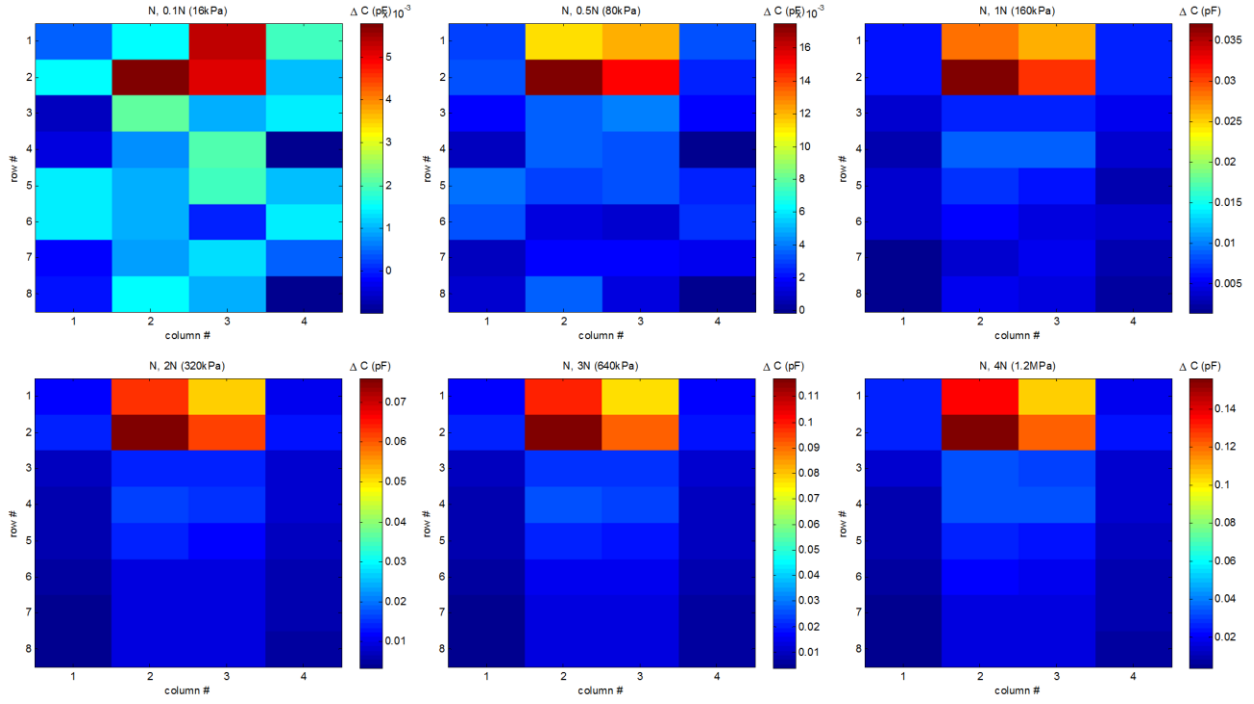

Figure C2. Indenter over sensors *(1,2) ~ (2,3)*

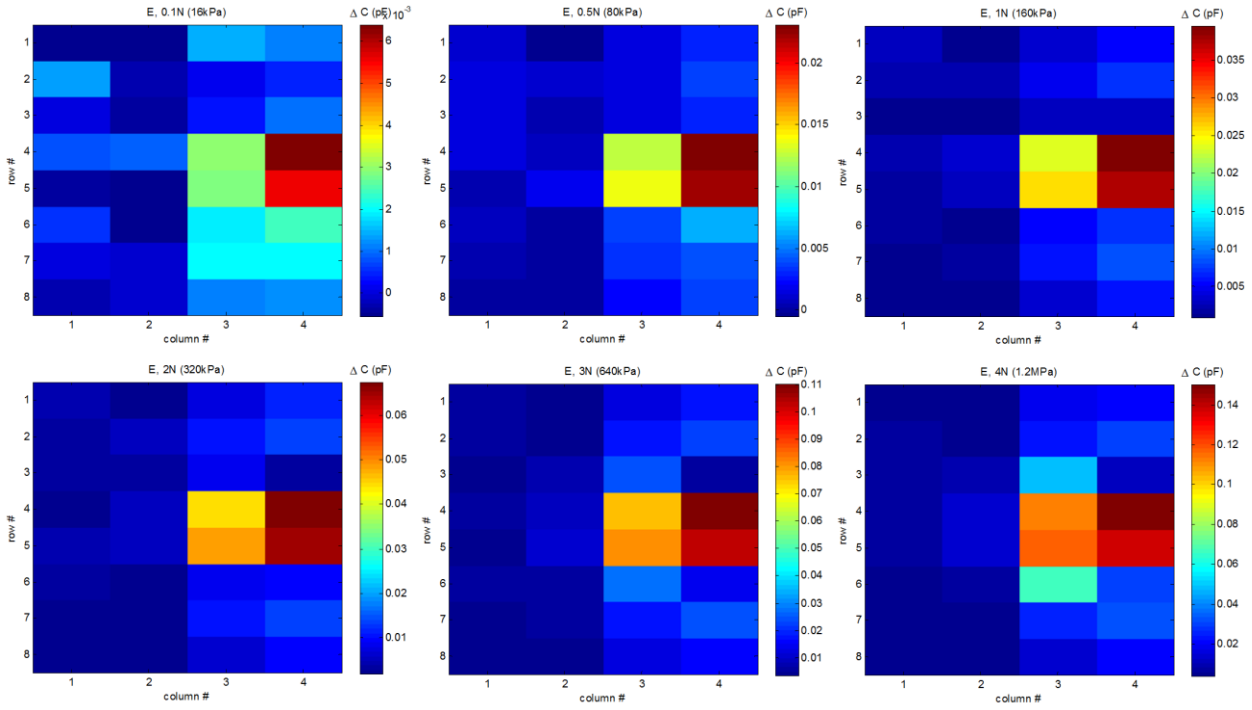

Figure C3. Indenter over sensors *(3,4) ~ (4,5)*

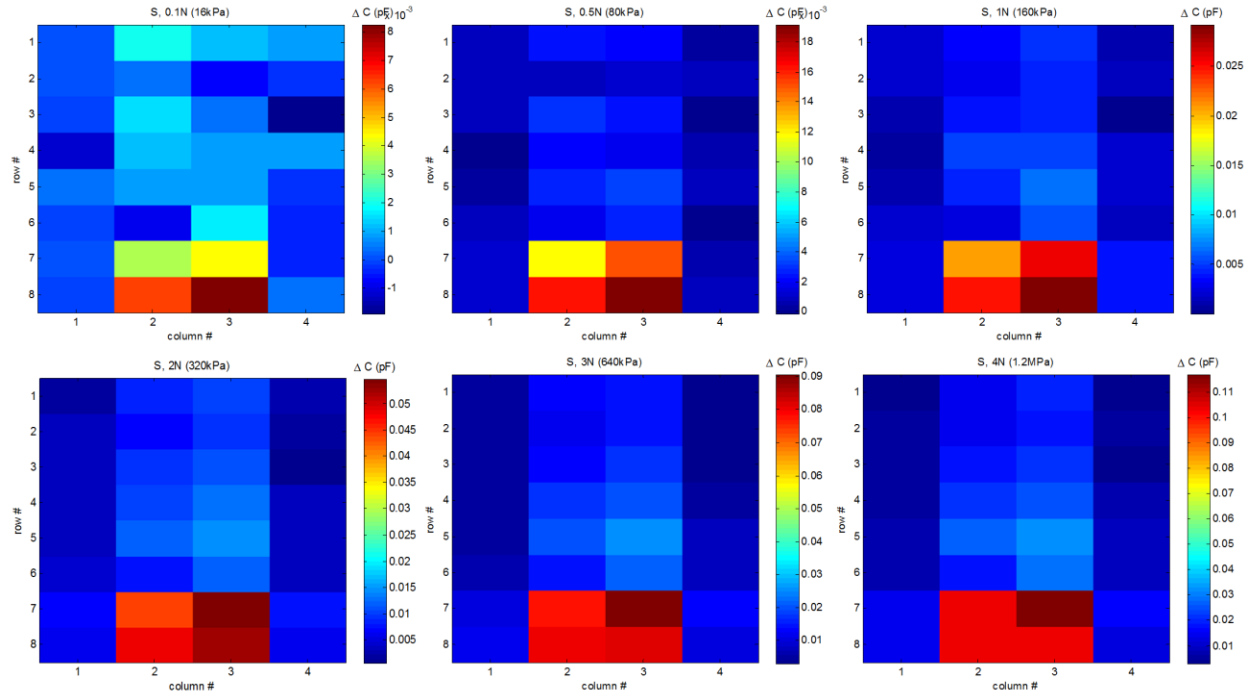

Figure C4. Indenter over sensors *(7,2) ~ (8,3)*

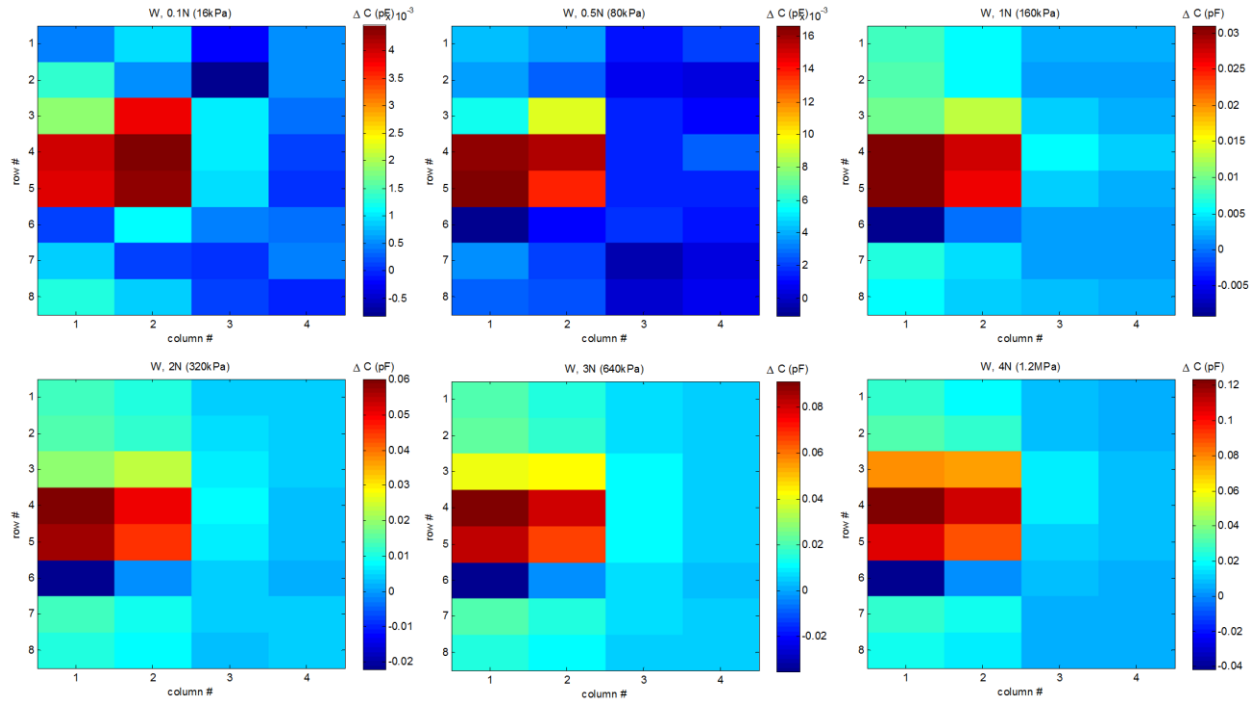

Figure C5. Indenter over sensors *(1,4) ~ (2,5)*

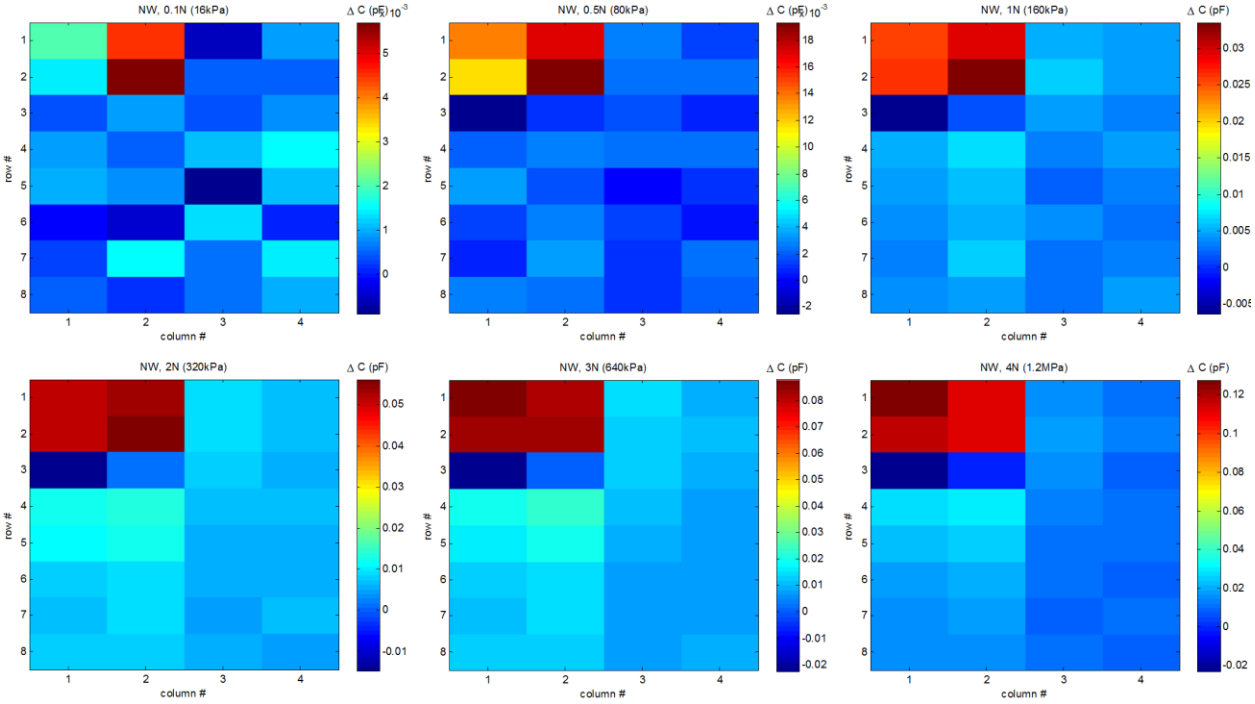

Figure C6. Indenter over sensors *(1,1) ~ (2,2)*

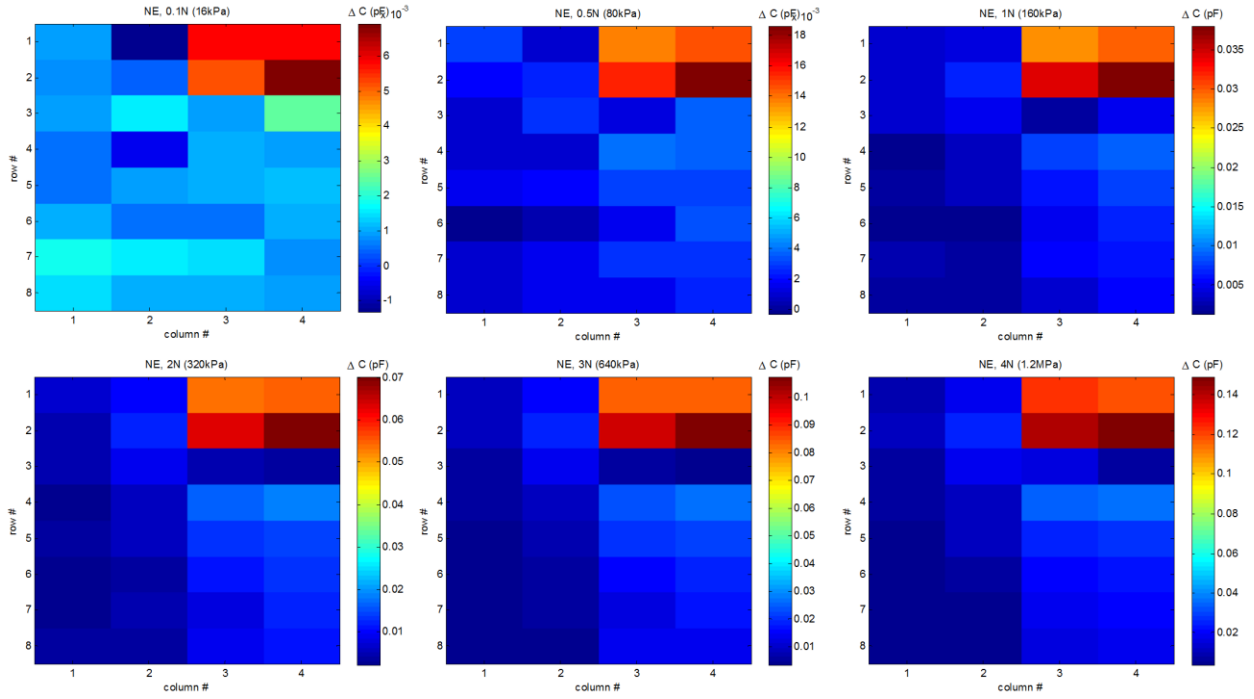

Figure C7. Indenter over sensors *(1,7) ~ (2,8)*

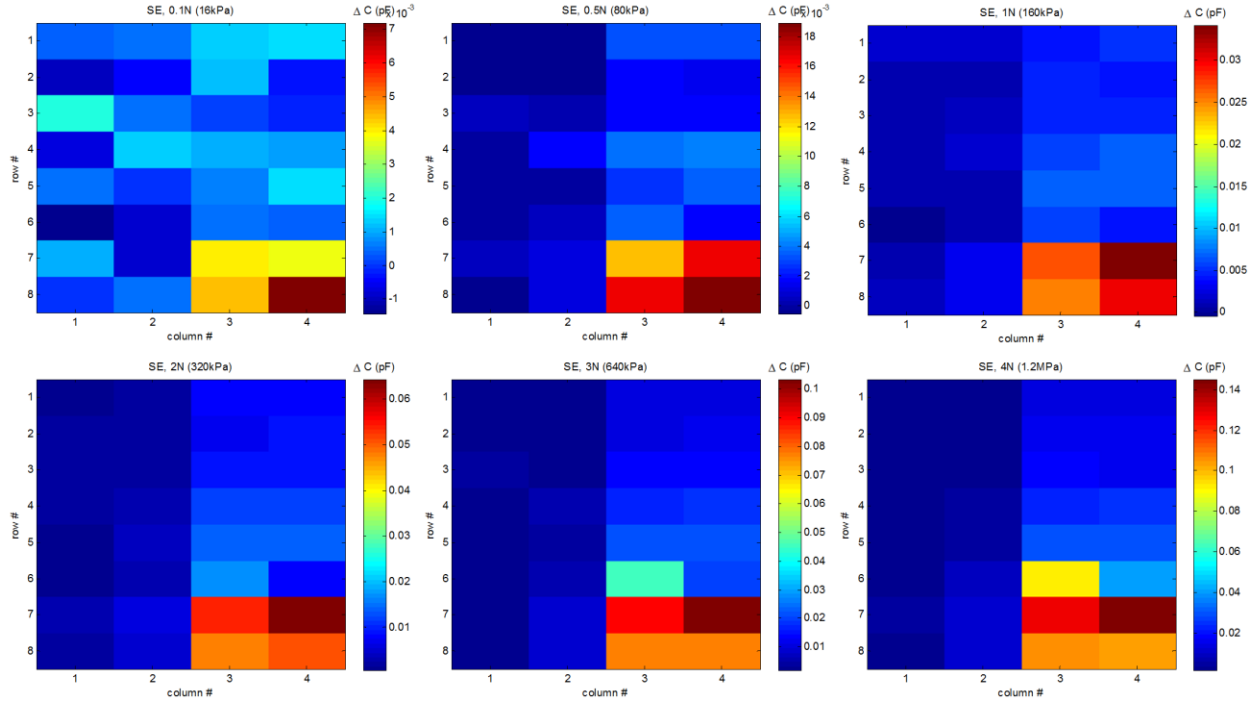

Figure C8. Indenter over sensors *(3,7) ~ (4,8)*

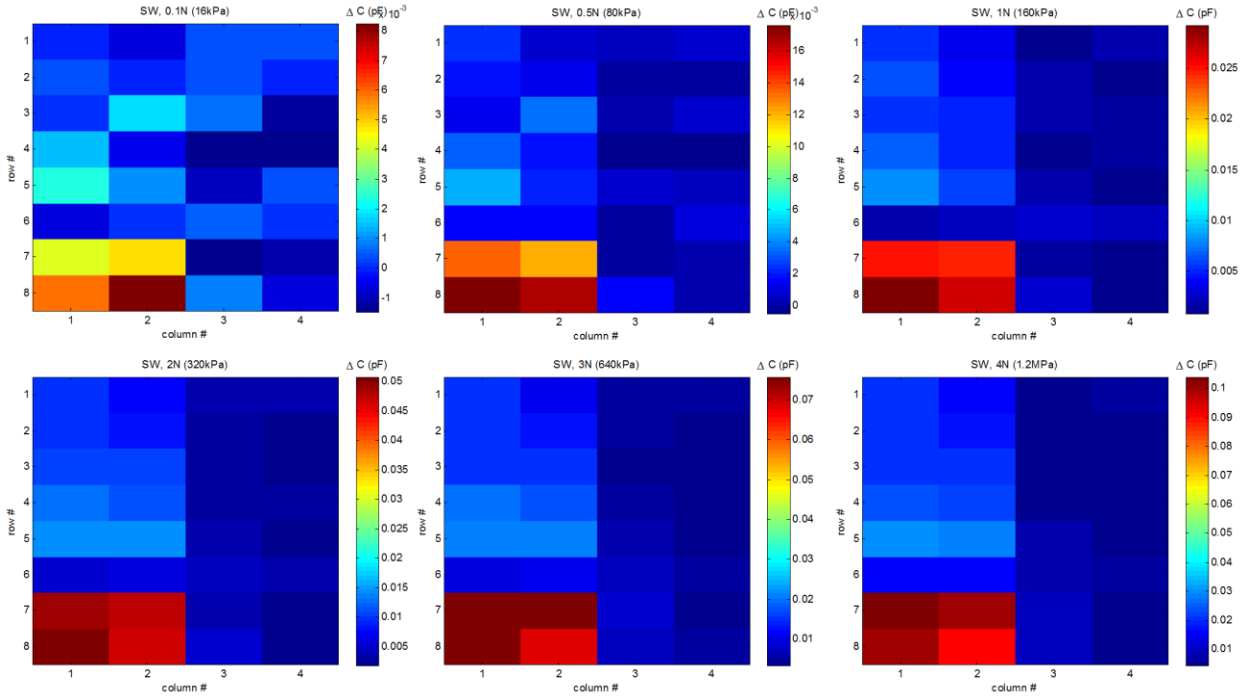

Figure C1. Indenter over sensors *(1,7) ~ (2,8)*

Appendix D: Elastic & viscoelastic model MATLAB script

viscoelastic_dispforce_prony.m

```
%%%%%%%%%%%%%%%%%%%%%%%%%%%%%%%%%%%%%%%%%%%%%%%%%%%%%%%%%%%%%%%%%%%%%%%%%%%%
%Viscoelastic model for DE actuators, Kevin Kadooka 2015
%
%This file requires loaddisplacement.m, which defines the linear elastic
%behavior of the beam and its parameters.
%%%%%%%%%%%%%%%%%%%%%%%%%%%%%%%%%%%%%%%%%%%%%%%%%%%%%%%%%%%%%%%%%%%%%%%%%%%%
clear all
clf

%Can the electrodes be ignored (set to 0) or not (set to 1?)
electrodes = 1;
%TOTAL number of layers (1 passive + n DE layers + n+1 electrodes...)
n = 22;

%Set up sumbolic variables, P is tip load, V is voltage, Y1~3 are stiffness
%of each material
syms P V Y1 Y2 Y3

%Run the loaddisplacementfunc to set up the ELASTIC equations. NOTE!!! You
%have to set the dimensions of the actuator (i.e. length, width,
%thicknesses, dielectric constant, etc). This is kind of inconvenient and
%it is easily changed. May fix this soon.
[delta,alpha,beta] = loaddisplacementfunc(electrodes,n);

%3-parameter prony series - previously used values for reference. 4 is better
%{
%Passive Prony parameters
g0_1 = 1721*10^6;
g1_1 = 154.3*10^6;
g2_1 = -9.39*10^12;
g3_1 = 143*10^6;
tau1_1 = 23.0;
tau2_1 = -1.88*10^7;
tau3_1 = 0.362;
%DE Prony parameters
g0_2 = 291*10^6;
g1_2 = 87.1*10^6;
g2_2 = 36.3*10^6;
g3_2 = 18.7*10^6;
tau1_2 = 63.0;
tau2_2 = 3.22;
tau3_2 = 0.112;
%Electrode Prony params
g0_3 = 3.87*10^6;
g1_3 = 1.66*10^6;
g2_3 = 0.592*10^6;
g3_3 = 0.520*10^6;
tau1_3 = 72.8;
tau2_3 = 16.7;
tau3_3 = 3.2;
%Make vectors with g and tau values;
```

```
g_array = [g0_1 g1_1 g2_1 g3_1 g0_2 g1_2 g2_2 g3_2 g0_3 g1_3 g2_3 g3_3];
tau_array = [tau1_1 tau2_1 tau3_1 tau1_2 tau2_2 tau3_2 tau1_3 tau2_3 tau3_3
];
%}


%4-parameter prony series
%Passive Prony parameters
g0_1 = 1663.2e6;
g1_1 = 350.4e6;
g2_1 = 241.6e6;
g3_1 = 51.26e6;
g4_1 = 153.1e6;
tau1_1 = 1170;
tau2_1 = 0.5503;
tau3_1 = 1.672;
tau4_1 = 25.98;
%DE Prony parameters
g0_2 = 395.6e6;
g1_2 = 36.43e6;
g2_2 = 87.35e6;
g3_2 = 123.02e6;
g4_2 = 0;
tau1_2 = 3.441;
tau2_2 = 53.42;
tau3_2 = 1.5903;
tau4_2 = 1;
%Electrode Prony params
g0_3 = 4.885e6;
g1_3 = 0.6159e6;
g2_3 = 1.746e6;
g3_3 = 0.7235e6;
g4_3 = 0.6757e6;
tau1_3 = 12.55;
tau2_3 = 67.05;
tau3_3 = 0.1245;
tau4_3 = 1.715;
%Make vectors with g and tau values;
g_array = [g0_1 g1_1 g2_1 g3_1 g4_1 g0_2 g1_2 g2_2 g3_2 g4_2 g0_3 g1_3 g2_3
g3_3 g4_3];
tau_array = [tau1_1 tau2_1 tau3_1 tau4_1 tau1_2 tau2_2 tau3_2 tau4_2 tau1_3
tau2_3 tau3_3 tau4_3];
%}

%If we have no electrodes, we're only using two materials. In that case we
%have to calculate two laplace transforms. Otherwise we calculate 3.
if electrodes == 0
    q = 2;
else
    q = 3;
end

%Declare our spatial variables, time and "s" in Laplace domain. We define
%the creep function, D(t), and calculate its Laplace transform, Db(t).
syms t s
```

```
for i = 1:q
    %For 3-parameter Prony Series...
    %G(i) = g_array(4*(i-1)+1) - g_array(4*(i-1)+2)*(1-exp(-t/tau_array(3*(i-
1)+1)))- g_array(4*(i-1)+3)*(1-exp(-t/tau_array(3*(i-1)+2)))- g_array(4*(i-
1)+4)*(1-exp(-t/tau_array(3*(i-1)+3)));
    %For 4-parameter Prony Series...
    G(i) = g_array(5*(i-1)+1) - g_array(5*(i-1)+2)*(1-exp(-t/tau_array(4*(i-
1)+1)))- g_array(5*(i-1)+3)*(1-exp(-t/tau_array(4*(i-1)+2)))- g_array(5*(i-
1)+4)*(1-exp(-t/tau_array(4*(i-1)+3)))- g_array(5*(i-1)+5)*(1-exp(-
t/tau_array(4*(i-1)+4)));
    G(i) = G(i)/(1-0.5^2); %Stiffness increase because of plane strain
    if i == 1
        G(i) = G(i)/(1-0.35^2);
    end
    Gb(i) = laplace(G(i),t,s);

    D(i) = ilaplace(1/((s^2)*Gb(i)),s,t);
    Db(i) = laplace(vpa(D(i)),t,s);
    %Db(i) = laplace(D(i),t,s);
end

%Again, if we have no electrodes we have fewer substitutions to make for
%the correspondence principle. Here we get rid of the "P" term and set
%"V^2" to one. This gives us Sb, the laplace transform of the "response"
%term in the convolution integral.
if electrodes == 0
    Sb = subs(beta,[Y1,Y2],[1/Db(1),1/Db(2)]);
    B = subs(beta,[Y1,Y2],[Gb(1),Gb(2)]);
    A = subs(alpha,[Y1,Y2],[Gb(1),Gb(2)]);
else
    Sb = subs(beta,[Y1,Y2,Y3],[1/Db(1),1/Db(2),1/Db(3)]);
    B = subs(beta,[Y1,Y2 Y3],[Gb(1),Gb(2),Gb(3)]);
    A = subs(alpha,[Y1,Y2 Y3],[Gb(1),Gb(2),Gb(3)]);
end

Sb_char = char(Sb);
Sb_char = strrep(Sb_char,'*i','*0');
Sb = sym(Sb_char);

%Perform the inverse laplace transform on Sb to get plain old S. Use vpa()
%to make things a little bit faster.
tic
disp('Inverting Sb');
Sv = vpa(ilaplace(Sb,s,t));
toc
tic
disp('Inverting Wb');
Wv = vpa(ilaplace(-B/A,s,t));
toc

%Define a time vector for convolution and plotting.
tf = 120;             %usually set to 120
dt = 0.01;           %usually set to 0.1
tvec = 0:dt:tf;

%S is a syms variable, so substitute variable "t" with the actual time
```

```
%vector "tvec" and turn it into a "double" so we can convolve and plot.
S = double(subs(Sv,t,tvec));
W = double(subs(Wv,t,tvec));

%plot(tvec,S)

%Make a voltage vector for plotting.
Vramplength = 0.1;
Vmax = 500;
%Vrampendindex = round(Vramplength/dt)+1;
%V = tvec*Vmax/Vramplength;
%V(Vrampendindex:length(V)) = V(Vrampendindex);
V(1:length(tvec)) = Vmax;
V(1:5) = Vmax*[0 79.2 402.1 457 493.3]/500;
V = double(V);

%Perform the convolution to get the displacement, "disp."
disp = conv(S,diff(V.^2));

syms tau
Wvc = subs(Wv,t,tau);
Vv = Vmax*heaviside(t);
Vvc = subs(Vv,t,t-tau);
result = 2*vpa(int(Wvc*Vvc^2,tau,0,t));
force = subs(result,t,tvec);
%plot(tvec,abs(force))

%Load experimental data
A = csvread('10Lt.csv');
te = A(:,1);
de500 = A(:,2)/1000;
fe500 = A(:,3)/1000;
de400 = A(:,4)/1000;
fe400 = A(:,5)/1000;
de300 = A(:,6)/1000;
fe300 = A(:,7)/1000;
de200 = A(:,8)/1000;
fe200 = A(:,9)/1000;
de100 = A(:,10)/1000;
fe100 = A(:,11)/1000;

%Dotted experimental data
ns = 20; %plot the data every ns data points
iter = 1;
for i = 1:ns:length(te)
    tn(iter) = te(i);
    de500n(iter) = de500(i);
    fe500n(iter) = fe500(i);
    de400n(iter) = de400(i);
    fe400n(iter) = fe400(i);
    de300n(iter) = de300(i);
    fe300n(iter) = fe300(i);
    de200n(iter) = de200(i);
    fe200n(iter) = fe200(i);
    de100n(iter) = de100(i);
    fe100n(iter) = fe100(i);
```

```
    iter = iter+1;
end

%Plot that business.
%{
subplot 211
plot(tvec,abs(disp(1:length(tvec))),te,de500)
xlabel('time(s)')
ylabel('displacement (m)')
subplot 212
plot(tvec,abs(force(1:length(tvec))),te,fe500)
xlabel('time(s)')
ylabel('force (N)')
%}

%Multiple voltage plot

%Plot that business.
plotopts1a.Color = [0 0.5 1];
plotopts1b.Color = [0.5 1 0];
plotopts1c.Color = [1 0.5 0];
plotopts1d.Color = [0.5 0.8 1];
plotopts1e.Color = [1 0.5 0.8];
plotopts2a.LineStyle = 'none';plotopts2a.Color = 'b';plotopts2a.Marker =
's';plotopts2a.MarkerFaceColor = 'b';plotopts2a.MarkerSize = 2;
plotopts2b.LineStyle = 'none';plotopts2b.Color = 'g';plotopts2b.Marker =
's';plotopts2b.MarkerFaceColor = 'g';plotopts2b.MarkerSize = 2;
plotopts2c.LineStyle = 'none';plotopts2c.Color = 'r';plotopts2c.Marker =
's';plotopts2c.MarkerFaceColor = 'r';plotopts2c.MarkerSize = 2;
plotopts2d.LineStyle = 'none';plotopts2d.Color = 'c';plotopts2d.Marker =
's';plotopts2d.MarkerFaceColor = 'c';plotopts2d.MarkerSize = 2;
plotopts2e.LineStyle = 'none';plotopts2e.Color = 'm';plotopts2e.Marker =
's';plotopts2e.MarkerFaceColor = 'm';plotopts2e.MarkerSize = 2;

dp500 = abs(disp(1:length(tvec)));
fp500 = abs(force(1:length(tvec)));

subplot 211
hold on
plot(tvec,abs(disp(1:length(tvec))),plotopts1a)
%{
plot(tvec,abs(disp(1:length(tvec)))*(4/5)^2,plotopts1b)
plot(tvec,abs(disp(1:length(tvec)))*(3/5)^2,plotopts1c)
plot(tvec,abs(disp(1:length(tvec)))*(2/5)^2,plotopts1d)
plot(tvec,abs(disp(1:length(tvec)))*(1/5)^2,plotopts1e)
%}
plot(tn,de500n,plotopts2a)
%{
plot(tn,de400n,plotopts2b)
plot(tn,de300n,plotopts2c)
plot(tn,de200n,plotopts2d)
plot(tn,de100n,plotopts2e)
%}
hold off
xlabel('time(s)')
ylabel('displacement (m)')
```

```
%legend('500V','400V','300V','200V','100V')

subplot 212
hold on
plot(tvec,abs(force(1:length(tvec))),plotopts1a)
%{
plot(tvec,abs(force(1:length(tvec)))*(4/5)^2,plotopts1b)
plot(tvec,abs(force(1:length(tvec)))*(3/5)^2,plotopts1c)
plot(tvec,abs(force(1:length(tvec)))*(2/5)^2,plotopts1d)
plot(tvec,abs(force(1:length(tvec)))*(1/5)^2,plotopts1e)
%}
plot(tn,fe500n,plotopts2a)
%{
plot(tn,fe400n,plotopts2b)
plot(tn,fe300n,plotopts2c)
plot(tn,fe200n,plotopts2d)
plot(tn,fe100n,plotopts2e)
%}
xlabel('time(s)')
ylabel('force (N)')
hold off
%}
```

loaddisplacementfunc.m

```
%%%%%%%%%%%%%%%%%%%%%%%%%%%%%%%%%%%%%%%%%%%%%%%%%%%%%%%%%%%%%%%%%%%%%%%%%%%%%%%
%Elastic model for DE actuators, Kevin Kadooka 2015
%
%This file is a companion to viscoelastic_dispforce_x.m
%It creates an expression for the displacement, and alpha and beta
%parameters, later used in the viscoelastic model.
%Commented out content can be un-commented so it can stand on its own.
%%%%%%%%%%%%%%%%%%%%%%%%%%%%%%%%%%%%%%%%%%%%%%%%%%%%%%%%%%%%%%%%%%%%%%%%%%%%%%%

function [delta,alpha,beta] = loaddisplacementfunc(electrodes,n)

%Set up actuator length and width
L = 0.010;
b = 0.010;

%First we declare symbolic variables for the Young's moduli. Typically
%there are only 3 materials, passive(Y1), DE(Y2), and electrode(Y3)
syms Y1 Y2 Y3

%Thicknesses of the DE and passive layers
h_PS = 50*10^-6;
h_DE = 12*10^-6;
h_EL = 17*10^-6;

%Vacuum permittivity and relative dielectric constant
ep0 = 8.85*10^-12;
epr = 50;

%Assume that the materials are sufficiently soft to be incompressible
```

```
v(1:n) = 0.5/(1-0.5);%Increased for plane strain???

%If we aren't including electrodes, the first layer is a passive and the
%rest is DE.
if electrodes == 0
    Y{1} = Y1;
    for i = 2:n
        Y{i} = Y2;
    end

    z(1) = 0;
    z(2) = h_PS;
    for i = 3:n+1
        z(i) = z(i-1)+h_DE;
    end

    ep(1) = 0;
    ep(2:n) = epr;
%Otherwise, we will include electrodes. The first layer is a passive, and
%subsequent even layers are electrodes, odd are DE.
else
    Y{1} = Y1;
    for i = 2:n
        if mod(i,2) == 0
            Y{i} = Y3;
        else
            Y{i} = Y2;
        end
    end

    z(1) = 0;
    z(2) = h_PS;
    for i = 3:n+1
        if mod(i,2) == 0
            z(i) = z(i-1) + h_DE;
        else
            z(i) = z(i-1) + h_EL;
        end
    end

    ep(1) = 0;
    for i = 2:n
        if mod(i,2) == 0
            ep(i) = 0;
        else
            ep(i) = epr;
        end
    end
end


%Next we construct the linear elastic solution using our known equation.
%Each term requires several summations, so we use for loops.

%%%%%%%%%%%%%%%%%%%%%%%%%%%%%% Set up K %%%%%%%%%%%%%%%%%%%%%%%%%%%%%%%%%%%%
```

```
K1 = 0;
K2 = 0;
K3 = 0;
for i = 1:n
    K1 = K1 + (1/2)*Y{i}*z(i+1)^2 - (1/2)*Y{i}*z(i)^2;
    K2 = K2 + Y{i}*(z(i+1)-z(i));
    K3 = K3 + (1/3)*Y{i}*z(i+1)^3 - (1/3)*Y{i}*(z(i)^3);
end
K = K1^2 - K2*K3;

%%%%%%%%%%%%%%%%%%%%%%%%%%%%%% Set up beta %%%%%%%%%%%%%%%%%%%%%%%%%%%%%%

B1 = 0;
B2 = 0;
B3 = 0;
B4 = 0;
for i = 1:n
    B1 = B1 + Y{i}*(z(i+1)-z(i));
    B2 = B2 + v(i)*ep(i)*ep0*(z(i)+z(i+1))/(2*(z(i+1)-z(i)));
    B3 = B3 + (1/2)*Y{i}*(z(i+1)^2 - z(i)^2);
    B4 = B4 + v(i)*ep(i)*ep0/(z(i+1)-z(i));
end
beta = 1/(2*K)*(B1*B2 - B3*B4)*L^2;

%%%%%%%%%%%%%%%%%%%%%%%%%%%%%% Set up alpha %%%%%%%%%%%%%%%%%%%%%%%%%%%%%%

A1 = 0;
for i = 1:n
    A1 = A1 + Y{i}*(z(i+1)-z(i));
end
alpha = -A1*L^3/(3*b*K);

%%%%%%%%%%%%%%%%%%%%%%%%%% Finish up and get delta %%%%%%%%%%%%%%%%%%%%%%%%%%

%Declare our "input" variables, P (force) and V (voltage).
syms P V
delta = alpha*P + beta*V^2;

end
```

Appendix E: Artery mapper serial data MATLAB script

SensorReadContinuous.m

```
%Artery mapper serial communication program
%Kevin Kadooka, Feb 2017

clf
clear all

%Delete all instances of serial objects
delete(instrfind)

%3-second pause, just so you can get things settled
pause(3)

%Make and open a new serial object to read serial data
arduino = serial('COM4','BaudRate',115200,'InputBufferSize',4096)
fopen(arduino);

%Init some variables
samples = 32;               %32 data sets will be collected, for 4 rows x 8
cols
S = zeros(samples,1);       %"S" will be used to store the signal "power"
Fs = 85;                    %Sampling frequency for making time vector

figure(1)
for i = 1:samples
    b = fscanf(arduino,'%s');
%Scan the serial port for new data
    b = str2double(strsplit(b,','));
%Convert "string" to "double"
    t_vec = linspace(0,length(b)/Fs,length(b));
%Construct a time vector based on Fs

    C(i,:) = b;
%Cap-time data gets saved in array C. Smoothing by moving average can be done
here or elsewhere
    %C(i,:) = smooth(b,9);

    subplot(311)
    plot(t_vec,smooth(b,9))
    title(i)

    M = smooth(b,10);
%Smooth data, remove linear trend, and window for FFT
    R = detrend(M);
    R = R.*hann(256);

    Y = fft(R);
%Perform the FFT & plot it
    L = length(R);
```

```
    P2 = abs(Y/L);
    P1 = P2(1:L/2+1);
    P1(2:end-1) = 2*P1(2:end-1);
    f = Fs*(0:(L/2))/L;
    subplot(312)
    plot(f,P1)

    %"S" is used to hold the "signal strength," which is calculated through
    %a variety of methods. So far I have found that the last one (summing
    %FFT bins at fundamental & harmonics works reliably

    %S(i) = max(detrend(b)) - min(detrend(b));
    %S(i) = sum(sqrt((detrend(b)).^2))/length(detrend(b));
    %S(i) = sum(P1(4:6));
    %S(i) = P1(5);
    S(i) = P1(5) + P1(9) + P1(13) + P1(17);

    %Plot "S"
    subplot(313)
    imagesc(transpose(reshape(S,8,4)))
    colorbar
    drawnow
end

fclose(arduino);

%Signal strength varies a lot between each row! So redraw the "S" plot,
%using a different color bar for each row.
figure(2)
S4 = transpose(reshape(S,8,4));
subplot(411)
imagesc(S4(1,:))
subplot(412)
imagesc(S4(2,:))
subplot(413)
imagesc(S4(3,:))
subplot(414)
imagesc(S4(4,:))
colormap winter
```

Appendix F: Artery mapper firmware (Arduino IDE)

```
//Artery mapper firmware
//February 2017
//Kevin Kadooka

//Include I2C library
#include <Wire.h>

//Define the control pins for the column MUX
#define R8 5
#define R7 13
#define R6 A0
#define R5 A1
#define R4 A2
#define R3 A3
#define R2 A4
#define R1 A5

//Init FDC1004 I2C address
const uint8_t reg = 80;

//Init variables to store capacitance, time
float C[256];
uint32_t t_init;

//Init variables to store MSB,LSB cap data from FDC1004
int lb1, lb2, lb3;
unsigned int lbb1, lbb2, lbb3;

void setup()
{
  //Begin the serial connection and wait for handshake
  Serial.begin(115200);
  while(!Serial)
  {;}

  //Pin 7 can be used for coordinating tasks w/ other devices
  pinMode(7,OUTPUT);

  //Init control pins as outputs
  pinMode(R1,OUTPUT);
  pinMode(R2,OUTPUT);
  pinMode(R3,OUTPUT);
  pinMode(R4,OUTPUT);
  pinMode(R5,OUTPUT);
  pinMode(R6,OUTPUT);
  pinMode(R7,OUTPUT);
  pinMode(R8,OUTPUT);

  //Control pins should NOT be left floating, so set them low for now
  digitalWrite(R1,LOW);
  digitalWrite(R2,LOW);
  digitalWrite(R3,LOW);
```

```
  digitalWrite(R4,LOW);
  digitalWrite(R5,LOW);
  digitalWrite(R6,LOW);
  digitalWrite(R7,LOW);
  digitalWrite(R8,LOW);

  Wire.begin();
  //Set up Meas 1, CH 1
  Wire.beginTransmission(reg);
  Wire.write(0x08);
  Wire.write(B00010000);
  Wire.write(B00000000);
  Wire.endTransmission();
  //Set up Meas 2, CH 2
  Wire.beginTransmission(reg);
  Wire.write(0x09);
  Wire.write(B00110000);
  Wire.write(B00000000);
  Wire.endTransmission();
  //Set up Meas 3, CH 3
  Wire.beginTransmission(reg);
  Wire.write(0x0A);
  Wire.write(B01010000);
  Wire.write(B00000000);
  Wire.endTransmission();
  //Set up Meas 4, CH 4
  Wire.beginTransmission(reg);
  Wire.write(0x0B);
  Wire.write(B01110000);
  Wire.write(B00000000);
  Wire.endTransmission();
}

void loop()
{
  //For synchronizing with other devices
  digitalWrite(7,HIGH);

  //This is just a big dumb loop to cycle through all 32 sensors, by columns
then rows.
  for(uint8_t j=1; j<5; j++)
  {
    for(int i=0; i<8; i++)
    {
      if(i == 0)
        {digitalWrite(R1,HIGH);
        digitalWrite(R2,LOW);
        digitalWrite(R3,LOW);
        digitalWrite(R4,LOW);
        digitalWrite(R5,LOW);
        digitalWrite(R6,LOW);
        digitalWrite(R7,LOW);
        digitalWrite(R8,LOW);}
      else if(i == 1)
        {digitalWrite(R1,LOW);
        digitalWrite(R2,HIGH);
        digitalWrite(R3,LOW);
```

```
  digitalWrite(R4,LOW);
  digitalWrite(R5,LOW);
  digitalWrite(R6,LOW);
  digitalWrite(R7,LOW);
  digitalWrite(R8,LOW);}
else if(i == 2)
  {digitalWrite(R1,LOW);
  digitalWrite(R2,LOW);
  digitalWrite(R3,HIGH);
  digitalWrite(R4,LOW);
  digitalWrite(R5,LOW);
  digitalWrite(R6,LOW);
  digitalWrite(R7,LOW);
  digitalWrite(R8,LOW);}
else if(i == 3)
  {digitalWrite(R1,LOW);
  digitalWrite(R2,LOW);
  digitalWrite(R3,LOW);
  digitalWrite(R4,HIGH);
  digitalWrite(R5,LOW);
  digitalWrite(R6,LOW);
  digitalWrite(R7,LOW);
  digitalWrite(R8,LOW);}
else if(i == 4)
  {digitalWrite(R1,LOW);
  digitalWrite(R2,LOW);
  digitalWrite(R3,LOW);
  digitalWrite(R4,LOW);
  digitalWrite(R5,HIGH);
  digitalWrite(R6,LOW);
  digitalWrite(R7,LOW);
  digitalWrite(R8,LOW);}
else if(i == 5)
  {digitalWrite(R1,LOW);
  digitalWrite(R2,LOW);
  digitalWrite(R3,LOW);
  digitalWrite(R4,LOW);
  digitalWrite(R5,LOW);
  digitalWrite(R6,HIGH);
  digitalWrite(R7,LOW);
  digitalWrite(R8,LOW);}
else if(i == 6)
  {digitalWrite(R1,LOW);
  digitalWrite(R2,LOW);
  digitalWrite(R3,LOW);
  digitalWrite(R4,LOW);
  digitalWrite(R5,LOW);
  digitalWrite(R6,LOW);
  digitalWrite(R7,HIGH);
  digitalWrite(R8,LOW);}
else if(i == 7)
  {digitalWrite(R1,LOW);
  digitalWrite(R2,LOW);
  digitalWrite(R3,LOW);
  digitalWrite(R4,LOW);
  digitalWrite(R5,LOW);
  digitalWrite(R6,LOW);
```

```
        digitalWrite(R7,LOW);
        digitalWrite(R8,HIGH);}
      delay(50);
      //The first 10 readings are sometimes spurious, so read and discard
      for(int k=0; k<10; k++)
      {capRead(j);}
      //Read 256 samples and then print to serial.
      for(int k=0; k<256; k++)
      {
        C[k] = capRead(j);
      }
      for(int i=0; i<256; i++)
      {
        if(i == 255)
        {
          Serial.println(C[i],5);
        }
        else
        {
          Serial.print(C[i],5);
          Serial.print(",");
        }
      }
    }
  }

  //End of synchronization (optional).
  digitalWrite(7,LOW);
}

//A function to read capacitance measurements from the FDC
float capRead(uint8_t channel)
{
  Wire.beginTransmission(reg);
  Wire.write(12);
  Wire.write(B00000100);
  if(channel == 1)
  {Wire.write(B10000000);}
  else if(channel == 2)
  {Wire.write(B01000000);}
  else if(channel == 3)
  {Wire.write(B00100000);}
  else
  {Wire.write(B00010000);}

  Wire.endTransmission();

  delay(10);

  Wire.beginTransmission(reg);            //Read data from 0x00 and 0x01
  if(channel == 1)
  {Wire.write(0);}
  else if(channel == 2)
  {Wire.write(2);}
  else if(channel == 3)
  {Wire.write(4);}
  else
```

```
  {Wire.write(6);}
  Wire.endTransmission();
  Wire.requestFrom(reg, 2);
  while (Wire.available())
  {
    lb1 = Wire.read();
    lb2 = Wire.read();
  }
  Wire.beginTransmission(reg);
  if(channel == 1)
  {Wire.write(1);}
  else if(channel == 2)
  {Wire.write(3);}
  else if(channel == 3)
  {Wire.write(5);}
  else
  {Wire.write(7);}
  Wire.endTransmission();
  Wire.requestFrom(reg, 1);
  while (Wire.available())
  {
    lb3 = Wire.read();
  }

  lbb1 = lb1 * 256 + lb2;
  lbb2 = lbb1 >> 11;
  lbb3 = 0b0000011111111111 & lbb1;
  float result = lbb2 + (float)lbb3 / 2048 + (float)lb3 / 1048576;
  return result;
}
```

Vita

Education

Doctor of Philosophy, Mechanical Engineering (June 2017)
University of Washington
Seattle, Washington

M.S. Mechanical Engineering (March 2016)
University of Washington
Seattle, Washington

B.S. Mechanical Engineering (May 2013)
University of Portland Shiley School of Engineering
Portland, Oregon

Publications

Kadooka, K., Imamura, H., Taya, M. "Experimentally verified model of viscoelastic behavior of multilayer unimorph dielectric elastomer actuators", *Smart Material and Structures* 25 105028, 2016.

Imamura, H., Kadooka, K., Taya, M. "Variable stiffness dielectric elastomer actuator based on electrostatic chucking", accepted by *Soft Matter* April 7 2017.

Presentations & proceedings papers

Kadooka, K., Taya, M., Naito, K., Saito, M. "Modeling of a corrugated dielectric elastomer actuator for artificial muscle applications", *Proc. SPIE* 9530 943020, 2015.

Kadooka, K., Taya, M., Adcock, J. "Bioinspired dielectric elastomer sensor for measurement of 3D tactile forces", *8th World Congress on Biomimetics, Artificial Muscles, and Nano-Bio,* 24 August 2016, University of British Columbia, Vancouver, Canada. Invited speaker.

Kadooka, K., Imamura, H., Taya, M. "Tactile sensor integrated dielectric elastomer actuator for simultaneous actuation and sensing", *Proc. SPIE* 9798 97982H, 2016.

Imamura, H., Kadooka, K., Taya, M., Kimura, M. "Processing of dielectric laminate actuator based on high precision dispenser and ink jet", *Proc. SPIE* 9798, 97981B, 2016.

Imamura, H., Kadooka, K., Taya, M. "Dielectric elastomer actuator with variable bending stiffness property based on interlaminar electrostatic chucking", to be presented March 2017 at *SPIE Smart Structures/NDE 2017*, Portland, Oregon.